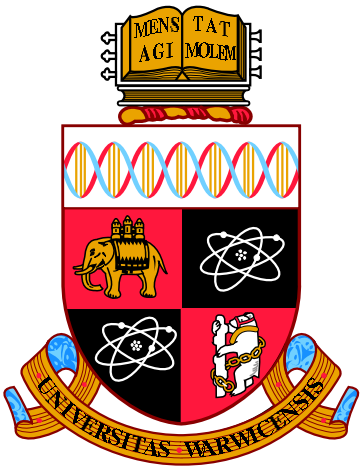

Development of two *in vitro* methodologies for the study of brain network dynamics and an application to the study of seizure-evoked adenosine release

by

Matthew George Thomas

Thesis

Submitted to the University of Warwick

for the degree of

Doctor of Philosophy

MOAC Doctoral Training Centre

July 2015

THE UNIVERSITY OF WARWICK

Contents

List of Figures

Acknowledgments

Firstly, I thank my supervisors, Prof. Matthew Turner, Dr Mark Wall, Dr Magnus Richardson and Dr James Covington; my advisory committee, Dr Joanna Collingwood, Dr Dawn Collins and Dr Steven Maggs as well as the neuroscience group at the University of Warwick and Dr Ramesh Arasaradnam for their advice and support over the time I have spent at Warwick. I also thank the MOAC DTC and the EPSRC for support and funding. Finally, I thank my friends and family for their support.

Declarations

The work presented in this thesis is entirely original and my own work, except where acknowledged in the text or figure legends. I confirm that this thesis has not been submitted for a degree at any other University.

Chapter 2 was published as:
Thomas, M.G.; Covington, J.A.; Wall, M.J.
A chamber for the perfusion of *in vitro* tissue with multiple solutions.
Journal of Neurophysiology 110:269-277, 2013

Chapter 3 is in review for:
Thomas, M.G.; Covington, J.A.; Richardson, M.J.E.; Turner, M.S.; Wall, M.J.
High-resolution recording of neural activity by transforming intrinsic optical signals.

Chapter 4 is in preparation for:
Thomas, M.G.; Richardson, M.J.E.; Wall, M.J.
Characterisation of the spatio-temporal dynamics of the extracellular concentration of adenosine in the neocortex in response to electrographic seizure activity.

Appendix B was published as:
Arasaradnam, R.P.; Ouaret, N.; **Thomas, M.G.**; Gold, P.; Quraishi, M.N.; Nwokolo, C.U.; Bardhan, K.D.; Covington, J.A.
Evaluation of gut bacterial populations using an electronic e-nose and field asymmetric ion mobility spectrometry: further insights into 'fermentonomics'.
Journal of Medical Engineering & Technology 36:333-337, 2012

Appendix C was published as:

A novel tool for noninvasive diagnosis and tracking of patients with inflammatory bowel disease.

Arasaradnam, R.P.; Ouaret, N.; **Thomas, M.G.**; Quraishi, M.N.; Heatherington, E.; Nwokolo, C.U.; Bardhan, K.D.; Covington, J.A.

Inflammatory Bowel Diseases 19:999-1003, 2013

Appendix D was published as:

The detection of patients at risk of gastrointestinal toxicity during pelvic radiotherapy by electronic nose and FAIMS: A pilot study.

Covington, J.A.; Wedlake, L.; Andreyev, J.; Ouaret, N.; **Thomas, M.G.**; Nwokolo, C.U.; Bardhan, K.D.; Arasaradnam, R.P.

Sensors 12:13002-13018, 2012

Appendix E was published as:

Detection of colorectal cancer (CRC) by urinary volatile organic compound analysis.

Arasaradnam, R.P.; McFarlane, M.J.; Ryan-Fisher, C.; Westenbrink, E.; Hodges, P.; **Thomas, M.G.**; Chambers, S.; O'Connel, N.; Bailey, C.; Harmston, C.; Nwokolo, C.U.; Bardhan, K.D.; Covington, J.A.

PLOS One 9:e108750

Abstract

Understanding the brain in both health and disease is of critical practical importance as well as fundamental scientific interest. The acute neural tissue slice is a widely used experimental preparation, it facilitates treatments and measurements not practical *in vivo* while preserving a largely connected network representative of the true *in vivo* structure. This thesis presents the development of two techniques for the study of the acute neural tissue slice, both particularly well suited to the study of epilepsy, followed by an application of one of these techniques. A slice chamber is presented that allows extended regions of a tissue slice to be exposed, in isolation, to changes in ionic environment or pharmacological manipulation, readily providing an entirely *in vitro* model of focal epilepsy. Secondly, a transformation is derived that converts the slow dynamics of the intrinsic optical signal (IOS) associated with neuronal activity both *in vivo* and *in vitro* to the form of the associated local field potential, allowing the advantages of the IOS to be exploited while mitigating the primary disadvantage - the lack of direct correspondence between the IOS and the associated network dynamics. Finally a study is presented that employs the transformation of the IOS to facilitate a quantitative characterisation of the spatio-temporal dynamics of adenosine release in response to electrographic seizure activity.

Abbreviations

5-HT 5-Hydroxytryptamine

8-CPT 8-Cyclopentyl-1,3-dimethylxanthine

aCSF artificial Cerebrospinal Fluid

ADA Adenosine Deaminase

ADK Adenosine Kinase

ADP Adenosine Diphosphate

AMP Adenosine Monophosphate

ATP Adenosine Triphosphate

BBSRC Biotechnology and Biological Sciences Research Council

BOLD Blood Oxygen Level Dependent

CA Cornu Ammonis

cAMP cyclic Adenosine Monophosphate

CAD Computer Aided Design

CC Corticocortical Cell

CED Cambridge Electronic Design

CFME Carbon Fibre Micro Electrode

CT Corticothalamic Cell

DC Direct Current

DG Dentate Gyrus

ECoG Electrocorticogram

EEG Electroencephalogram

EHNA Erythro-9-(2-hydroxy-3-nonyl)adenine

EGTA Ethylene Glycol Tetraacetic Acid

ENT Equilibritive Nucleoside Transporter

EPSP Excitatory Post Synaptic Potential

EPSRC Engineering and Physical Sciences Research Council

FAIMS Field Asymmetric Ion Mobility Spectrometry

fEPSP field Excitatory Post Synaptic Potential

fMRI functional Magnetic Resonance Imaging

FPA Fixed Potential Amperometry

FPS Frames Per Second

FSCV Fast Scan Cyclic Voltammetry

FWHM Full Width at Half Maximum

GABA Gamma Aminobutyric Acid

GPCR G-Protein Coupled Receptor

GCMS Gas Chromatography Mass Spectrometry

HEPES 4-(2-hydroxyethyl)-1-piperazineethanesulfonic Acid

IOS Intrinsic Optical Signal

ITN Intratelencephalic Neuron

LED Light Emitting Diode

LFP Local Field Potential

L Layer

MOAC Molecular Organisation and Assembly in Cells

MRI Magnetic Resonance Imaging

MSL Microstereolithography

NBMPR 6-S-(4-Nitrobenzyl)-6-thioinosine

NMDA N-methyl-D-aspartate

PC Pyramidal Cell

RMSD Root Mean Square Deviation

RC Recurrent Collateral

ROI Region of Interest

SPME Solid Phase Micro Extraction

SPN Subcerebral Projection Neurons

tIOS transformed Intrinsic Optical Signal

TTL Transistor Transistor Logic

TTX Tetrodotoxin

Chapter 1

Introduction

Epilepsy is a disorder of the nervous system that is characterised by paroxysmal episodes of abnormal brain activity. In this thesis two techniques for the study of brain function in health and disease, both particularly suited to the study of epilepsy, will be presented. The first is a fluidic device that allows an extended region of a tissue slice to be exposed, in isolation, to changes in environment while preserving the ability to record from the slice. This readily provides a model of focal epilepsy - by exposing a region of tissue to a pro-convulsant while maintaining the remainder of the slice in a physiological medium. The second method transforms the slow temporal dynamics of the intrinsic optical signal (IOS) associated with neuronal activity *in vitro* to a form that accurately mimics the more fundamental dynamics of the local field potential (LFP). This transformation overcomes the primary disadvantage of the use of the IOS as a proxy for recording neuronal activity, allowing the many advantages to be fully exploited. The result is a technique for recording the spatio-temporal dynamics of neuronal activity particularly well suited to the study of the propagation of focal seizure activity. Finally, the transformation of the IOS is applied to the study of the spatiotemporal dynamics of adenosine, a potent neuromodulator implicated in a number of physiological and pathophysiological processes, and that plays a particularly important role in epilepsy.

In this chapter aspects of neurophysiology and neuropharmacology relevant to the studies presented in later chapters will be briefly summarised, a number of techniques for the study of the nervous system will be reviewed and the relevant

Figure 1.1: The structure of a typical neuron showing branching processes. From Briar et al. (2003). The figure has been redacted from this version to avoid copyright infringement.

disease processes will be discussed.

1.1 Brain anatomy and physiology

The brain processes sensory input, stores information and coordinates responses. The current understanding of the cellular basis of these processes will be briefly summarised here, however, for a more thorough review see Kandel et al. (2013).

Cellular composition

The three main components of brain tissue that are thought to be involved in information processing and storage are neurons, astrocytes and oligodendrocytes. Neurons consist of a cell body (soma) that gives rise to a number of processes that connect to other neurons, receive sensory input or transmit output to other parts of the body. Fig 1.1 shows the branching structure of a typical neuron. Input to the neuron is received by the processes termed dendrites and output is conveyed to other neurons along the axon. Neurons are electrically excitable cells, at rest active transport of ions leads to a potential across the membrane $\sim$ -65 mV. However, if a combination of depolarising inputs causes the membrane potential to cross

Figure 1.2: The membrane potential of a typical neuron during an action potential. From Bean (2007). The figure has been redacted from this version to avoid copyright infringement.

a threshold potential (typically $\sim$ -55 mV), the membrane potential undergoes a large transient depolarisation, followed by repolarisation. Such an event is termed an action potential (Fig. 1.2). At their simplest, action potentials are caused by the opening of a large number of voltage gated Na^+ channels in response to initial depolarisation. The resulting influx of Na^+ ions leads to further depolarisation, before the channels inactivate. Voltage gated K^+ channels then open, K^+ ions enter the cell, causing it to repolarise (for a more thorough summary see Bean (2007)). Action potentials are binary events that propagate along the processes of neurons. It is the rate and relative timing of action potentials, in addition to the connectivity of the network that is thought to encode information in the brain. The speed of propagation of action potentials strongly affects brain function. Lower membrane conductance and capacitance both lead to increased propagation speed. To reduce membrane conductance and capacitance other cells, oligodendrocytes in the central nervous system and Schwann cells in the peripheral nervous system, can form an insulating layer, known as myelin, around the axons of neurons. This insulation results in much faster signal propagation. Some diseases, such as Guillain-Barré syndrome and multiple schlerosis, are associated with loss of myelin and cause significant neurological problems.

Figure 1.3: The structure of a typical chemical synapse showing both presynaptic and postsynaptic neurons and an astrocyte. From Briar et al. (2003). The figure has been redacted from this version to avoid copyright infringement.

There are three known forms of coupling between neurons, chemical synapses, gap junctions and ephaptic coupling. Chemical synapses are junctions between the terminal boutons of neurons and their target cells. When an action potential reaches the terminal the depolarisation causes the opening of voltage gated Ca^{2+} channels. As a result, Ca^{2+} ions enter the terminal and cause vesicles of neurotransmitter to stochastically (Ribrault et al., 2011) fuse with the membrane and release their contents in to the synaptic cleft (Fig. 1.3). The neurotransmitter then diffuses across the cleft and binds to receptors on the post-synaptic cell and, potentially, on the pre-synaptic cell and adjacent astrocytes, effecting some change, for a review see Lisman et al. (2007). Most simply, the binding of neurotransmitter to ligand gated ion channels causes them to open channels, ions then move across the membrane of the post-synaptic cell, causing a change in membrane potential. If the combination of synaptic inputs to the post-synaptic neuron causes its membrane to depolarise above its threshold, an action potential will occur. The released transmitter is then removed by astrocytes, cells that surround synapses (for reviews of astrocytic functions see Haydon (2001); Volterra and Meldolesi (2005); Clarke and Barres (2013)). Modulation of synaptic strength is implicated in learning and memory, for reviews see Lamprecht and LeDoux (2004) and Sohl et al. (2005).

In addition to chemical synapses, neurons can be coupled by gap junctions.

Figure 1.4: Golgi stained cortex of a human infant, showing the typical layered structure. From Cajal (1899). The figure has been redacted from this version to avoid copyright infringement.

These are groups of channels that directly connect the cytoplasm of two neurons. Ions can move through the channels and so when the potentials of the connected regions of the two cells are unequal, ions move so as reduce the difference in potential. If, for example, an action potential occurs in one cell, a transient depolarisation occurs in cells to which it is gap junction coupled. For a review see Pereda (2014).

The final way in which neurons are known to couple is by direct field effects, known as ephaptic coupling (Anastassiou et al., 2011). Neurons are electrochemical systems, their dynamics give rise to time varying electric fields, these fields then affect other cells. These effects, although relatively small, are sufficient to entrain the firing of action potentials in adjacent cells (Anastassiou et al., 2011).

Tissue structure

The brain is formed of a number of functionally and structurally distinct regions. The structure of the regions discussed in this thesis will be briefly summarised here, for a more complete discussion see Kandel et al. (2013).

The majority of the results presented in this thesis relate to the neocortex. The neocortex is the outer-most region of the cerebrum, it is responsible for many higher cognitive processes such as perception and the generation of motor commands. The neocortex is comprised of six layers (Fig. 1.4) that lie parallel to the pial surface.

Layer I, the outer most layer, is termed the molecular layer and contains few neuronal somata, the majority that are present are inhibitory. Additionally, Layer I is composed of dendritic tufts, axons and glia. Layer II/III receives strong feed-forward input from layer IV, which in turn receives strong input from the thalamus. Layer V is the main output layer, projecting to sub-cortical structures. Layer VI

Figure 1.5: The cannonical connectivity of the principal cells of the neocortex. From Harris and Mrsic-Flogel (2013). The figure has been redacted from this version to avoid copyright infringement.

is the deepest layer, and both receives input and provides output to the thalamus. The typical connectivity within the neocortex is an area of intense study, Fig. 1.5 shows a simplified summary, for a review see Harris and Mrsic-Flogel (2013).

Hippocampal and cerebellar tissue was also employed in a number of experiments presented in this thesis. The hippocampus is a cortical structure strongly implicated in memory and navigation. The hippocampus has a well characterised structure (Fig. 1.6) comprising a number of ordered pathways (Strange et al., 2014). These pathways are used for a wide range of investigations because the structure facilitates a convenient stimulus evoked response and it was for this reason that hippocampal tissue was employed here. Finally, cerebellar tissue was used in a number of experiments. The cerebellum (Fig. 1.7) is a posterior structure, implicated in motor control. Cerebellar tissue was employed because one of its constituent cell types, Purkinje cells, fire spontaneously (at a frequency of approximately 50 Hz (Raman and Bean, 1999)) in acute slice (Apps and Garwicz, 2005; De Zeeuw et al., 2011).

Figure 1.6: The hippocampal circuit, showing the well characterised pathways. From Daumas et al. (2009). The figure has been redacted from this version to avoid copyright infringement.

Figure 1.7: The cerebellar circuit, showing the location of Purkinje cells that fire spontaneously in acute slice preparations. From Apps and Garwicz (2005). The figure has been redacted from this version to avoid copyright infringement.

Figure 1.8: The molecular structure of adenosine. From Ralevic and Burnstock (1998). The figure has been redacted from this version to avoid copyright infringement.

1.2 The role of adenosine

The final study in the core of this thesis presents a characterisation of the spatiotemporal dynamics of extracellular adenosine concentration in response to electrographic seizure activity in the neocortex. A brief summary of the current understanding of the role of adenosine will be presented here, for more thorough reviews see Fredholm et al. (2001) and Ralevic and Burnstock (1998).

Adenosine is a purine nucleoside (Fig. 1.8), it is an important signalling molecule, implicated in both physiological and pathological processes. For example, adenosine plays an important role in the regulation of sleep (Huang et al., 2011; Blanco-Centurion et al., 2006; Bjorness and Greene, 2009; Schmitt et al., 2012; Sims et al., 2013), is a powerful vasodilator and an important neuroprotectant implicated in stroke, traumatic brain injury and epilepsy (Pasini et al., 2000; Dale et al., 2000; Frenguelli et al., 2003; Hunter et al., 2003; Pearson et al., 2006; Dale and Frenguelli, 2009; Ross et al., 2014; Winn et al., 1980; During and Spencer, 1992; Van Gompel et al., 2014).

Adenosine activates four types of G-protein coupled receptor: A_1, A_{2A}, A_{2B} and A_3 (Ralevic and Burnstock, 1998; Fredholm et al., 2001), all composed of seven putative transmembrane domains (the structure of the A_1 receptor is shown in Fig. 1.9). Activation of A_1 and A_3 receptors is largely inhibitory while that of A_2 receptors is largely excitatory; A_{2A} receptors are found in the central nervous system and A_{2B} are found in the peripheral nervous system (Wall and Dale, 2008). The EC_{50} values for the four subtypes are 73 nM (Daly and Padgett, 1992); 150 nM (Daly and Padgett, 1992); 5100 nM (Peakman and Hill, 1994) and 6500 nM (Zhou

et al., 1992).

A_1 receptors are particularly abundant in the central nervous system. They are located both pre- and post-synaptically, on cell bodies and on axons. Activation of A_1 receptors has an inhibitory effect on neurotransmission by decreasing the probability of vesicle release and hyperpolarising neuronal membranes (Ralevic and Burnstock, 1998). Adenosine is released during hypoxia and ischemia. The resulting activation of A_1 receptors reduces neuronal activity and, therefore, metabolic demand and as such is neuroprotective. A_1 receptors are also expressed on the heart, activation of these receptors has negative chronotropic and inotropic effects, complicating the use of an A_1 receptor agonist therapeutically to treat excessive neuronal activity such as occurs in epilepsy.

A_{2A} receptors are found in a restricted number of tissues including the central nervous system, particularly the striatum, and vascular smooth muscle. In the central nervous system activation of A_{2A} receptors largely facilitates neurotransmitter release. However, striatal neurons express A_{2A} receptors in close association with dopamine D_2 receptors, activation of these A_{2A} receptors reduces the affinity of the D_2 receptors for dopamine. This has raised the possibility of using A_{2A} receptor antagonists to treat Parkinsons.

A_{2B} receptors are widely expressed at low levels, requiring relatively high concentrations of adenosine for activation. They appear to be implicated in inflammatory responses.

A_3 receptors are also expressed widely and also appear to play a role in inflammatory responses. Activation of hippocampal A_3 receptors has also been shown to desensitise A_1 receptor mediated inhibition (Dunwiddie et al., 1997).

Changes in extracellular adenosine concentration are produced by a number of mechanisms, for reviews see Latini and Pedata (2001) and Wall and Dale (2008). Briefly, adenosine can be released from neurons through equilibritive nucleoside transporters (ENTs) (Wall and Dale, 2013); adenosine can be produced by the dephosphorylation of ATP released by exocytosis from astrocytes (Wall and Dale, 2013) and direct exocytosis of adenosine has been detected in the cerebellum (Klyuch et al., 2012). A number of candidate mechanisms are shown in Fig. 1.10.

Figure 1.9: The structure of the A1 receptor showing seven transmembrane domains, thought to be composed of α-helices. From Ralevic and Burnstock (1998). The figure has been redacted from this version to avoid copyright infringement.

Figure 1.10: Possible mechanisms for activity-dependent adenosine release. (1) ATP released by exocytosis and subsequently dephosphorylated to adenosine in the extracellular space. (2) An intermediate signalling molecule is released by exocytosis and acts on another cell to cause adenosine release. (3) Direct exocytotic release of vesicular adenosine. Additionally, adenosine could be released through equilibritive nucleoside transporters. From Wall and Dale (2008). The figure has been redacted from this version to avoid copyright infringement.

Adenosine is removed either by phosphorylation to AMP by adenosine kinase (ADK) or deamination to inosine by adenosine deaminase (ADA) (Latini and Pedata, 2001). Both ADK and ADA are primarily found intracellularly and act on adenosine once it has entered a cell via ENTs, however, there is also evidence of extracellular ADA (Latini and Pedata, 2001). A summary of some of the pathways of production, metabolism and transport of adenosine are shown in Fig. 1.11.

1.3 Methods for recording neuronal activity

To study network activity in the nervous system a technique is required to measure or infer neuronal activity. Many techniques have been developed, each striking a different balance in the compromise between spatial and temporal resolution; recording duration; the area of the region of interest and the damage or ionic modification caused in the tissue. In this section a number of commonly used techniques will be briefly summarised, however, it should be noted that this is an intense area of research and so the technology available is developing rapidly.

As already discussed, neurons are active electro-chemical systems. To infer neuronal activity, the voltage changes that arise from neuronal activity can be

Figure 1.11: Pathways of adenosine production, metabolism and transport, with indications of the sites of action of various enzyme inhibitors. ADA: Adenosine deaminase; AK: Adenosine kinase; AOPCP: α,β-methylene ADP; DCF: deoxycoformycin; EHNA: erythro-9-(2-hydroxy-3-nonyl)adenosine; es: equilibrative-sensitive nucleoside transporters; ei: equilibrative-insensitive nucleoside transporters; 5-IT: 5-iodotubercidin; NBMPR: nitrobenzyl-thioiniosine; PDE: cAMP phosphodiesterase; SAH: S-adenosyl homocysteine. From Latini and Pedata (2001). The figure has been redacted from this version to avoid copyright infringement.

measured directly, either from single neurons by patch clamp recording or by measuring the averaged contribution from a population of neurons, such as with local field potential (LFP), electrocorticogram (ECoG) or electroencephalogram (EEG) recording. Alternatively neuronal activity can be measured using voltage or calcium sensitive dyes, either loaded in to cells or expressed by the cells themselves. Finally, activity can be inferred from changes in the intrinsic optical properties of brain tissue at the network level, such as with *in vitro* intrinsic optical signal (IOS) imaging, or by the effect of activity on the local perfusion, as with functional magnetic resonance imaging (fMRI) or typical *in vivo* IOS imaging.

The intracellular voltage dynamics of single neurons can be recorded using patch clamp recording techniques (Sakmann and Neher, 1984), using either whole cell, cell attached (Perkins, 2006) or perforated patch (Linley, 2013) configurations. These approaches give high resolution recordings specific to the neurons under investigation. However, the number of simultaneous recordings is limited, the highest number to date is twelve (Anastassiou et al., 2011), this does not give a representative reflection of the activity of the $\sim 10^6$ neurons in a slice of rat cortex.

The potential at any point in or around the brain is a weighted average of contributions from the entire brain. This potential can be measured and its time dependence can be used to make inferences about the underlying network dynamics. When this potential is measured by electrodes on the scalp it is termed the electroencephalogram (EEG), when it is measured by subdural electrodes on the cortical surface it is termed the electrocorticogram (ECoG) and when measured from within the brain, either *in vivo* or *in vitro*, the local field potential (LFP). Whilst this technique does allow activity to be resolved spatially, the contribution at any point includes contributions from all points. The contribution of each monopole scales inversely with distance, spatial localisation is, therefore, limited. However, advances in analysis approaches are improving the recoverable spatial resolution. The advantage of these techniques, however, is that they produce a local spatial average of neuronal activity. When coordinated network activity is of interest, such as in the study of epilepsy, this averaging is highly desirable - the activity of a few single neurons, such as would be obtained from patch clamp recordings, is not as

representative. For a review of these recording modalities see Buzsaki et al. (2012).

Single cell resolution can also be achieved using dye based techniques. The fluorescence characteristics of suitable dyes change in response to changes either in intracellular voltage or intracellular calcium concentration. These changes can then be used to infer neuronal activity. Dyes can either be loaded in to cells directly or the cells can be modified to express the dyes themselves. Dye based techniques allow single cell resolution recording from many more cells than is possible with patch clamp recording. However, dyes bleach with a half life ~ 800 s (Wenjun et al., 2002; Takagaki et al., 2008) and so the recording duration is severely limited. These approaches are, therefore, not suitable for the study of rare spontaneous events, such as seizure onset. For reviews of these techniques see Kerr and Denk (2008) and Knopfel (2012).

Other techniques infer the activity of neurons indirectly. Neuronal activity has an associated metabolic demand and increased neuronal activity has an associated increased metabolic demand. Such variations in metabolic demand can be inferred from the blood oxygen level, this is termed the blood oxygen level dependent (BOLD) signal. The BOLD signal is made up of three components: Immediately after an increase in neuronal activity the ratio of oxy- to deoxy- haemoglobin transiently decreases as a result of increased oxygen consumption. To compensate for this the supply of oxygenated blood then increases. Finally, after the level of neuronal activity has reduced, the blood flow also reduces. The BOLD signal can be detected in a number of ways, for example, using magnetic resonance imaging (MRI) and is the basis of functional MRI (fMRI), for a review see Heeger and Ress (2002). It should be noted, however, that the neurovascular coupling that gives rise to the BOLD signal may be altered in disease states and may vary with age so care is needed when employing this technique (D'Esposito et al., 2003). The BOLD signal, in addition to changes in the oxidation state of cytochrome oxidase, can also be detected spectroscopically and is often termed an intrinsic optical signal (IOS). However, without a craniotomy or cranial window, the scalp and skull limit the signal, but this approach has shown significant promise for measurement in neonates (Edwards et al., 1991; Cooper et al., 1999).

In addition to the BOLD and cytochrome oxidase dependent signals observed *in vivo* there is an additional intrinsic optical signal (IOS) that persists *in vitro* (Gouras, 1958; Aitken et al., 1999; Gurden et al., 2006). A number of mechanisms contribute to this signal. There is a fast change in light scattering that is neuronal in origin and closely tracks the dynamics of the underlying electrical activity (Cohen et al., 1968; Stepnoski et al., 1991; Rector et al., 1997, 2005). However, because of its small signal-to-noise ratio, averaging of many sweeps is required to detect this signal in tissue; it is therefore unsuitable for the study of spontaneous activity. The first response is followed by a slower, much larger, signal that results from a combination of glutamate dependent neuronal and glial swelling, changes in cytoplasmic refractive index and possibly changes in the interactions between macromolecules and organelles (Lipton, 1973; Holthoff and Witte, 1996; Andrew et al., 1999; Buchheim et al., 1999, 2005; Jarvis et al., 1999; Fayuk et al., 2002; Gurden et al., 2006; Kitaura et al., 2009). This signal can be readily measured, however, the temporal dynamics of the signal do not directly reflect the underlying network dynamics. This signal is the subject of Chapter 3 and will be discussed more fully there.

1.4 Preparations used for the study of the nervous system

A wide range of preparations have been developed for the study of the nervous system. Each strikes a different balance between fidelity to the system ultimately of interest, access for recording and the ability to control and manipulate the system to implement experimental protocols.

Ultimately it is the *in vivo* human brain that is of interest, it can be studied directly using non-invasive techniques such as fMRI and EEG and with more invasive approaches, such as ECoG, when they are indicated for clinical reasons and additional data can be obtained without significant modification to the surgical protocol. For example, depth electrodes may be implanted to determine the location of seizure foci for evaluation for resection, (for examples see Truccolo et al. (2011); Van Gompel et al. (2014); Chang et al. (2012)). However, experiments that require

more invasive surgical procedures than clinically indicated or that require otherwise unnecessary pharmacological manipulation are deemed unethical and so cannot be carried out.

Pharmacological manipulation and invasive recording techniques can, however, be applied to *ex vivo* human brain tissue. Resection of the brain is indicated for a number of neurological problems, for example, for the treatment of some cases of pharmacologically refractory focal epilepsy. The tissue removed, after appropriate clinical tests, is often made available for research purposes. This tissue often provides exact insights in to disease processes, rather than only being a model of them. However, the availability of such tissue is limited and clinical considerations must always take precedence over maximising the quality of the samples for research. Additionally, the tissue removed is almost always affected by a disease process and so it is unlikely to be suitable for the study of physiological processes.

Although it is the human brain that is ultimately of interest, the brains of other mammals are thought to provide a good model of human brain function and are widely used for the study of the nervous system. As with human brain, the brains of other mammals can be studied *in vivo*, however, although there are strict ethical controls, where justified, more invasive *in vivo* surgical procedures can be carried out. Furthermore these can be implemented in both healthy animals and those affected by disease as well as in transgenic lines. The access for both recording and manipulation is, however, still limited and so *in vivo* preparations are unsuitable for some protocols. Equally, some protocols do not require *in vivo* measurement and so it would be unethical to use such a preparation.

Typically experiments are either carried out *in vivo*, in tissue slices or in cultured cells. However, an intermediate preparation is possible with the guinea pig brain. The guinea pig brain can be removed and perfused through its circle of Willis, allowing the intact brain to be viably maintained out of the skull, this is termed the isolated brain. This preparation allows improved access and pharmacological manipulation while preserving the complete network connectivity. Access for recording is, however, still more limited than in tissue slice or cell culture.

The acute tissue slice strikes a different balance between fidelity and ac-

cess. The brain of an animal is rapidly removed and, whilst cold, cut in to slices $\sim$ 400 μm thick. The slices are then rewarmed and immersed in an oxygenated artificial cerebrospinal fluid (aCSF) which maintains the viability of the tissue by diffusion. The cutting process severs a large proportion of the network connections, however, sections are cut that maximise connectivity within the slice and such slices exhibit spontaneous activity, indicating a significant degree of connectivity. The advantage of the acute tissue slice preparation is the degree of access to the tissue that it facilitates, both for recording from the tissue and for pharmacological, ionic, electrical and mechanical manipulation. Additionally, all experimentation is carried out once the animal is dead and so the suffering caused is minimised. For these reasons all experiments presented in this thesis that involved animal tissue employed this preparation.

Typically acute tissue slices are only viable on the day of preparation, however, tissue from young animals can be cultured. Cultured slices are termed organotypics and are well suited to the study of slow processes that require direct access to the cells (Gahwiler et al., 1997). For example, cells in culture can be transfected and the effect of expression of a resulting protein can be investigated, a process that would not occur within the time scale of viability of an acute tissue slice. Unlike in cultures of separate cells, some synaptic connections between cells are preserved, allowing the study of synaptic transmission. However, the development of the cells within an organotypic slice can differ from that which would occur *in vivo* so some caution is required.

Finally, cellular processes and ion channel dynamics can be studied in cultured cells, unlike in organotypic cultures, the cells do not form a network and so synaptic transmission can not be studied using this preparation. However, cultured cells are well suited to the study of ion channels and other proteins, such as connexins, as mutant lines can be produced rapidly. Ion channel properties can also be studied in relative isolation by reconstituting them in artificial membranes.

1.5 Seizures

Clinically, an epileptic seizure is defined as an unprovoked transient occurrence of signs or symptoms due to abnormal excessive or synchronous neuronal activity in the brain (Fisher et al., 2005). The signs and symptoms of seizures vary considerably depending on the location and extent of the affected brain area. Seizures are divided in to two main classes: focal seizures, those that are localised to an area of the brain and generalised seizures, those that involve the majority of the cortex. Some seizures do not cause a loss of consciousness, but depending on the location of the seizure activity, may cause motor signs or sensory, autonomic or psychic symptoms, these are termed simple partial seizures (Alarcon et al., 2009). If a focal seizure affects both hemispheres it can impair consciousness, this is then termed a complex partial seizure. Generalised seizures cause a loss of consciousness in addition to one or more of a number of other possible signs, most commonly (in approximately 60% of patients) convulsions. Typically, limbs become rigid for a few seconds (tonic phase) followed by repetitive contractions of all limbs at approximately 3 Hz, where the limbs jerk in one direction followed by a slower movement back to the original position before jerking again (clonic phase) (Alarcon et al., 2009).

The electrographic correlate of seizure symptoms is large amplitude rhythmic activity with time dependent frequency components (an example LFP recording of a seizure *in vitro* is shown in Fig 1.12). Traditionally this was interpreted as the result of hyperexcitability and hypersynchronous neuronal activity. However, more recent work has shown the dynamics of seizure onset, spread and termination to be far more complex and are as yet not fully understood (Pinto et al., 2005; Jiruska et al., 2010a; Zhang et al., 2011). The hallmark of seizure activity appears to be hypersynchronous activity, however, recent studies have shown that there is actually an increase in the heterogeneity of firing at seizure onset and that hypersynchronicty is a feature associated with, and potentially implicated in, seizure termination (Truccolo et al., 2011; Jiruska et al., 2013). Furthermore, whilst seizures may result from an imbalance between excitation and inhibition in favour of excitability, inhibition can promote their characteristic synchronisation. Inhibition can give rise to synchronisation both by GABAergic depolarisation resulting from imbalance of

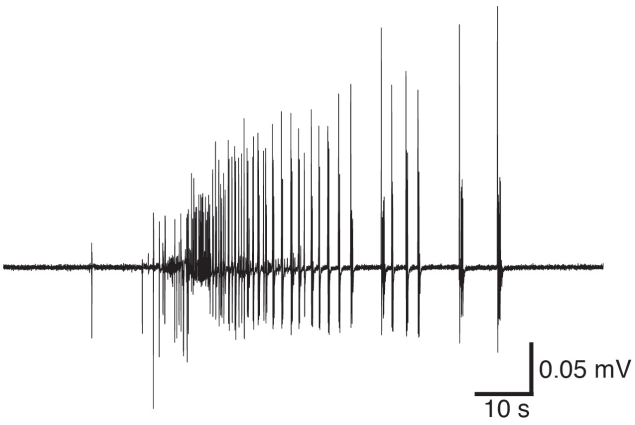

Figure 1.12: The local field potential recorded during a typical burst of electrographic seizure activity in the Mg^{2+} free seizure model in acute neocortical slice.

chloride (Pavlov et al., 2013) and by synchronous recovery from inhibition of a larger population of principal neurons (Klaassen et al., 2006). The propagation of seizures is also complex and involves all three known mechanisms of neuronal coupling: chemical synapses, gap junctions and ephaptic coupling. Propagation can even occur independently of both chemical synapses and gap junctions (Jefferys and Haas, 1982; Zhang et al., 2014). During ictal events interacting networks appear to coalesce and fragment (Kramer et al., 2010), similarly seizure may involve a micro to macro seizure transition (Stead et al., 2010).

Understanding seizure dynamics is of fundamental scientific interest, but also of significant practical importance. An understanding of seizure onset, particularly identification of the features of pre-ictal states, would facilitate the implementation of systems to predict seizures. Temporally targeted therapy could then be provided to prevent the seizure occurring or a system could warn the patient of the impending event so that they could take steps to avoid injury during the seizure. Greater understanding of the mechanisms that cause seizure termination could be used to inform the development of improved anti-epileptic therapies.

1.6 Epilepsy

Epilepsy is a disorder of the brain characterised by an enduring predisposition to unprovoked seizures (Fisher et al., 2005). It is not a single condition, rather a term for any disorder that gives rise to unprovoked seizures. Pragmatically, an individual

is diagnosed with epilepsy if they have two or more unprovoked epileptic seizures within a period of two years (Alarcon et al., 2009).

Epilepsy is broadly classified on the basis of its cause. Some types of epilepsy are genetic, for example, Dravet's syndrome is caused by a mutation in the sodium channel αI subunit gene SCN1A (Depienne et al., 2009; Dravet, 2011; Marini et al., 2011). Other types of epilepsy are termed symptomatic - the result of an insult to the brain, for example, febrile infection related epilepsy syndrome (FIRES) - the development of epilepsy by a school age child as the result of a period of status epilepticus caused by a fever (Kramer et al., 2011; van Baalen et al., 2012; Serrano-Castro et al., 2013). Finally, epilepsy can be idiopathic.

Although it is not completely understood, a number of processes have been implicated in epileptogenesis. For example, granule cell dispersion, mossy fibre sprouting, raised intracellular chloride potentials and astrogliosis and associated ADK up regulation have all been observed (Pitkanen and Lukasiuk, 2011; Boison, 2008).

There are three approaches to the treatment of epilepsy: pharmacological, surgical and electrical. Anti-epileptic drugs work via a variety of mechanisms, for example, benzodiazepines work by enhancing inhibition by allosteric modulation of $GABA_A$ receptors, gabapentin works by binding to the $\alpha 2\delta$ subunit of the voltage-gated calcium channels and reduces synaptic release of glutamate. Resection can be carried out to treat some cases of focal epilepsy. Finally, use of electrical stimulation shows promise in treating epilepsy (Alarcon et al., 2009; Jiruska et al., 2010b). Currently it is estimated that 30% of patients with epilepsy would still suffer from seizures even with optimal treatment (Deacon, 2011), however, recent studies of the mechanisms of pharmacological resistance have implicated P-glycoprotein (Loscher, 2005; Volk and Loscher, 2005; Brandt et al., 2006) and combined treatment with both an anti-epileptic drug and a P-glycoprotein inhibitor has shown significant promise (Potschka et al., 2002).

Epilepsy is a common disorder, affecting approximately 50 million people worldwide (Scott et al., 2001), causing a significant detrimental effect on the quality of life of affected individuals and also a significant financial cost. In the UK the

incidence of epilepsy is approximately 51 per 100,000 of population per year, the prevalence of epilepsy is around 1 in 103 people (1 in 242 for those under 18 years) and approximately 600,000 people take anti-epileptic drugs (Deacon, 2011). In the UK 1,150 people died of epilepsy related causes in 2009, the average number of years of life lost per person was 30.2 (Deacon, 2011). In England, Wales and Scotland 69,700 people with epilepsy were claiming disability living allowance in 2009. This cost $\sim$ £244 million per year (Deacon, 2011).

1.7 Models of epilepsy

Numerous models have been developed to replicate the features of epilepsy. These range from *in vivo* models, through acute slice models and dissociated cells, to cultures of transgenic cells and computational models. For example, lateral fluid percussion is used in rats as a model of post-traumatic epilepsy. In contrast, cell cultures are used to study the properties of ion channels arising from genes mutated to reflect those causing genetic epilepsies. For thorough reviews of experimental and computational models of epilepsy see Pitkanen et al. (2006) and Soltesz and Staley (2008) respectively.

In this thesis the hypomagnesemic seizure model (Mody et al., 1987) was employed in acute slice of the rat neocortex. This model produces spontaneous seizures in neocortical tissue from wild type rats without any pretreatment *in vivo*. Mg^{2+} ions block N-methyl-D-aspartate receptor channels, by removing this block neocortical tissue becomes more excitable and spontaneous electrographic seizures occur in the neocortex after approximately 20 minutes. This model exhibits the spatio-temporal dynamics that were of interest here, while causing minimal suffering to the animals and so was used for each of the projects presented here.

1.8 Thesis outline

This is a thesis 'based on published work' as per MOAC Doctoral Training Centre, University of Warwick, regulations. It is comprised of three papers, Chapters 2, 3 and 4, that are either published, in review or in preparation. Chapter 2 presents

a device for the perfusion of *in vitro* tissue with multiple solutions, providing an entirely *in vitro* model of focal epilepsy. Chapter 3 presents a transformation to convert the slow dynamics of intrinsic optical signals *in vitro* to the form of the local field potential, facilitating the study of the spatio-temporal dynamics of focal seizure activity *in vitro*. Chapter 4 presents the application of the transformation derived in Chapter 3 to the study of the spatio-temporal dynamics of extracellular adenosine release in response to electrographic seizure activity *in vitro*.

Finally the appendices of this thesis contain four additional papers. These papers are not related to the core of this thesis but are projects to which I made a significant contribution and so are included for completeness. These studies demonstrate the potential for Field Asymmetric Ion Mobility Spectrometry (FAIMS) in medical diagnosis. FAIMS is a highly sensitive tool for chemical detection, originally applied to the detection of chemical warfare agents. FAIMS is able to detect a broad range of chemicals at concentrations below one part per billion. As such, FAIMS was thought to have significant potential in medical diagnosis, however, this had never been explored due to the challenge of the analysis of FAIMS spectra from complex biological mixtures. Our studies provide a proof of principle that biological mixtures can be distinguished using FAIMS (Appendix B) and then apply it to identify inflammatory bowel diseases (Appendix C), patients at risk of high gastrointestinal toxicity in response to radical pelvic radiotherapy (Appendix D) and patients with colorectal cancer (Appendix E).

Bibliography

Aitken, P., Fayuk, D., Somjen, G. G., and Turner, D. Use of intrinsic optical signals to monitor physiological changes in brain tissue slices. *Methods*, 18:91–103, 1999.

Alarcon, G., Nashef, L., Cross, H., Nightingale, J., and Richardson, S. *Epilepsy*. Oxford University Press, 2009.

Anastassiou, C., Perin, R., Markram, H., and Koch, C. Ephaptic coupling of cortical neurons. *Nature Neuroscience*, 14:217–224, 2011.

Andrew, R., Jarvis, C., and Obeidat, A. Potential sources of intrinsic optical signals imaged in live brain slices. *Methods*, 18(2):185 – 196, 1999. ISSN 1046-2023.

Apps, R. and Garwicz, M. Anatomical and physiological foundations of cerebellar information processing. *Nature Reviews Neuroscience*, 6:297–311, 2005.

Bean, B. The action potential in mammalian central neurons. *Nature Reviews Neuroscience*, 8:451–465, 2007.

Bjorness, T. and Greene, R. Adenosine and sleep. *Current Neuropharmacology*, 7: 238–245, 2009.

Blanco-Centurion, C., Xu, M., Murillo-Rodriguez, E., Gerashchenko, D., Shiromani, A., Salin-Pascual, R., Hof, P., and Shiromani, P. Adenosine and sleep homeostasis in the basal forebrain. *The Journal of Neuroscience*, 26:8092–8100, 2006.

Boison, D. The adenosine kinase hypothesis of epileptogenesis. *Progress in Neurobiology*, 84:249–262, 2008.

Brandt, C., Bethmann, K., Gastens, A., and Loscher, W. The multidrug transporter

hypothesis of drug resistance in epilepsy: Proof-of-principle in a rat model of temporal lobe epilepsy. *Neurobiology of Disease*, 24:202–211, 2006.

Briar, C., Lasserson, D., Gabriel, C., and Sharrack, B. *Nervous System*. Mosby, 2003.

Buchheim, K., Schuchmann, S., Siegmund, H., Gabriel, H., Heinemann, U., and Meierkord, H. Intrinsic optical signal measurements reveal characteristic features during different forms of spontaneous neuronal hyperactivity associated with ECS shrinkage in vitro. *Eur, J. Neurosci.*, 11:1877–1882, 1999.

Buchheim, K., Wessel, O., Siegmund, H., Schuchmann, S., and Meierkord, H. Processes and components participating in the generation of intrinsic optical signal changes in vitro. *European Journal of Neuroscience*, 22:125–132, 2005.

Buzsaki, G., Anastassiou, C., and Kocj, C. The origin of extracellular fields and currents - EEG, ECog, LFP and spikes. *Nature Reviews Neuroscience*, 13:407–420, 2012.

Cajal, S. *Comparative study of the sensory areas of the human cortex*. 1899.

Chang, S., Kim, I., Marsh, M., Jang, D., Hwang, S., Van Gompel, J., Goerss, S., Kimble, C., Bennet, K., Garris, P., Blaha, C., and Lee, K. Wireless fast-scan cyclic voltammetry to monitor adenosine in patients with essential tremor during deep brain stimulation. *Mayo Clinic Proceedings*, 87:760–765, 2012.

Clarke, L. and Barres, B. Emerging roles of astrocytes in neural circuit development. *Nature Reviews Neuroscience*, 14:311–321, 2013.

Cohen, L., Keynes, R., and B., H. Light scattering and birefringence changes during nerve activity. *Nature*, 218:438 – 441, 1968.

Cooper, C., Cope, M., Springett, R., Amess, P., Penrice, J., Tyszczuk, L., Punwani, S., Ordidge, R., Wyatt, J., and Delpy, D. Use of mitochondrial inhibitors to demonstrate that cytochrome oxidase near-infrared spectroscopy can measure mitochondrial dysfunction non-invasively in the brain. *Journal of Cerebral Blood Flow and Metabolism*, 19:27–38, 1999.

Dale, N. and Frenguelli. Release of adenosine and ATP during ischemia and epilepsy. *Current Neuropharmacology*, 7:160–179, 2009.

Dale, N., Pearson, T., and Frenguelli, B. Direct measurement of adenosine release during hypoxia in the CA1 region of the rat hippocampal slice. *Journal of Physiology*, 526:143–155, 2000.

Daly, J. and Padgett, W. Agonist activity of 2- and 5′-substituted adenosine analogs and their N^6-cycloalkyl derivatives at A_1- and A_2-adenosine receptors coupled to adenylate cyclase. *Biochem Pharmacol*, 43:1089–1093, 1992.

Daumas, S., Ceccom, J., Halley, H., Frances, B., and Lassalle, J.-M. Activation of metabotropic glutamate receptor type 2/3 supports the involvement of the hippocampal mossy fiber pathway on contextual fear memory consolidation. *Learning and Memory*, 16:504–507, 2009.

De Zeeuw, C., Hoebeek, F., Bosman, L., Schonewille, M., Witter, L., and Koekkoek, K. Spatiotemporal firing patterns in the cerebellum. *Nature Reviews Neuroscience*, 12:327–344, 2011.

Deacon, K. Epilepsy prevalence, incidence and other statistics. Technical report, Joint Epilepsy Council, September 2011.

Depienne, C., Trouillard, O., Saint-Martin, C., Gourfinkel-An, I., Bouteiller, D., Carpentier, W., Keren, B., Abert, B., Gautier, A., Baulac, S., Arzimanoglou, A., Cazeneuve, C., Nabbout, R., and LeGuern, E. Spectrum of SCN1A gene mutations associated with Dravet syndrome: analysis of 333 patients. *Journal of Medical Genetics*, 46:183–191, 2009.

D'Esposito, M., Deouell, L., and Gazzaley, A. ALterations in the bold fMRI signal with ageing and disease: A challenge for neuroimaging. *Nature Reviews Neuroscience*, 4:863–872, 2003.

Dravet, C. The core Dravet syndrome phenotype. *Epilepsia*, 52:3–9, 2011.

Dunwiddie, T., Diao, L., Kim, H., Jiang, J., and Jacobson, K. Activation of hip-

pocampal adenosine A_3 receptors produces a desensitization of A_1 receptor- mediated responses in rat hippocampus. *Journal of Neuroscience*, 17:607–614, 1997.

During, M. and Spencer, D. Adenosine: A potential mediator of seizure arrest and postictal refractoriness. *Annals of Neurology*, 32:618–624, 1992.

Edwards, A., Brown, G., Cope, M., Wyatt, J., McCormick, D., Roth, S., Delpy, D., and Reynolds, E. Quantification of concentration changes in neonatal human cerebral oxidized cytochrome oxidase. *Journal of Applied Physiology*, 71:1907–1913, 1991.

Fayuk, D., Aitken, P., Somjen, G., and Turner, D. Two different mechanisms underlie reversible, intrinsic optical signals in rat hippocampal slices. *J. Neurophysiol.*, 87:1924–1937, 2002.

Fisher, R., van Emde Boas, W., Blume, W., Elger, C., Genton, P., Lee, P., and Engel, J. Epileptic seizures and epilepsy: Definitions proposed by the International League Against Epilepsy (ILAE) and the International Bureau for Epilepsy (IBE). *Epilepsia*, 46:470–472, 2005.

Fredholm, B., Ijzerman, A., Jacobson, K., Klotz, K.-N., and Linden, J. International union of pharmacology. xxv. nomenclature and classification of adenosine receptors. *Pharmacological Reviews*, 53:527–552, 2001.

Frenguelli, B., Lllaudet, E., and Dale, N. High-resolution real-time recording with microelectrode biosensors reveals novel aspects of adenosine release during hypoxia in rat hippocampal slices. *Journal of Neurochemistry*, 86:1506–1515, 2003.

Gahwiler, B., Capogna, M., Debanne, D., McKinney, R., and Thompson, S. Organotypic slice cultures: a technique has come of age. *Trends in Neuroscience*, 20: 471–477, 1997.

Gouras, P. Spreading depression of activity in amphibian retina. *Am. J. Physiol.*, 195:28–32, 1958.

Gurden, H., Uchida, N., and Mainen, Z. Sensory-evoked intrinsic optical signals

in the olfactory bulb are coupled to glutamate release and uptake. *Neuron*, 52: 335–345, 2006.

Harris, K. and Mrsic-Flogel, T. Cortical connectivity and sensory coding. *Nature*, 503:51–58, 2013.

Haydon, P. Glia: listening and talking to the synapse. *Nature Reviews Neuroscience*, 2:185–193, 2001.

Heeger, D. and Ress, D. What does fMRI tell us about neuronal activity? *Nature Reviews Neuroscience*, 3:142–151, 2002.

Holthoff, K. and Witte, O. Intrinsic optical signals in rat neocortical slices measured with near-infrared dark-field microscopy reveal changes in extracellular space. *J. Neurosci.*, 16:2740–2749, 1996.

Huang, Z., Urade, Y., and Hayaishi, O. The role of adenosine in the regulation of sleep. *Current Topics in Medicinal Chemistry*, 11:1047–1057, 2011.

Hunter, C., Bennet, L., Power, G., Roelfsema, V., Blood, A., Quaedackers, J., George, S., Guan, J., and Gunn, A. Key neuroprotective role for endogenous A_1 receptor activation during asphyxia in the fetal sheep. *Stroke*, 34:2240–2245, 2003.

Jarvis, C., Lilge, L., Vipond, G., and Andrew, R. Interpretation of intrinsic optical signals and calcein fluorescence during acute excitotoxic insult in the hippocampal slice. *Neuroimage*, 10:357–372, 1999.

Jefferys, J. and Haas, H. Synchronised bursting of CA1 hippocampal pyramidal cells in the absence of synaptic transmission. *Nature*, 300:448–450, 1982.

Jiruska, P., Csicsvari, J., Powell, A., Fox, J., Chang, W.-C., Vreugdenhil, M., Xiaolia, L., Palus, M., Bujan, A., Dearden, R., and Jefferys, J. High-frequency network activity, global increase in neuronal activity and synchrony expansion precede epileptic seizures *in vitro*. *Journal of Neuroscience*, 30:5690–5701, 2010a.

Jiruska, P., Powell, A., Deans, J., and Jefferys, J. Effects of direct brain stimulation depend on seizure dynamics. *Epilepsia*, 51:93–97, 2010b.

Jiruska, P., de Curtis, M., Jefferys, J., Schevon, C., Schiff, S., and Schindler, K. Synchronization and desynchronization in epilepsy: controversies and hypotheses. *Journal of Physiology*, 591:787–797, 2013.

Kandel, E., Schwartz, J., Jessell, T., Siegelbaum, S., and Hudspeth, A. *Principles of neural science*. McGraw-Hill, 2013.

Kerr, J. and Denk, W. Imaging *in vivo*: watching the brain in action. *Nature Reviews Neuroscience*, 9:195–205, 2008.

Kitaura, H., Tsujita, M., Huber, V., Kakita, A., Shibuki, K., Sakimura, K., Kwee, I., and Nakada, T. Activity-dependent glial swelling is impaired in aquaporin-4 knockout mice. *Neurosci. Res.*, 64:208–212, 2009.

Klaassen, A., Glykys, J., Maguire, J., Labarca, C., Mody, I., and Boulter, J. Seizures and enhanced cortical GABAergic inhibition in two mouse models of human autosomal dominant nocturnal frontal lobe epilepsy. *Proceedings of the National Academy of Sciences of the USA*, 103:19152–19157, 2006.

Klyuch, B., Dale, N., and Wall, M. Deletion of ecto-5′-nucleotidase (CD73) reveals direct action potential dependent adenosine release. *Journal of Neuroscience*, 32: 3842–3847, 2012.

Knopfel, T. Genetically encoded optical indicators for the analysis of neuronal circuits. *Nature Reviews Neurocience*, 13:687–700, 2012.

Kramer, M., Eden, U., Kolaczyk, E., Zepeda, R., Eskandar, E., and Cash, S. Coalescence and fragmentation of cortical networks during focal seizures. *Journal of Neuroscience*, 30:10076–10085, 2010.

Kramer, U., Chi, C.-S., Lin, K.-L., Specchio, N., Sahin, M., Olson, H., Nabbout, R., Kluger, G., Lin, J.-J., and van Baalen, A. Febrile infection related epilepsy syndrome (FIRES): Pathogenesis, treatment, and outcome: A multicenter study on 77 children. *Epilepsia*, 52:1956–1965, 2011.

Lamprecht, R. and LeDoux, J. Structural plasticity and memory. *Nature Reviews Neuroscience*, 5:45–54, 2004.

Latini, S. and Pedata, F. Adenosine in the central nervous system: release mechanisms and extracellular concentrations. *Journal of Neurochemistry*, 79:463–484, 2001.

Linley, J. Perforated whole-cell patch-clamp recording. *Methods in Molecular Biology*, 998:149–157, 2013.

Lipton, P. Effects of membrane depolarization on light scattering by cerebral cortical slices. *J. Physiol.*, 231:365–383, 1973.

Lisman, J., Raghavachari, S., and Tsien, R. The sequence of events that underlie quantal transmission at central glutamatergic synapses. *Nature Reviews Neuroscience*, 8:597–609, 2007.

Loscher, W. Drug resistance in brain diseases and the role of drug efflux transporters. *Nature Reviews Neuroscience*, 6:591–602, 2005.

Marini, C., Scheffer, I., Nabbout, R., Suls, A., De Jonge, P., Zara, F., and Guerrini, R. The genetics of Dravet syndrome. *Epilepsia*, 52:24–29, 2011.

Mody, I., Lambert, J., and Heinemann, U. Low extracellular magnesium induces epileptiform activity and spreading depression in rat hippocampal slices. *Journal of Neurophysiology*, 57:869–888, 1987.

Pasini, F., Guideri, F., Picano, E., Parenti, G., Petersen, C., and Varga, T., A. abd Perri. Increase in plasma adenosine during brain ischemia in man: A study during transient ischemic attacks, and stroke. *Brain Research Bulletin*, 51:327–330, 2000.

Pavlov, I., Kaila, K., Kullmann, D., and Miles, R. Cortical inhibition, pH and cell excitability in epilepsy: what are optimal targets for antiepileptic interventions? *Journal of Physiology*, 591:765–774, 2013.

Peakman, M. and Hill, S. Adenosine A_{2B}-receptor-mediated cyclic AMP accumulation in primary rat astrocytes. *British Journal Pharmacology*, 111:191–198, 1994.

Pearson, T., Damian, K., Lynas, R., and Frenguelli, B. Sustained elevation of extracellular adenosine and activation of A1 receptors underlie post-ischaemic inhibi-

tion of neuronal function in rat hippocampus *in vitro*. *Journal of Neurochemistry*, 97:1357–136, 2006.

Pereda, A. Electrical synapses and their functional interactions with chemical synapses. *Nature Reviews Neuroscience*, 15:250–263, 2014.

Perkins, K. Cell-attached voltage-clamp and current-clamp recording and stimulation techniques in brain slices. *Journal of Neuroscience Methods*, 154:1–18, 2006.

Pinto, D., Patrick, S., Huang, W., and Connors, B. Initiation, propagation, and termination of epileptiform activity in rodent neocortex *in vitro* involve distinct mechanisms. *Journal of Neuroscience*, 25:8131–8140, 2005.

Pitkanen, A. and Lukasiuk, K. Mechanisms of epileptogenesis and potential treatment targets. *Lancet Neurology*, 10:173–186, 2011.

Pitkanen, A., Schwartzkroin, P., and Moshe, S. *Models of seizures and epilepsy*. Elsevier Academic Press, 2006.

Potschka, H., Fedrowitz, M., and Loscher, W. P-glycoprotein-mediated efflux of phenobarbital, lamotrigine, and felbamate at the blood-brain barrier: evidence from microdialysis experiments in rats. *Neuroscience Letters*, 327:173–176, 2002.

Ralevic, V. and Burnstock, G. Receptors for purines and pyrimidines. *Pharmacological reviews*, 50:413–492, 1998.

Raman, I. and Bean, B. Ionic currents underlying spontaneous action potentials in isolated cerebellar Purkinje neurons. *The Journal of Neuroscience*, 19:1663–1674, 1999.

Rector, D., Poe, G., Kristensen, M., and Harper, R. Light scattering changes follow evoked potentials from hippocampal schaffer collateral stimulation. *J. Neurophysiol.*, 78:1707 – 1713, 1997.

Rector, D., Carter, K., Volegov, P., and George, J. Spatio-temporal mapping of rat whisker barrels with fast scattered light signals. *NeuroImage*, 26:619 – 627, 2005.

Ribrault, C., Sekimoto, K., and Triller, A. From the stochasticity of molecular processes to the variability of synaptic transmission. *Nature Reviews Neuroscience*, 12:375–387, 2011.

Ross, A., Nguyen, M., Privman, E., and Venton, B. Mechanical stimulation evokes rapid increases in adenosine concentration in the prefrontal cortex. *Journal of Neurochemistry*, 130:50–60, 2014.

Sakmann, B. and Neher, E. Patch clamp techniques for studying ionic channels in excitable membranes. *Annual Review of Physiology*, 46:455–472, 1984.

Schmitt, L., Sims, R., Dale, N., and Haydon, P. Wakefulness affects synaptic and network activity by increasing extracellular astrocyte-derived adenosine. *Journal of Neuroscience*, 32:4417–4425, 2012.

Scott, R., Lhatoo, S., and Sander, J. The treatment of epilepsy in developing countries: where do we go from here? *Bulletin of the World Health Organisation*, 79:344–351, 2001.

Serrano-Castro, P., Quiroga-Subirana, P., Payan-Ortiz, M., and Fernandez-Perez, J. The expanding spectrum of febrile infection-related epilepsy syndrome (FIRES). *Seizure*, 22:153–155, 2013.

Sims, R., Wu, H., and Dale, N. Sleep-wake sensitive mechanisms of adenosine release in the basal forebrain of rodents: An *In Vitro* Study. *PLoS One*, 8:e53814, 2013.

Sohl, G., Maxeiner, S., and Willecke, K. Expression and functions of neuronal gap junctions. *Nature Reviews Neuroscience*, 6:191–200, 2005.

Soltesz, I. and Staley, K. *Computational neuroscience in epilepsy*. Elsevier Academic Press, 2008.

Stead, M., Bower, M., Brinkman, B., Lee, K., Marsh, R., Meyer, F., Litt, B., Van Gompel, J., and Worrell, G. Microseizures and the spatiotemporral scales of human partial epilepsy. *Brain*, 133:2789–2797, 2010.

Stepnoski, R., LaPorta, A., Raccuia-Behling, F., Blonder, G., Slusher, R., and Kleinfeld, D. Noninvasive detection of changes in membrane potential in cultured neurons by light scattering. *Proc. Natl. Acad. Sci. USA*, 88:9382 – 9386, 1991.

Strange, B., Witter, M., Lein, E., and Moser, E. Functional organization of the hippocampal longitudinal axis. *Nature Reviews Neuroscience*, 15:655–669, 2014.

Takagaki, K., Lippert, M., Dann, B., Wagner, T., and Ohi, F. Normalization of voltage-sensitive dye signal with functional activity measures. *PLos ONE*, 3: e4041, 2008.

Truccolo, W., Donoghue, J., Hochberg, L., Eskandar, E., Madsen, J., Anderson, W., Brown, E., Halgren, E., and Cash, S. Single-neuron dynamics in human focal epilepsy. *Nature Neuroscience*, 14:635–641, 2011.

van Baalen, A., Husler, M., Plecko-Startinig, B., Strautmanis, J., Vlaho, S., Gebhardt, B., Rohr, A., Abicht, A., Kluger, G., Stephani, U., Probst, C., Vincent, A., and Bien, C. Febrile infection-related epilepsy syndrome without detectable autoantibodies and response to immunotherapy: a case series and discussion of epileptogenesis in FIRES. *Neuropediatrics*, 43:209–216, 2012.

Van Gompel, J., Bower, M., Worrell, G., Stead, M., Chang, S.-Y., Goerss, S., Kim, I., Bennet, K., Meyer, F., Marsh, W., Blaha, C., and Lee, K. Increased cortical extracellular adenosine correlates with seizure termination. *Epilepsia*, 55:233–244, 2014.

Volk, H. and Loscher, W. Multidrug resistance in epilepsy: rats with drug-resistant seizures exhibit enhanced brain expression of P-glycoprotein compared with rats with drug-responsive seizures. *Brain*, 128:1358–1368, 2005.

Volterra, A. and Meldolesi, J. Astrocytes, from brain glue to communication elements: the revolution continues. *Nature Reviews Neuroscience*, 6:626–640, 2005.

Wall, M. and Dale, N. Activity-dependent release of adenosine: A critical re-evaluation of mechanism. *Current Neuropharmacology*, 6:329–337, 2008.

Wall, M. and Dale, N. Neuronal transporter and astrocytic ATP exocytosis underlie activity-dependent adenosine release in the hippocampus. *Journal of Physiology*, 591:3853–3871, 2013.

Wenjun, J., Zhang, R.-J., and Wu, J.-Y. Voltage-sensitive dye imaging of population neuronal activity in cortical tissue. *Journal of Neuroscience Methods*, 115:13 – 27, 2002.

Winn, H., Welsh, J., Rubio, R., and Berne, R. Changes in brain adenosine during bicuculine-induced seizures in rats. *Circulation Research*, 47:568–577, 1980.

Zhang, M., Ladas, T., Qiu, C., Shivacharan, R., Gonzalez-Reyes, L., and Durand, D. Propagation of epileptiform activity can be independent of synaptic transmission, gap junctions, or diffusion and is consistent with electrical field transmission. *Journal of Neuroscience*, 34:1409–1419, 2014.

Zhang, Z., Valiante, T., and Carlen, P. Transition to seizure from 'macro' to 'micro' mysteries. *Epilepsy Research*, 97:290–299, 2011.

Zhou, Q., Li, C., Olah, M., Johnson, R., Stiles, G., and Civelli, O. Molecular cloning and characterization of an adenosine receptor: The A_3 adenosine receptor. *Proceedings of the National Academy of Sciences of the USA*, 89:7432–7436, 1992.

Chapter 2

A chamber for the perfusion of *in vitro* tissue with multiple solutions

The acute neural tissue slice is a widely used preparation, providing a powerful compromise between invasiveness, access and control. Tissue can readily be treated, both locally and globally, pharmacologically or with changes in ionic conditions. However, it is harder to manipulate the environment of regions of tissue on the intermediate scale, that of areas comprising a significant proportion, but not the whole, of a tissue slice. Manipulation of the perfusing aCSF on this scale could be used, for example, as a model of focal epilepsy. An excitant solution could be applied to part of a tissue slice, to induce electrographic seizure activity in that region, while the remainder of the slice was perfused with a standard aCSF. The propagation of the pathological activity from the activated region in to the otherwise quiescent tissue could then be studied. A chamber was developed by Blake *et al.* (2007) to enable the manipulation of the environment of extended regions of tissue. However, the system developed by Blake *et al.* entirely encapsulated the tissue slice except for a single edge. Micro-electrode recordings could, therefore, only be made from that single edge.

We developed a chamber that allows the manipulation of the environment of extended regions (> 5 mm^2) of a tissue slice, whilst maintaining access to the tissue

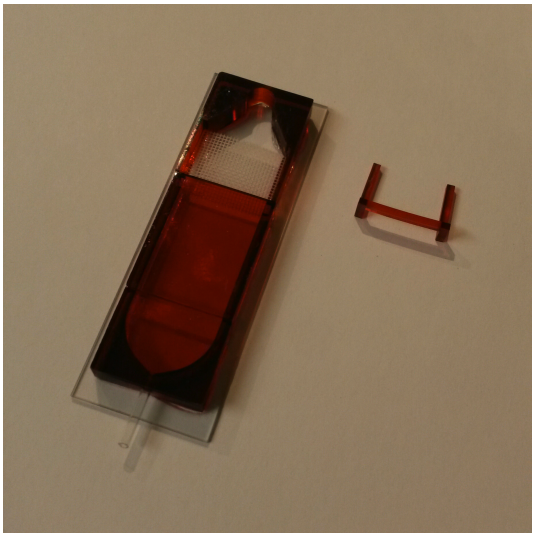

Figure 2.1: The chamber produced for Prof. Frenguelli, University of Warwick. For scale, the chamber is mounted on a standard 26×75 mm microscope slide.

slice for micro-electrodes. This chapter contains the published paper describing this work. Some preliminary development of the chamber was included in a submission for an MSc, however, neither this chamber design, nor any of the data, analysis or text presented here were included in the submission. I designed the chamber, planned and carried out the experiments, carried out the data analysis and wrote the paper. The design, manufacture and initial testing of the chamber was carried out under the supervision of Dr James Covington, the planning and implementation of the biological testing of the chamber was carried out under the supervision of Dr Mark Wall.

After publication of this work, a commission was received from Prof. Bruno Frenguelli, University of Warwick, for a similar device. As shown in our study, the typical design of commercially available chambers results in turbulent flow across tissue slices, resulting in areas of stagnant solution. Prof. Frenguelli required a chamber that avoided this problem, to facilitate stable prolonged recordings for the study of long term potentiation. For this purpose we produced a modified version of the chamber we developed to generate laminar flow across tissue slices (Fig. 2.1).

A chamber for the perfusion of *in vitro* tissue with multiple solutions

Matthew G. Thomas[1,2,3], James A. Covington[2] and Mark J. Wall[1]

[1] School of Life Sciences, [2] School of Engineering, [3] MOAC Doctoral Training Centre, University of Warwick, CV4 7AL, United Kingdom

2.1 Abstract

There are currently no practical systems that allow extended regions (> 5 mm^2) of a tissue slice *in vitro* to be exposed, in isolation, to changes in ionic conditions or to pharmacological manipulation. Previous work has only achieved this at the expense of access to the tissue for recording electrodes. Here we present a chamber that allows a tissue slice to be maintained in multiple solutions, at physiological temperatures, and preserves the ability to record from the slice. We demonstrate the effectiveness of the tissue bath with respect to minimising the mixing of the solutions, maintaining the viability of the tissue and preserving the ability to simultaneously record from the slice.

2.2 Introduction

The acute neural tissue slice is a valuable and widely used experimental preparation (Huang et al., 2012). Tissue, *in vitro*, is typically maintained in a chamber where it is perfused with an oxygenated solution (Croning and Haddad, 1998). The ability to manipulate the tissue environment both focally and globally with changes to ionic conditions or pharmacological manipulation, in addition to electrical stimulation and electrophysiological recording, is a useful tool to elucidate tissue properties in health and disease (Scott et al., 2013). Fluid manipulation on these scales is the domain of microfluidics. The field of microfluidics potentially provides a powerful set of tools for such manipulations and is therefore currently being adopted by neuroscientists (Ahrar et al., 2013). A thorough review of microfluidic techniques applied to brain tissue slices is given in Huang et al. (Huang et al., 2012). Recent examples of the application of microfluidics in neuroscience applications include

focal pharmacological manipulation on the micron scale, less invasively than with conventional glass micropipettes (Mohammed et al., 2008; Queval et al., 2010; Tang et al., 2011) and improved perfusion of tissue slices allowing thicker tissue slices to be viably be maintained (Choi et al., 2007; Hill and Greenfield, 2011).

The global conditions of a tissue slice can be simply altered by changing the solution supplied to the tissue bath. The environment of regions of tissue on the scale of single cells can be modified using pressure ejection systems and micropipettes (Smith and Cunningham, 1983; Salierno et al., 2007) as well as by microfluidic approaches (Queval et al., 2010). However, the ability to expose an extended region (> 5 mm^2) within a tissue slice to a change in conditions is limited. Work by Blake et al. (Blake et al., 2007) used laminar flow to successfully maintain adjacent regions of tissue in different media. Their device did not, however, facilitate recording from the tissue surface. Access for recording electrodes was only possible along a single edge of the tissue. This was satisfactory for the medullary slices that were studied. However, for many applications access for recording electrodes to the tissue surface is essential (Rutecki et al., 1985; Mody et al., 1987).

An example of an application of a chamber capable of exposing an extended region (> 5 mm^2) within a tissue slice to a change in conditions is in the study of the propagation of epileptiform activity across neural tissue. Epileptiform activity is commonly induced in neural tissue by the modification of the perfusing medium (Jefferys and Haas, 1982; Konnerth et al., 1984). A chamber that perfuses regions of a tissue slice with different media would allow the study of the propagation of epileptiform activity, in the region treated with excitant solution, into an adjacent region, maintained in physiological medium. This provides a model for the study of the generalisation of focal seizure activity.

Here we present a tissue bath that utilises laminar flow to maintain adjacent regions of tissue in different media, whilst maintaining both the viability of the tissue and the ability to record from its surface. Such targeting has application in a wide range of network studies involving neural tissue, and also has applications in the study of, for example, uterine and cardiac tissue. The chamber was manufactured using microstereolithography (MSL), a rapid direct digital manufacturing technique.

This allowed bespoke chambers to be manufactured in less than 12 hours.

2.3 Materials and methods

The requirements of the chamber were to:

1. Expose extended regions (> 5 mm^2) within a tissue slice to different solutions, minimising mixing at the interface between the solutions.
2. Allow access to the tissue surface for recording.
3. Perfuse both sides of the tissue to maintain its viability.
4. Maintain the tissue at a physiological temperature.

Design considerations

The chamber is composed of long, high surface area to volume ratio, inflow channels prior to an accessible bath region (Figure 2.2A). The channels were designed to minimise the Reynolds number of the perfusing medium flowing through them, whilst allowing sufficient flow to maintain the viability of the tissue in the chamber. The purpose of the reduced Reynolds number flow is to eliminate turbulence prior to entry to the bath region. It was hypothesised (and tested, detailed below) that longer in-flow channels would correspond to reduced mixing in the bath region. For practicality, the size of the bath was limited to the area of a standard microscope slide (75 mm x 25 mm). The length of the chamber's channels was maximised, given the overall size constraint and the size requirement of the bath region. This gave channels 37.2 mm long. The channels were 4 mm high and, for a two channel chamber, 8.15 mm wide. For a two channel chamber, water, at a flow rate of 5 ml/min, had a theoretical Reynolds number of 13.9 in the channels and 39.9 in the bath, both in a laminar flow regime (Brody et al., 1996).

A structure was developed to support the tissue, vertically, in the centre of the flow, allowing perfusion across both surfaces. Oxygen reaches tissue in recording chambers by diffusion (Croning and Haddad, 1998). Perfusion of the tissue across both surfaces increases the possible slice thickness that can be maintained hypoxia

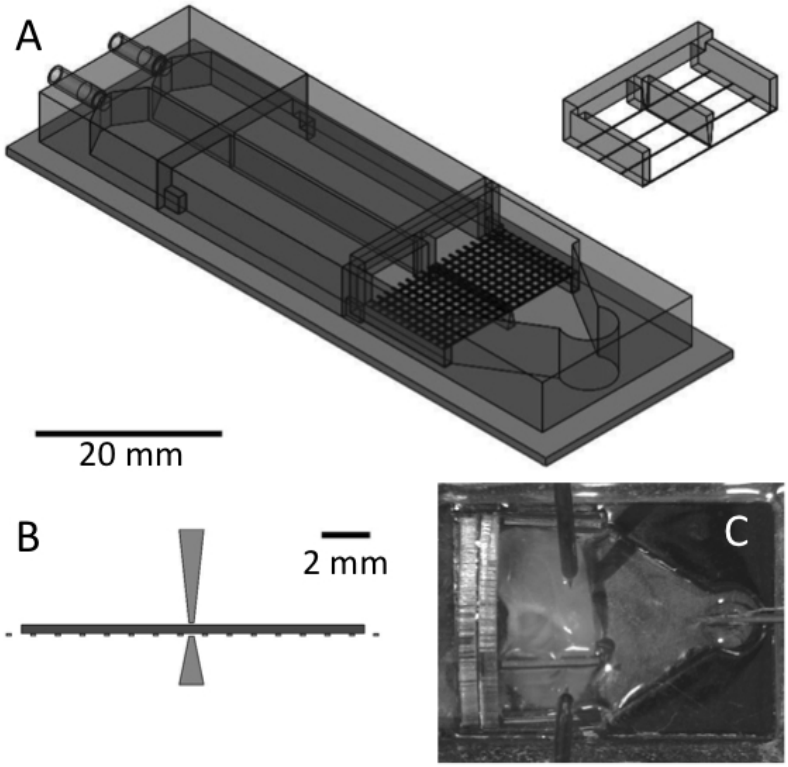

Figure 2.2: (A) A rendered CAD model of the chamber showing the bath region with mesh tissue support and slice hold down with dividers. (B) Cross section showing dividers on tissue support and hold down relative to tissue slice. (C) An image of the bath region of a chamber built to target the entorhinal cortex region of a cortical slice with a different solution to the rest of the cortex and hippocampus. Two microelectrodes (filled with a 2 mM solution of Brilliant blue R, to allow visualisation), a cortical slice, bath earth and hypodermic needle (for outflow) are shown.

free. Thicker slices provide a greater connected network for study. A similar component was designed to hold the tissue in place from above. Both the slice support and slice hold down were designed to fit in an accommodating slot in the bath region of the chamber (Figure 2.2A). The horizontal bars connected the sides above the level of the fluid and, therefore, did not obstruct the flow and thereby introduce turbulence, which would increase mixing. The main structures of the support and hold down were manufactured using MSL. A 10 Denier nylon mesh was stretched across the support and 10 Denier nylon fibres were attached across the hold down.

The insertion of microelectrodes in to the chamber was expected to disrupt the laminar flow and cause mixing of the perfusing solutions. To counteract this effect dividers were included on the slice support and hold down. These aligned with the divide between the channel inlets and thus reduced mixing in the chamber. The dimensions of the dividers were such that they did not come into contact with the tissue. The dividers reduced the perfusing flow to a small area of the tissue directly beneath them, they, however, tapered to 200 μm in width above the tissue surface to minimise this effect (Figure 2.2A and B). The maximum distance of any area of tissue from flowing perfusing medium in a 350 μm slice was 300 μm, diffusion could maintain tissue viability over this distance (Meme et al., 2009).

The bath region had a working area of 16.8 mm x 13.2 mm. This then tapered symmetrically towards a hypodermic needle connected to a pump for out-flow. This avoided the eddy currents that would be expected in corners. Behind this was a region for an earth, allowing contact with the perfusing medium, but not affecting the laminar flow.

The tissue bath was connected to in-flow tubing with 7 mm long sections of 3 mm diameter capillary tubes. These were inserted into collars on the chamber.

Chamber manufacture

The chamber consisted of a number of structures, manufactured by MSL, mounted on a standard microscope slide (75 mm x 25 mm). MSL is an additive layer manufacturing process that employs a photocurable resin to produce solid three dimensional structures. Two dimensional cross sections are sequentially projected into a tray

of liquid resin to cure regions where a solid is required and build up a three dimensional structure. The parts were designed in a computer aided design package (SolidWorks 2011). The parts were then converted into a set of two dimensional cross sections at 25 m intervals using Envisiontec RP. The parts were manufactured on a custom Envisiontec Perfactory Mini SLA system (Envisiontec, Gladbeck, Germany) out of Envisiontec R11 (25 μm voxel depth) resin (Envisiontec, Gladbeck, Germany). After manufacture the parts were washed with acetone and hardened in an Envisiontec Otoflash (Envisiontec, Gladbeck Germany) (1000 flashes on each side; flash frequency: 10 Hz; spectral distribution: 300 - 700 nm; power: 200 W). This caused the polymerisation of any unreacted resin on the surface of the parts. This was hypothesised (and tested, detailed below) to prevent contamination of the perfusing medium with resin from the chamber.

The components were mounted on a microscope slide and 7 mm lengths of glass capillary inserted into the chamber, to form the interface for inflow tubes. These were secured with epoxy adhesive.

The nature of the manufacturing process meant that a chamber bespoke for an experiment could be manufactured rapidly. The build time for each component used here was 1 hour 42 minutes. Figure 2.2C shows the bath region of a chamber produced to target the entorhinal cortex region of a sagittal slice of cortex, used to investigate the origin of electrographic seizure activity. For such chambers the in-flow rate to each region had to be corrected to generate equal flow speeds for the different solutions, to prevent shear stress between the solutions in the chamber.

Chamber operation

Solutions were delivered (at the same flow rate) to the chamber through gas impermeable Tygon tubing by a double headed peristaltic pump (SciQ 400, Watson-Marlow, Cornwall, UK). A system of four valves allowed the solution supplied to each side to be changed without the introduction of air bubbles. Two syringes were connected to T connectors immediately prior to the chamber. These were used to remove air bubbles from the channels in the chamber when initially priming.

Solutions were maintained at 34 ^{o}C in a water bath to prevent de-gassing

when heated prior to entry to the chamber.

To avoid the need for two heating systems (one for each solution), a simple (and inexpensive) method of heating the two solutions was developed. A 125 ml glass beaker (positioned within the faraday cage, close to the bath) containing water was maintained at 40 ^{o}C. This was achieved by pumping (with a diaphragm pump, 0.35 l/min, RS, Northants, UK) water from a bath at 60 ^{o}C, external to the Faraday cage, through a tube coiled in the beaker and back to the bath. The tubes containing the solutions were, at the end immediately prior to the bath, coiled and immersed in the water. To test the temperature stability of the heating system, the temperature in the bath region of the device was measured for periods of one hour (n = 3) at 10 Hz, using a thermocouple connected to a TC-10 temperature controller (npi electronic GmbH, Tamm, Germany) and recorded using a CED Power 1401 mkII digitiser, controlled by Spike2 software (Cambridge Electronic Design, Cambridge, UK). This was compared to the temperature stability of solution in a commercially available bath (RC-27, Warner Instruments, Hamden, CT, USA) heated using a commercially available system. The solution was heated by an HPT-2 heated perfusion tube (ALA Scientific Instruments Inc. Harmingdale, NY, USA) and the temperature was controlled by a TC-10 temperature controller (npi electronic GmbH, Tamm, Germany). The temperature was recorded for the same periods and using the same methods for both systems, with a set temperature of 32 ^{o}C. The mean temperature using the novel system (and the commercial system) was 31.57 ^{o}C (29.46 ^{o}C). The standard deviation was 0.18 ^{o}C (0.12 ^{o}C) and half of the maximum range was 0.47 ^{o}C (0.37 ^{o}C). The system we implemented was, therefore, deemed acceptable for use.

A tissue slice was transferred on to the mesh support and the slice hold down positioned on top to hold it in place (Figure 2.2A). Slices were positioned relative to the divide between in-flow channels as necessary for each experiment.

For the out-flow, a hypodermic needle was held with its tip at the desired level of the bath. This was connected, through a second peristaltic pump (323, Watson-Marlow, Cornwall, UK), to a waste container.

Solution mixing

The effectiveness of the chamber in minimising the mixing of two solutions was characterised using a fluorescent dye. The chamber was supplied with a 50 μM solution of fluorescein sodium salt (Sigma-Aldrich, Dorset, UK) in de-ionised water on one side and de-ionised water on the other. The chamber was uniformly illuminated with eight LEDs with peak emission at 458 nm (PLCC-4, RS, Northants, UK) in an otherwise dark environment. An image of the chamber was captured with a VMS-004D microscope (Veho, Hampshire, UK). Images were corrected for intensity using a control region outside the chamber. The fluorescence profiles at cross sections 1 mm, 6 mm and 12 mm into the chamber, along the direction of flow, were measured. Fluorescence was converted to concentration and the interface width was measured, defined to be the distance over which the fluorescein concentration changed from 25% to 75% of its maximum.

The effectiveness of the channels in suppressing inertial instability and therefore mixing was investigated. Four chambers were compared. These were manufactured with inflow channels of lengths uniformly spanning the possible range, giving channel lengths of 0 mm, 12.4 mm, 24.8 mm and 37.2 mm.

The effect on the width of the interface of the addition of microelectrodes and supporting net to the bath region was investigated for a chamber with full length (37.2 mm) channels. The effect of the addition of net with divider, in addition to microelectrodes, tissue and supporting net to chambers with no inflow channels (0 mm) and full length inflow channels (37.2 mm) was also compared.

Fluorescence profiles were measured six times for each chamber and addition. The channel supplied with fluorescent solution was alternated and interleaved with controls during which both channels were supplied with the same solution.

Solution exchange

The time for solution exchange in the chamber was measured using a fluorescent dye. The bath was illuminated and imaged as for experiments to measure mixing. The chamber was supplied on both sides with de-ionised water. This was then changed to a 50 μM solution of fluorescein sodium salt (Sigma-Aldrich, Dorset, UK)

in de-ionised water. The fluorescence intensity was converted to concentration and the time taken for the concentration of fluorescent solution to change from 5% to 95% of its maximum was measured. The solution exchange time was measured for a chamber with 4 mm high channels and a chamber with 2 mm high channels. For comparison the exchange time in a commercial bath (RC-27, Warner Instruments, Hamden, CT, USA) with solution depths of both 2 mm and 4 mm was also measured using the same method. In all cases measurements were made (n = 3) both with the chambers empty and when containing a tissue slice, and microelectrodes.

Contamination detection

Water was collected after passing though the system and tested for contamination from the chamber. De-ionised water was passed though the chamber at 5 ml/min, 31−32 ^{o}C (as required of solutions for biological experiments) and collected. For comparison, de-ionised water was passed though the tubing of the system, with the chamber replaced with a Petri dish, and collected. A mixture of less than 100 parts per million (ppm), by volume, R11 resin monomer, cross-linker and associated solvents, in de-ionised water, was also prepared. 100 μl of R11 resin monomer, cross-linker and associated solvents was mixed with 10 ml of de-ionised water for 30 minutes in a glass bottle on an orbital shaker. R11 resin is orange (because of the addition of photoinhibitors to aid layer thickness control) the majority was seen to settle to the bottom of the bottle. 100 μl of the aqueous phase, that relevant to contamination of water based solutions, was removed and mixed with 10 ml of de-ionised water. This resulted in a solution of the water soluble components of R11 of much less than 100 ppm. For each solution, a 2 ml aliquot was transferred to a 10 ml sample bottle with a crimp lid, fitted with a septum. The samples were heated to 80 ^{o}C and exposed to a solid phase micro extraction (SPME) fibre (Supelco, Sigma Aldrich, Dorset, UK) for 15 minutes. The SPME fibre was then inserted into a Scion SQ 451 gas chromatography - mass spectrometry (GCMS) system (Bruker, Bremen, Germany) and heated to 250 ^{o}C. The GCMS column oven was heated from 50 ^{o}C to 280 ^{o}C over 15 minutes. Mass spectra were recorded at 20 Hz over a mass range of 35 - 400 u.

Biological testing

Slice preparation

Parasagittal slices of cerebellar vermis or cortex (350 μm) were prepared from male Wistar rats at postnatal days 18-21. In accordance with the UK Animals (Scientific Procedures) Act 1986, rats were killed by cervical dislocation and decapitated. Either the cerebellum or cerebrum was rapidly removed. Parasagittal slices were cut on a Microm HM 650V microslicer (Carl Zeiss, Welwyn Garden City, UK) in cold (2−4 ^{o}C) high Mg^{2+}, low Ca^{2+} artificial cerebrospinal fluid (aCSF), composed of (mM): 127 NaCl, 1.9 KCl, 8 $MgCl_2$, 0.5 $CaCl_2$, 1.2 KH_2PO_4, 26 $NaHCO_3$, 10 D-glucose (pH 7.4 when bubbled with 95% O_2 and 5% CO_2). Slices were stored in experimental aCSF (1.0 mM $MgCl_2$, 2.0 mM $CaCl_2$), bubbled with 95% O_2 and 5% CO_2. The slices were maintained in a Gibbs chamber at 34 ^{o}C for the first hour after slicing and at room temperature for the remaining time before recording.

Electrophysiology

Individual tissue slices were transferred to the bath region of the chamber, maintained at 31−32 ^{o}C, and continuously perfused at 5 ml/min with aCSF bubbled with 95% O_2 and 5% CO_2. Extracellular recordings were made with aCSF filled electrodes, tip diameters 15 μm, placed on the surface of the tissue. The recordings were made using WPI ISO-DAM amplifiers (WPI, Hertfordshire, UK), with band pass filters: 10 Hz - 3 kHz and digitised on-line (10kHz) with a CED Power 1401 mkII digitiser, controlled by Spike2 software (Cambridge Electronic Design, Cambridge, UK). Slices were maintained in the chamber for twenty minutes prior to the start of recording.

Schaffer collateral stimulation

Schaffer collaterals were stimulated with a 50 μm diameter concentric bipolar stimulating electrode (FHC, Bowdoin, ME, USA) from a Model 2100 isolated stimulator (AM Systems, Sequim, WA, USA). The resulting field excitatory post synaptic potentials (fEPSPs) in CA1 were recorded to test slice viability in the chamber. Slices were maintained in the novel chamber for 3.5 hours prior to stimulation. A paired

pulse protocol was implemented with a 50 ms interval between pulses, stimulating with 5V for periods of 200 μs. The initial slope of the fEPSPs was measured and the paired pulse ratio calculated. The evoked fEPSPs were compared with those from slices that were maintained in a Gibbs chamber for 3 hours and then transferred to the chamber for a 30 minute recovery period prior to stimulation. Slices that had been maintained in the two environments were interleaved. The initial slopes and the paired pulse facilitation ratios of the evoked fEPSPs were compared to published results from other work (Sui et al., 2005; Manahan-Vaughan and Schwegler, 2011).

Cerebellar recording

Purkinje cells exhibit spontaneous action potentials, at a frequency of approximately 50 Hz, in the absence of synaptic input (Raman and Bean, 1999) and thus are active in *in vitro* cerebellar slices. This spontaneous activity was used as a functional measure of the effectiveness of the bath. Microelectrodes were placed on the surface of the Purkinje cell layer, one on each side of the chamber, such that spontaneous firing of Purkinje cells was recorded. Initially both sides of the bath were perfused with aCSF (5 minutes). Following this, one side of the bath was perfused with the sodium channel blocker, tetrodotoxin (TTX, 1 μM, Ascent, Cambridge, UK) to terminate the spontaneous firing on that side of the bath. The other side was still perfused with aCSF. If the chamber functioned successfully, the spontaneous firing would be terminated on the side perfused with TTX but continue on the other side. After a further 5 minutes, 1 μM TTX was applied to both sides of the bath to confirm that firing on both sides could be abolished. In total nine experiments were performed, the side of the chamber to which TTX was first applied was alternated. For three of the experiments the distance between the recording microelectrode on the side opposite to that initially supplied with TTX and the divide was minimised. This biologically tested the effectiveness of the solution separation. In all three cases the microelectrode was less than 2 mm from the divide and in one case less than 1.5 mm from the divide.

Epileptiform activity recording

Epileptiform activity was elicited in slices of cortex by perfusion with an excitant solution (experimental aCSF with 0 mM Mg^{2+}, 5 mM K^{+}, (Mody et al., 1987)). Slices were positioned such that approximately half of the cortex was on each side of the divide. The hippocampus did not cross the central divide of the bath. Microelectrodes were placed, one on each side of the bath, over layer five of the cortex. After transfer to the bath and placement of the microelectrodes the slices were left to recover for twenty minutes before recording. Initially both sides of the bath were perfused with aCSF for 5 minutes. Following this, one side of the bath was perfused with excitant solution, and the other with aCSF, for 30 minutes. If the chamber was functioning successfully it was expected that this would elicit epileptiform activity on the side of the tissue exposed to excitant but not on the other side (perfused with aCSF). Subsequently both sides of the bath were perfused with aCSF for 30 minutes to terminate any seizure activity. Both sides of the tissue were then perfused with excitant solution for 30 minutes. This was expected to elicit epileptiform activity on both sides of the tissue and thus confirm that they were viable and that the microelectrodes were correctly placed. Synchronicity of activity on both sides of the divide during this final period would demonstrate the viability of the region of the tissue under the divider.

2.4 Results

Solution mixing

The effectiveness of the inflow channels in reducing turbulence and mixing in the chamber was tested (as detailed above). The images of the bath region of the chamber with 0 mm channels (Figure 2.3A) showed significant mixing arising from inertial instability. In contrast, images of the bath region of the chamber with 37.2 mm channels showed a straight, narrow, interface (Figure 2.3C). Profiles of cross sections of the bath regions of the two chambers (Figures 2.3B and 2.3D respectively) show a poorly defined interface in the case of the chamber with 0 mm channels and a well defined, consistently positioned, interface in the case of the

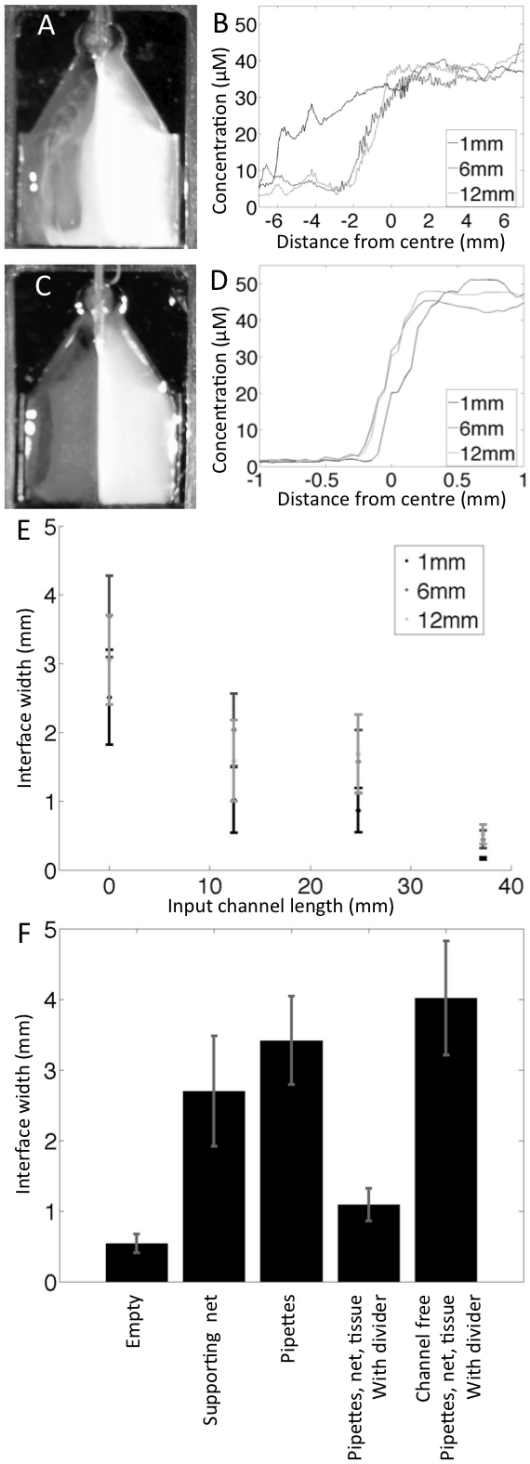

Figure 2.3: Dye characterisation of solution interface width. (A) Image of bath region of chamber with 0 mm channels supplied with a fluorescent solution to left and water to the right. Significant mixing can be seen arising from inertial instability. (B) Concentration profile at cross sections 1 mm, 6 mm and 12 mm along flow direction into empty bath region of chamber with 0 mm channels as shown in (A). (C) Image of bath region of chamber with 37.2 mm channels supplied with a fluorescent solution to left and water to the right. The separation of the distinct solutions is seen to be well maintained. (D) Concentration profile at cross sections 1 mm, 6 mm and 12 mm along flow direction into empty bath region of chamber with 37.2 mm channels as shown in (C). (E) Dependence of interface width on input channel length. Measured along cross sections 1 mm, 6 mm and 12 mm along flow direction into chamber region. Mean of n = 6, bars show the standard error. (F) Width of interface 12 mm along flow direction in chamber with 37.2 mm or 0 mm channels, with listed additions. Mean of n = 6, bars show the standard error.

chamber with 37.2 mm channels (the maximum length possible given the other design constraints). A greater than 90% change in concentration occurred over less than 0.5 mm in the bath region of the full device. The interface width decreased with increasing channel length, as did the variation in interface width (Figure 2.3E). The interface width (25% to 75% change in concentration) was 3.7 ± 0.6 mm in the centre of the bath region of the chamber with 0 mm channels and 0.4 ± 0.1 mm in the chamber with 37.2 mm channels (n = 6 for both). The visible effects of inertial instability in the chamber with 0 mm channels, its apparent absence in the chamber with 37.2 mm channels, and the decrease in interface width with channel length all support the conclusion that the high surface area to volume ratio inflow channels acted to suppress inertial instability and, therefore, mixing.

The effect on the interface width of the introduction of microelectrodes and a supporting net to the chamber was measured. The presence of the microelectrodes or net in the images limited analysis to the profile at the cross section at 12 mm. As expected, the addition of both microelectrodes and a supporting net caused an increase in interface width, to 2.7 ± 0.8 mm and 3.4 ± 0.6 mm respectively (n = 6 for both) (Figure 2.3F). The replacement of the supporting net and hold down with ones with a divider effectively compensated for this effect. The interface width 12 mm into the bath region of a chamber with 37.2 mm channels, containing a support and hold down with dividers, a tissue slice and two microelectrodes, was 1.1 ± 0.2 mm. The dividers were, however, insufficient to prevent mixing independent of inflow channels. The interface width in a chamber with 0 mm channels, containing a support and hold down with dividers, a tissue slice and two microelectrodes was 4 ± 0.8 mm.

Solution exchange

After the change in solution supplied to the chamber, the fluorescence intensity increased uniformly across the bath region of the chamber (Figure 2.4A). In contrast, there was mixing in the commercially available bath that resulted in stagnant regions, free from fluorescent solution, more than 20 s after the fluorescent solution reached the in-flow of the bath (Figure 2.4A). The increase in concentration of

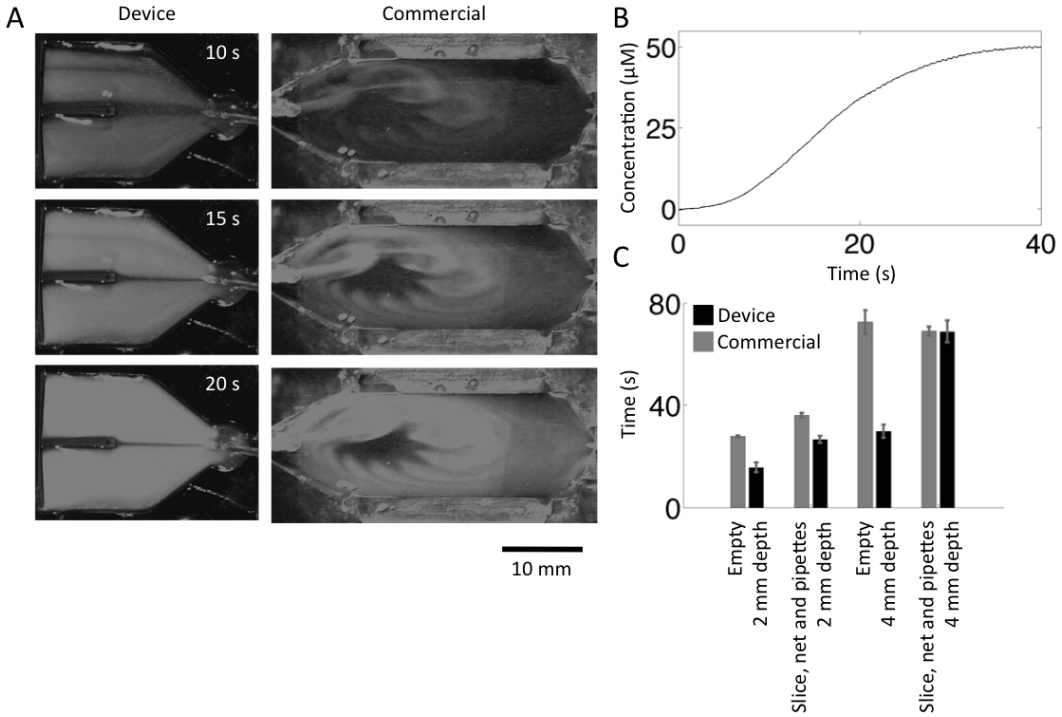

Figure 2.4: Dye characterisation of solution change. (A) Sequence of images during the change from water to a fluorescent solution taken at the indicated times. On the left are images of the bath region of the novel chamber, showing a uniform increase in fluorescence intensity, free from turbulence. On the right are images of a commercial tissue bath (detailed in the text) showing mixing of the two solutions with a stagnant region of water persisting, unmixed with fluorescent solution. (B) Concentration profile during change from water to fluorescent dye for the region occupied by a tissue slice in the novel chamber. (C) Comparison of times for change from 5% to 95% of the maximum fluorescein concentration for both the novel chamber and the commercially available bath. The contents of the bath and the depth of solution is indicated for each case. Mean of n = 3, bars show the standard error.

fluorescent solution in the bath region of the chamber increased sigmoidally (Figure 2.4B) with a characteristic time scale less than or equal to that of the commercial bath under the same conditions (Figure 2.4C). There was mixing of the two solutions in both the novel chamber and the commercially available bath. In the novel chamber, however, the mixing occurred in the in-flow channels, prior to the bath region. In both the novel chamber and the commercial bath the exchange time was significantly longer with a solution depth of 4 mm than with a solution depth of 2 mm. When containing a tissue slice and two microelectrodes the time for exchange with 4 mm deep solution for the novel chamber (and the commercial bath) was 68.9 $\pm$ 7.5 s (69.0 $\pm$ 2.9 s) and with a solution depth of 2 mm 26.6 $\pm$ 2.3 s (36.0 $\pm$ 1.5 s).

Whilst mixing did occur between solutions supplied consecutively to the same side of the chamber, the time for exchange from 5% to 95% concentration was no worse than that for a commercially available bath. Mixing was isolated to the in-flow channels prior to the region containing the tissue slice. This reduced areas of stagnant solution in contact with the slice.

Contamination detection

There were no differences, above measurement noise, between the GCMS results from the solution that had passed through the chamber and the control solution that only passed through the associated tubing (Figure 2.5A). The solution of R11 resin monomer, cross-linker and associated solvents ($\ll$ 100 ppm by volume) resulted in GC peaks consistently over 50 times greater than the measurement noise. The upper limit on contamination was, therefore, 2 parts per million by volume. Given the concentration of the R11 solution was an upper bound, the actual level of contamination was, however, much less than this. MSL, using R11 resin, provides a rapid technique for the productions of chambers bespoke for experiments. The resulting parts have been shown not to contaminate water based solutions, at physiological temperatures, that pass through them. MSL using R11 resin could, therefore, be an effective manufacturing technique for many types of chamber with biological applications.

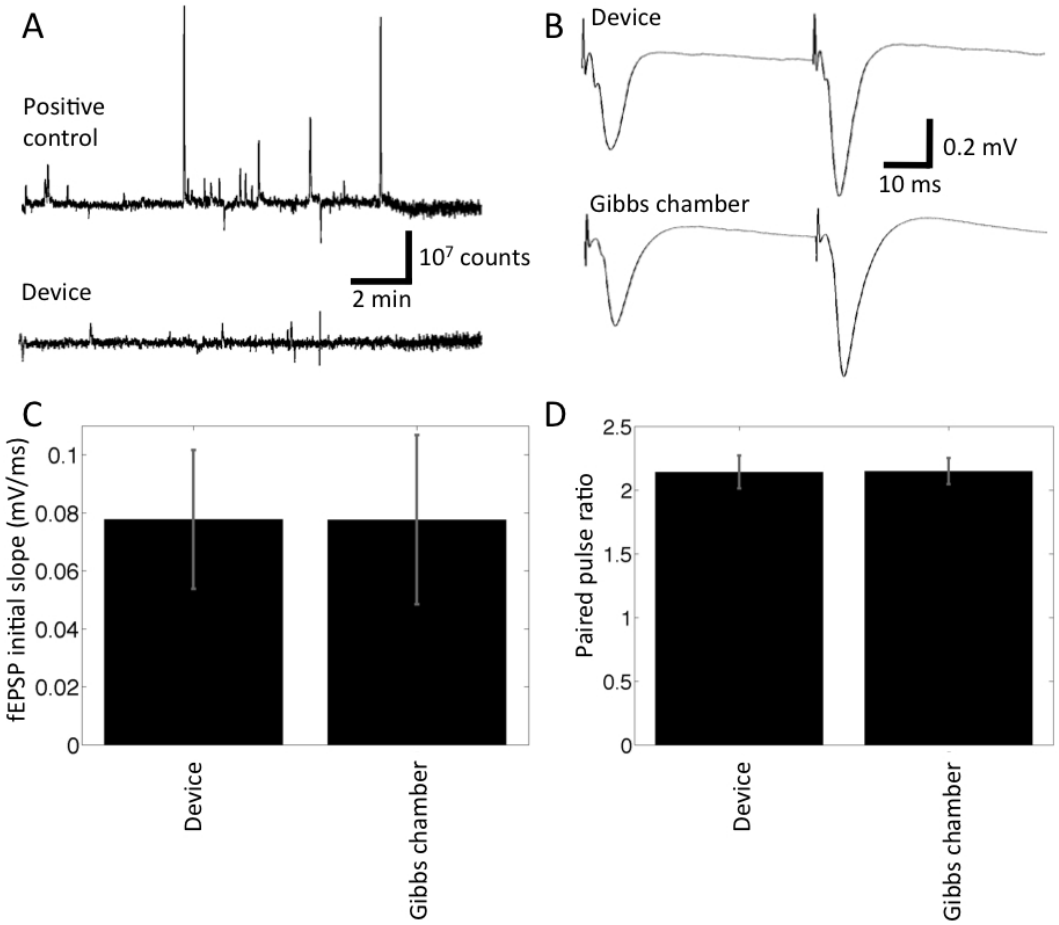

Figure 2.5: Results of tests for contamination of slices in the chamber from components of the R11 resin used for its manufacture. (A) Top: Result of gas chromatography of a control solution of less than 100 ppm of the water soluble components of R11 resin monomer, cross-linker and associated solvents. Bottom: Result of gas chromatography of water after being passed through the chamber at 30 - 31 ^{o}C, showing no detectable contamination with any components of R11 resin. (B) Example recordings from hippocampal slices using a paired pulse stimulation protocol (50 ms interval) illustrating the viability of slices after an extended period in the novel chamber. Top: Example fEPSPs from a slice maintained in the novel chamber for 3.5 hours. Bottom: Example fEPSPs from a slice maintained in a Gibbs chamber for 3 hours before being transferred to the novel chamber for a 30 minute recovery period before stimulation. (C) Comparison of the initial slope of the first fEPSP evoked in slices maintained in the novel chamber and in a Gibbs chamber, showing no significant difference. Mean of n = 6, bars show the standard error. (D) Comparison of the paired pulse facilitation ratio from the initial slope of the fEPSPs evoked in slices maintained in the novel chamber and in a Gibbs chamber, showing no significant difference. Mean of n = 6, bars show the standard error. Recordings were made from interleaved slices either maintained in the bath or in a Gibbs chamber and fEPSPs were evoked with the same stimulus strength.

Schaffer collateral stimulation

The fEPSPs evoked in hippocampal slices maintained in the novel chamber were indistinguishable from those evoked in slices maintained in a Gibbs chamber (Figure 2.5B and 2.5C). The mean initial slope of the first fEPSP evoked in slices maintained in the novel chamber (and the Gibbs chamber) was -0.078 $\pm$ 0.012 mV/ms (-0.078 $\pm$ 0.014 mV/ms) and the paired pulse facilitation ratio (for a 50 ms interval) was 2.14 $\pm$ 0.13 (2.15 $\pm$ 0.10). These results are consistent with published results from other work (Sui et al. 2005; Manahan-Vaughan and Schwegler 2011). Slices maintained in the chamber for over 3.5 hours exhibited stimulus evoked responses indistinguishable from those evoked in slices maintained in standard chambers. There was, therefore, no evidence of any adverse effects either from contamination of the perfusing solution with components of the R11 resin (consistent with the results from tests with GCMS) or from a difference in perfusion.

Cerebellum recording

The effectiveness of the chamber was tested using extracellular recordings from Purkinje cells. All slices (n = 9) exhibited spontaneous activity, demonstrating slice viability in the chamber. In all cases application of 1 μM TTX to one side terminated the activity on that side (n > 3 for each side of the chamber) but had no effect on the opposite side, including those cases (n = 3) when the microelectrode on the side opposite to that initially perfused with TTX was less than 2 mm from the divide. The ongoing activity was shown to be sensitive to TTX with subsequent application to that side (Figure 2.6). This demonstrated the effectiveness of the chamber in maintaining the solution separation under typical recording conditions with a slice present in the chamber.

Recording of epileptiform activity

The effectiveness of the chamber was further tested by eliciting epileptiform activity in slices of cortex. Extracellular recordings (n = 12) were made while implementing the perfusion protocol described above. This protocol was implemented with the side initially exposed to excitant being either the anatomically anterior region (n = 6)

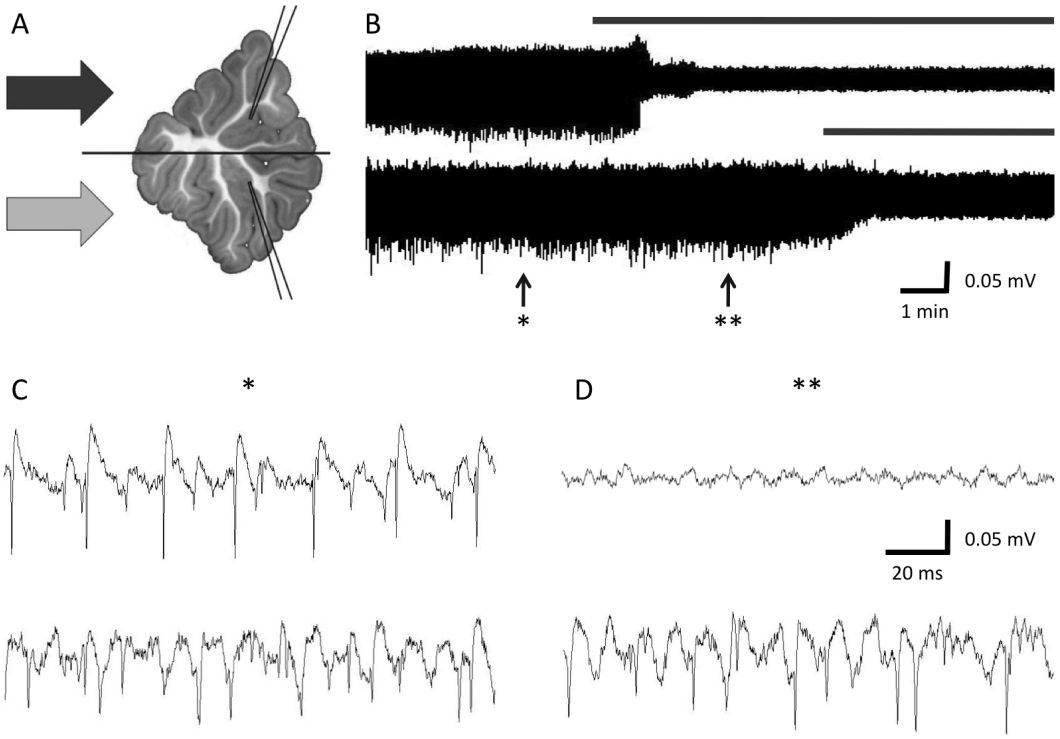

Figure 2.6: Example of an individual cerebellar slice recording demonstrating the effectiveness of the chamber. (A) Schematic of cerebellar slice showing microelectrode placement relative to the interface. Arrows indicate perfusion with distinct solutions. (B) Extracellular recordings of spontaneous Purkinje cell action potential firing on a compressed time base. Microelectrode placement as in (A). Application of 1 μM TTX (grey bars) at five minutes causes cessation of firing on perfused side while not affecting the opposite side. Application of TTX to both sides caused a complete loss of activity. (C) Expanded portion of panel (B) from (*) illustrating multi-unit firing on both sides of the tissue. (D) Expanded portion of panel (B) from (**) illustrating continued multi-unit firing on one side although activity has been blocked on the other side of the tissue.

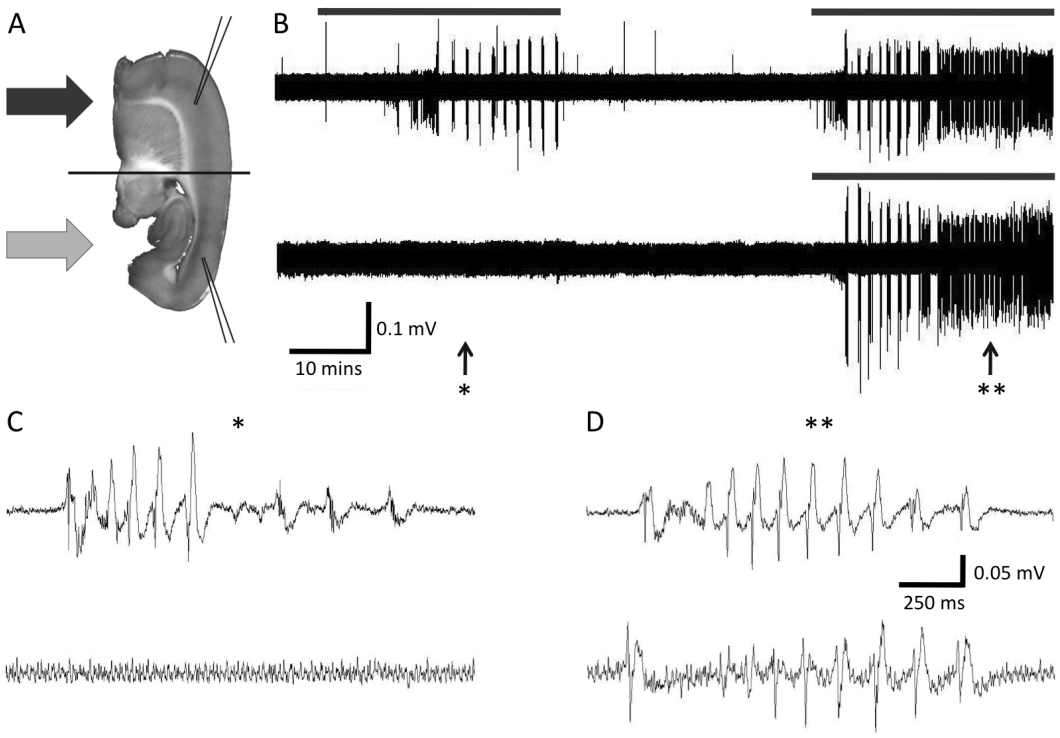

Figure 2.7: Example recording of induced epileptiform activity, demonstrating the effectiveness of the chamber both with respect to targeted perfusion and the maintenance of tissue viability. (A) Schematic of cortical slice showing microelectrode placement relative to the interface. Arrows indicate perfusion with distinct solutions. (B) Extracellular voltage recording on a compressed time base. Microelectrode placement as in (A). Application of excitant solution is indicated by grey bars. Initially excitant was applied to one side, which became active, while the other side remained quiescent. Application of excitant to both sides induced activity on both sides. (C) Expanded portion of panel (B) from (*) showing a burst of epileptiform activity on one side of the slice while the other side remained quiescent. (D) Expanded portion of panel (B) from (**) showing a burst of population spikes on both sides of the tissue. The synchronicity of the burst, and the population spikes with in it, demonstrates the viability of the centre of the tissue between the dividers, which connects them.

or the anatomically posterior region (n = 6). In all cases epileptiform activity was recorded on the side perfused with excitant but not on the side perfused with experimental aCSF. Activity was recorded on both sides when both were perfused with excitant (Figure 2.7). This demonstrated the effectiveness of the chamber in generating isolated activity in a tissue slice. As both anatomical regions were recorded as the first side perfused with excitant in isolation, the activity was not a result of the side exposed being more excitable. The slices were alternated in orientation such that half of each set of six recordings was made with excitant first perfusing on each side of the chamber. This eliminated the possibility of an asymmetry in the perfusion. In all cases the epileptiform activity recorded when

both sides were perfused with excitant was synchronised. Bursts of seizure activity, and the population spikes within them, were temporally correlated (Figure 2.7C). This demonstrated the viability of the tissue between the central dividers. This was required for transmission and, therefore, correlation between the activity in the two regions of tissue. Synchronisation was exhibited at the end of 95 minutes of recording. Including the time for microelectrode placement and that allowed for slice recovery, this demonstrated the chamber maintained the viability of entire slices for periods in excess of two hours.

This form of protocol has application in the study of seizure propagation from pathological to physiological regions of tissue. This is exhibited in secondary generalisation of seizure activity *in vivo* and is of significant research interest.

2.5 Discussion

A chamber has been produced that allows extended regions of a tissue slice *in vitro* to be exposed, in isolation, to changes in conditions or drugs. The device facilitates the study of the propagation of epileptiform activity between regions of tissue in different ionic environments. The chamber could also be used to carry out experiments with a simultaneous control in coronal slices, with each side of a slice being maintained in different conditions. This would reduce bias as the regions being compared would be from the same position in the brain and when being tested would have been maintained for the same amount of time since dissection.

The effectiveness of the chamber has been shown to be preserved with the introduction of microelectrodes to the chamber, to record from the slice. This simultaneous solution targeting and access for microelectrodes has not previously been achieved. The chamber was manufactured from R11 resin using MSL. This is an additive manufacturing technique allowing chambers bespoke for experiments to be produced rapidly. It has been shown that chambers manufactured from R11 using MSL do not contaminate water based solutions that pass through them at physiological temperatures. The chamber has been shown to maintain the viability of tissue slices for periods in excess of 3.5 hours, perfusing them across all surfaces and maintaining them at a physiological temperature. The design employed generalises

to varied geometries bespoke for experiments. In future work chambers with greater numbers of channels will be developed.

2.6 Acknowledgements

We thank Simon Leigh and Christopher Purssell for useful discussions and Eric Westenbrink for assistance with GCMS.

2.7 Grants

This work was funded by the Engineering and Physical Sciences Research Council through the MOAC Doctoral Training Centre.

2.8 Disclosures

No conflicts of interest, financial or otherwise, are declared by the authors.

Bibliography

Ahrar, S., Nguyen, T., Shi, Y., Ikrar, T., Xu, X., and Hui, E. Optical stimulation and imaging of functional brain circuitry in a segmented laminar flow chamber. *Lab on a chip*, 13:536–541, 2013.

Blake, A., Pearce, T., Rao, N., Johnson, S., and Williams, J. Multilayer PDMS microfluidic chamber for controlling brain slice microenvironment. *Lab on a chip*, 7:842–849, 2007.

Brody, J., Yager, P., Goldstein, R., and Austin, R. Biotechnology at low Reynolds numbers. *Biophysical Journal*, 71:3430–3441, 1996.

Choi, Y., McClain, M., LaPlaca, M., Frazier, A., and Allen, M. Three dimensional MEMS microfluidic perfusion system for thick brain slice cultures. *Biomedical Microdevices*, 9:7–13, 2007.

Croning, M. and Haddad, G. Comparison of brain slice chamber designs for investigations of oxygen deprivation *in vitro*. *Journal of Neuroscience Methods*, 81: 103–111, 1998.

Hill, M. and Greenfield, S. The membrane chamber: A new type of *in vitro* recording chamber. *Journal of Neuroscience Methods*, 195:15–23, 2011.

Huang, Y., Williams, J., and Johnson, S. Brain slice on a chip: opportunities and challenges of applying microfluidic technology to intact tissues. *Lab on a chip*, 12: 2103–2117, 2012.

Jefferys, J. and Haas, H. Synchronised bursting of CA1 hippocampal pyramidal cells in the absence of synaptic transmission. *Nature*, 300:448–450, 1982.

Konnerth, A., Heinemann, U., and Yaari, Y. Slow transmission of neural activity in hippocampal area CA1 in absence of active chemical synapses. *Nature*, 207: 69–71, 1984.

Manahan-Vaughan, D. and Schwegler, H. Strain-dependent variations in spatial learning and in hippocampal synaptic plasticity in the dentate gyrus of freely behaving rats. *Frontiers in Behavioral Neuroscience*, 5:1–7, 2011.

Meme, W., Vandecasteele, M., Giaume, C., and Venance, L. Electrical coupling between hippocampal astrocytes in rat brain slices. *Neuroscience Research*, 63: 236–243, 2009.

Mody, I., Lambert, J., and Heinemann, U. Low extracellular magnesium induces epileptiform activity and spreading depression in rat hippocampal slices. *Journal of Neurophysiology*, 57:869–888, 1987.

Mohammed, J., Caicedo, H., Fall, C., and Eppington, D. Microfluidic add-on for standard electrophysiology chambers. *Lab on a chip*, 8:1048–1055, 2008.

Queval, A., Ghattamaneni, N., Perrault, C., Gill, R., Mirzaei, M., McKinney, R., and Juncker, D. Chamber and microfluidic probe for microperfusion of organotypic brain slices. *Lab in a chip*, 10:326–334, 2010.

Raman, I. and Bean, B. Ionic currents underlying spontaneous action potentials in isolated cerebellar purkinje neurons. *The Journal of Neuroscience*, 19:1663–1674, 1999.

Rutecki, P., Lebeda, F., and Johnston, D. Epileptiform activity induced by changes in extracellular potassium in hippocampus. *Journal of Neurophysiology*, 54:1363–1375, 1985.

Salierno, M., Cabrera, R., Filevich, O., and Etchenique, R. Encapsulated Petri dish system for single-cell drug delivery and long-term time lapse microscopy. *Analytical Biochemistry*, 371:208–214, 2007.

Scott, A., Weir, K., Easton, C., Huynh, W., Moody, W., and Folch, A. A microflu-

idic microelectrode array for simultaneous electrophysiology, chemical stimulation, and imaging of brain slices. *Lab on a chip*, 13:527–535, 2013.

Smith, T. and Cunningham, M. Pressure ejection system for quantitative focal application of neuroactive substances from micropipettes. *Medical and biological engineering and computing*, 21:138–144, 1983.

Sui, L., Anderson, W., and Gilbert, M. Impairment in short-term but enhanced long-term synaptic potentiation and ERK activation in adult hippocampal area CA1 following developmental thyroid hormone insufficiency. *Toxicological sciences*, 85: 647–656, 2005.

Tang, Y., Kim, J., Lopez-Valdes, H., Brennan, K., and Ju, Y. Development and characterisation of a microfluidic chamber incorporating fluid ports with active suction for localized chemical stimulation of brain slices. *Lab on a chip*, 11:2247–2254, 2011.

Chapter 3

High-resolution recording of neural activity by transforming Intrinsic Optical Signals

The intrinsic optical properties of brain tissue are known to be activity dependent. Measurement of these intrinsic optical signals (IOSs) is commonly used as a non-invasive method to infer neuronal activity. Their use as a proxy for neuronal activity has many advantages; they require no mechanical, chemical or genetic interference with the tissue and are not limited by recording rate or duration. The temporal dynamics of the IOS are, however, slow and so do not directly correspond to the underlying network dynamics.

We characterised the intrinsic optical signal (IOS) that persists *in vitro* and derived a transformation that converts the slow temporal dynamics of the IOS to a form that accurately reflects the underlying network dynamics, thereby mitigating the primary disadvantage of the use of IOSs as a method to record neuronal dynamics, allowing their advantages to be fully exploited. This chapter contains the submitted paper describing this work. The results of some preliminary experiments characterising the *in vitro* IOS were included in a submission for an MSc, however, none of the data, analysis or text presented here was included in the submission. I

planned and carried out the experiments, carried out the data analysis and wrote the paper under the supervision of Dr James Covington, Dr Magnus Richardson, Prof. Matthew Turner and Dr Mark Wall.

The full paper has been redacted from this version to avoid copyright infringement.

Chapter 4

Characterisation of the spatio-temporal dynamics of the extracellular concentration of adenosine in the neocortex in response to electrographic seizure activity

Adenosine is a potent neuromodulator known to be released in response to seizure activity. The temporal dynamics of this release have previously been investigated, however, the spatial dynamics have not been readily accessible because of the lack of a suitable recording tool for the associated network activity. The transformation presented in Chapter 3 has now rendered this regime accessible. This chapter contains a paper in preparation describing work characterising the spatio-temporal dynamics of adenosine release in response to seizure activity. I planned and carried out the experiments, carried out the data analysis and wrote the paper under the supervision of Dr Magnus Richardson and Dr Mark Wall.

Characterisation of the spatio-temporal dynamics of the extracellular concentration of adenosine in the neocortex in response to electrographic seizure activity

4.1 Abstract

Adenosine is a potent neuromodulator, providing important negative feedback in response to cortical network activity. Adenosine is critical for seizure termination and has significant potential in the treatment of epilepsy. The spatio-temporal dynamics of endogenous adenosine peri-ictally are, however, not well characterised. A number of real-time measurement techniques sensitive to adenosine are available, however, they all have significant cross-sensitivities to other compounds that exhibit transient variation in response to seizure activity. Here, we simultaneously employ two independent techniques to measure extracellular adenosine, along with optical recording of seizure activity and a modelling approach, to elucidate these dynamics and their underlying mechanisms.

Key words: adenosine, electrographic seizure activity, biosensor, fast scan cyclic voltammetry, intrinsic optical signal

4.2 Introduction

Adenosine plays an important role in many physiological processes, such as locomotion and sleep, and can be neuroprotective during pathological events, such as hypoxia and ischaemia (Barraco et al., 1993; Florio et al., 1997; Nagel et al., 2003; Ralevic and Burnstock, 1998; Fredholm et al., 2001; Latini and Pedata, 2001).

A basal tone of adenosine is present in brain tissue (Fredholm et al., 2001; Latini and Pedata, 2001; Kerr et al., 2013) which is augmented by release in response to neuronal activity, metabolic stress and other insults(Ralevic and Burnstock, 1998; Fredholm et al., 2001; Latini and Pedata, 2001). The origins of extracellular adenosine are not completely understood, but could include breakdown of previously re-

leased ATP and direct release through equilibritive transport (Latini and Pedata, 2001; Wall and Dale, 2008). Adenosine can activate four types of G-protein coupled receptors: A_1, A_{2A}, A_{2B}, and A_3 (Fredholm et al., 2001; Ralevic and Burnstock, 1998). Activation of A_1 and A_3 receptors has a mostly inhibitory effect while that of A_2 receptors is largely excitatory. Adenosine is removed to AMP by adenosine kinase (ADK) and to inosine by adenosine deaminase (ADA) (Latini and Pedata, 2001).

Adenosine plays a particularly important role in epilepsy, providing negative feedback in response to seizure activity and it is strongly implicated in seizure termination (During and Spencer, 1992; Ilie et al., 2012; Van Gompel et al., 2014). Changes in adenosine metabolism may also be involved in epileptogenesis (Fedele et al., 2005; Boison, 2006, 2007) and the mechanism of action of the ketogenic diet (Masino et al., 2011). The inhibitory and neuroprotective effects of adenosine make it a promising candidate for therapeutic use (Huber et al., 2001; Boison, 2006), however, the spatio-temporal dynamics of endogenous adenosine release in response to seizure activity remains poorly characterised.

A number of studies of adenosine release in response to seizure activity have been carried out (for example see (Winn et al., 1980; During and Spencer, 1992; Etherington et al., 2009; Van Gompel et al., 2014; Wall and Richardson, 2015)). These studies have, however, yielded inconsistent results, Van Gompel *et al.* (Van Gompel et al., 2014) found adenosine release to be associated with seizure termination, with the peak in extracellular adenosine release occurring up to 26.8 ± 16.5 s after seizure termination. Wall and Richardson (Wall and Richardson, 2015), however, found that extracellular adenosine could not be directly detected as it was metabolised to inosine so rapidly. These studies have, however, been limited in two ways. Firstly in their spatial resolution, microelectrodes can be used to provide high temporal resolution measurement of analyte concentration, the spatial localisation of the associated seizure activity has, however, been limited. Secondly, the methods of detection have not been specific to adenosine, actually measuring, for example, the sum of adenosine, inosine and hypoxanthine. To elucidate the negative feedback suppressing seizure activity it is important to measure adenosine specifically as the

other compounds do not significantly activate A_1 receptors.

A number of methods have been used to measure local extracellular adenosine concentration. It can be inferred from its effect on synaptic transmission (for example see (Fredholm et al., 1984; Yoon and Rothman, 1991; Kerr et al., 2013). However, peri-ictally there are at least two sources of synaptic depression, that caused by transient adenosine release and that resulting from vesicular depletion. Pharmacological approaches could be used to separate the two, but this would be slow compared to the temporal dynamics of the two processes. It is, therefore, not practical to use this approach to infer adenosine dynamics periictally. Microdialysis (During and Spencer, 1992) can be used to measure adenosine concentration, however, its spatial and temporal resolution are both poor. Freeze blow techniques have also been used to measure adenosine concentration (Winn et al., 1980), however, this only allows measurement at a single time point and does not distinguish between intra and extra-cellular adenosine. Two further, microelectrode based, techniques can provide higher spatio-temporal resolution of adenosine concentration: fixed potential amperometry (FPA) and fast scan cyclic voltammetry (FSCV). Both, however, suffer from cross-sensitivity to other compounds.

FPA uses an enzyme coated microelectrode, held at a constant potential, to detect adenosine (Fig. 4.1a) (Dale et al., 2005). The enzymes break down adenosine, through inosine and hypoxanthine, to urate and hydrogen peroxide. The hydrogen peroxide is then detected amperometrically by the platinum microelectrode polarised to 500 mV (Llaudet et al., 2003; Dale et al., 2005). A permselective layer over the enzymes prevents direct oxidation of other analytes such as ascorbate, 5HT and dopamine. Enzymatic specificity means that the response is highly specific to the purines adenosine, inosine and hypoxanthine. The sensors are, however, not specific to adenosine. As inosine and hypoxanthine are steps in the enzymatic cascade, presence of these compounds endogenously also results in an amperometric signal. Measurement with an inosine FPA biosensor (a sensor identical to an adenosine biosensor without adenosine deaminase) gives a signal corresponding to the local inosine and hypoxanthine. Subtraction of the signal from an inosine sensor from that of an adenosine sensor could give a signal specific to adenosine, however, the purine

concentration in the neocortex has been shown to be heterogeneous on the scale of the minimum separation of two FPA biosensors and so this method is ineffective (Kerr et al., 2013; Wall and Richardson, 2015).

FSCV detects adenosine by oxidising it directly (Swamy and Venton, 2007; Chang et al., 2012; Van Gompel et al., 2014; Nguyen et al., 2014). A triangular waveform is applied to a microelectrode and the resulting current is measured. The applied voltage results in the oxidation and reduction of many compounds, including adenosine. The current at the voltages of the characteristic oxidation peaks of adenosine in the voltammagram gives a measure of the local adenosine concentration (Swamy and Venton, 2007). The voltages at which the adenosine oxidation peaks occur are relatively specific to adenosine, however, other analytes that are likely to exhibit transient dynamics in response to ictal activity also give rise to finite currents at these voltages. Furthermore, it is possible that FSCV may modify the local adenosine tone and available stock by directly causing adenosine release. It is known that electrical stimulation can elicit adenosine release (Klyuch et al., 2011; Chang et al., 2012). Whilst the effect of the FSCV waveform would be constant on the time-scale of ictal events it may modify transient adenosine release by chronically depleting the available stock.

Both FPA and FSCV provide high spatio-temporal information about extracellular adenosine concentration, albeit both with cross-sensitivity to other compounds. The cross-sensitivities of the two techniques are, however, different. In combination they provide a more specific measure of adenosine than can be obtained with either technique in isolation.

Adenosine provides critical negative feedback during seizure activity, however, the spatio-temporal dynamics of peri-ictal adenosine release are poorly characterised. Here we use a transformed form of the intrinsic optical signal (Thomas et al., 2015) to determine the spatio-temporal dynamics of seizure activity in acute neural tissue slice and perform simultaneous FPA and FSCV to resolve the associated adenosine dynamics and thereby characterise the spatio-temporal dynamics of adenosine release associated seizure activity.

4.3 Materials and Methods

Slice preparation

Parasagittal slices of cortex (400 μm) were prepared from male Sprague-Dawley rats at postnatal days 18−21. In accordance with the United Kingdom Animals (Scientific Procedures) Act 1986, rats were killed by cervical dislocation and decapitated. The cerebrum was rapidly removed. Parasagittal slices were cut on a Microm HM 650V micro-slicer (Carl Zeiss, Welwyn Garden City, United Kingdom) in cold (2−4^{o}C) high Mg^{2+}, low Ca^{2+} artificial cerebrospinal fluid (aCSF) composed of (in mM): 127 NaCl, 1.9 KCl, 8 $MgCl_2$, 0.5 $CaCl_2$, 1.2 KH_2PO_4, 26 $NaHCO_3$, 10 D-glucose (pH 7.4 when bubbled with 95% O_2 − 5% CO_2). Slices were stored in aCSF (1.0 mM $MgCl_2$, 2.0 mM $CaCl_2$) in a Gibbs chamber at 34^{o}C for at least one hour before recording. The number of slices used for each experiment was determined empirically from the results of preliminary tests. All experiments were approved by the University of Warwick Animal Welfare and Ethical Review Body.

Recording from slices

Slices were transferred to a bespoke recording chamber after Thomas et al. (2013) that supported the tissue in the aCSF flow, allowing it to be perfused on both sides. Slices were perfused with aCSF at a constant flow rate of 4 ml/min at 35 ± 0.5 ^{o}C. All tubing was gas tight (Tygon) and solutions were vigorously bubbled with 95% O_2 − 5% CO_2. Slices were allowed to recover in the chamber for 40 minutes before recording.

Induction of network activity

Population spikes were induced by application of 40 μM bicuculline methiodide (Sigma Aldrich, Gillingham, UK). Electrographic seizure activity was induced by a gradual change from standard aCSF to Mg^{2+} free aCSF (Mody et al., 1987). What is believed to be mixed state activity was induced by rapidly changing from normal aCSF to Mg^{2+} free aCSF. Spreading depression was induced by rapidly changing from normal aCSF to Mg^{2+} free aCSF with 3.8 mM KCl.

Local Field Potential recording

Extracellular recordings were made with aCSF filled electrodes, tip diameters 15 μm, placed on the surface of the tissue. The recordings were made using A-M

systems amplifiers with bandpass filter 10 Hz to 3 kHz and digitised online (10 kHz) with a CED Power1401 mk II digitiser controlled by Spike2 software (Cambridge Electronic Design, Cambridge, UK).

Fixed potential amperometry

Adenosine FPA biosensors (Fig. 4.1a) were obtained from Sarissa Biomedical (Coventry, UK). These consisted of a 50 μm diameter, 500 μm long, Pt wire coated with a matrix containing ADA, nucleoside phosphorylase, and xanthine oxidase (responsive to adenosine, inosine and hypoxanthine), then further coated with a permselective layer to prevent direct oxidation of other analytes such as ascorbate, 5HT and dopamine (Llaudet et al., 2003). Null sensors, also from Sarrisa Biomedical, identical to the adenosine biosensors except lacking the enzymes, were used in preliminary experiments to control for nonspecific electro-active interferents. No responses were detected on the null sensors and so they were not used for later experiments. The biosensors were inserted through the tissue. Biosensor signals were acquired at 1 kHz with a Micro CED (Mark 2) interface using Spike (version 6.1) software (Cambridge Electronics Design). When not simultaneously recording with FSCV the FPA signal was low pass filtered at 100 Hz, thereby simultaneously detecting the LFP associated with electrographic seizure activity. When simultaneously recording with FSCV a low pass filter of 1 Hz was used. Preliminary experiments showed adenosine transients to be sufficiently slow for this filtering not to affect the transients recorded, whilst also suppressing the aretfacts resulting from the FSCV waveform. The times of the FSCV artefacts was recorded and they were removed from recordings retrospectively, but by suppressing them live, the biosensor responses could be used to monitor experiments in real-time. After each experiment, the biosensors were calibrated with 10 μM adenosine.

Local field potential recording from biosensor

The LFP was extracted from FPA recordings (where a 100 Hz low pass filter was employed) by Fourier transforming the recording, separating the low (<1 Hz) and high (>1 Hz) frequency components and Fourier transforming the result to give the adenosine transients and the LFP respectively.

Fast Scan Cyclic Voltammetry

FSCV was carried out by applying a triangular waveform to a 7 μm diameter, 500 μm long, carbon fibre micro-electrode (CFME, Fig. 4.1d, purchased from Sarissa Biomedical, Coventry, UK) inserted in to the tissue. The waveform was applied using a CED Power1401 mk II digitizer and consisted of a baseline of -0.4 V with a triangular waveform at 10 Hz rising to 1.6 V and returning to baseline in 10 ms (Fig. 4.1e). The voltage across a 4.6 kΩ resistor in series with the CFME was measured using an A-M systems amplifier with bandpass filter 0.1 Hz to 20 kHz and was digitised online (20 kHz) with a CED Power1401 mk II digitiser controlled by Spike2 software (Cambridge Electronic Design, Cambridge, UK). The current corresponding to the applied voltage waveform was calculated using Ohm's law. The current at the voltages associated with adenosine oxidation (Swamy and Venton, 2007) were identified and converted to a time series retrospectively.

Intrinsic optical signal imaging

Network activity was inferred from the intrinsic optical signal (IOS) recorded from the tissue (Thomas et al., 2015). The tissue was illuminated by three L-7113VGC-E LEDs (Kingbright, New Taipei City, Taiwan). The LEDs were connected in parallel to each other and in series to a 100 Ω resistor. An HY3003 DC power supply (Digimess, Derby, UK) was used to supply 6.2 V, giving a total current through the LEDs of 30 mA. The peak in the emission spectrum of the LEDs was 520 nm, this maximised the signal-to-noise ratio of the recording given the wavelength dependence of the camera's sensitivity and the wavelength dependence of the signal amplitude (Thomas et al., 2015). The incident light intensity was optimised to give a typical baseline reflected intensity 70 % of that which would saturate the camera sensor, this prevented inhomogeneities in the reflected intensity resulting in regions saturating the camera sensor whilst maximising the signal to noise ratio. The LEDs were positioned around the slice to avoid shadows resulting from the microelectrodes. The LEDs were angled to illuminate the slice at approximately 25^o to normal. The reflected light was recorded using a Hitachi KP-M1A camera (Scientifica, Bedford, UK). Recordings were made at 25 frames per second (fps) at a resolution of 640 x 480 pixels. The recordings were saved as uncompressed avi files on external hard drives. The time base of the optical recording was synchronised

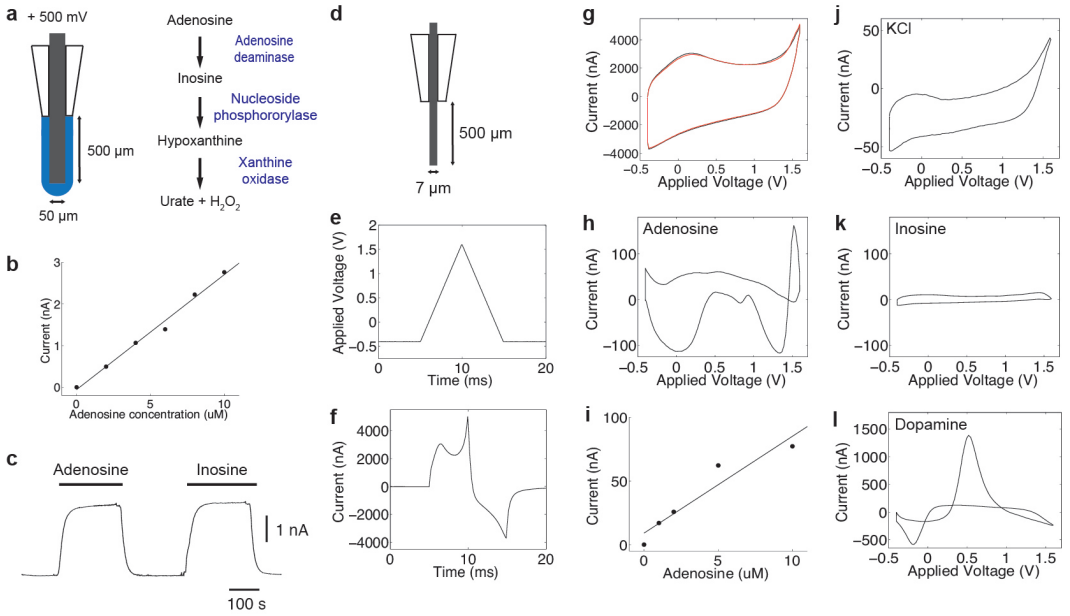

Figure 4.1: Methods for the measurement of adenosine: Fixed Potential Amperometry (FPA) and Fast Scan Cyclic Voltammetry (FSCV). (a) Schematic of FPA biosensor. (b) Example calibration of an FPA biosensor. (c) Example response of an FPA biosensor to 10 μM adenosine and 10 μM inosine, showing the cross sensitvity of the biosensors. (d) Schematic of a carbon fibre microelectrode (CFME) used for FSCV. (e) Applied voltage waveform. (f) Example current measured in response to application of voltage shown in (e). (g) Voltammagrams of aCSF (black) and aCSF and 10 μM adenosine (red). (h) Background subtracted voltammagram of 10 μM adenosine. (i) Example calibration of FSCV to adenosine. (j-l) Example cross sensitivities of FSCV: subtracted voltammagrams of potassium chloride (j), inosine (k) and dopamine (l).

to the others (LFP, FPA, FSCV) by a TTL pulse to both the digitiser and the illuminating LEDs at the beginning and end of recordings. The recorded IOS was transformed to the tIOS (Thomas et al., 2015) which then accurately reflected the spatial and temporal dynamics of the underlying network activity (Fig. 4.2).

Pharmacological manipulation

All drugs were made up as 10−100 mM stock solutions, stored frozen, and then thawed and diluted with aCSF on the day of use. Adenosine was purchased from Sigma (Poole, UK). Erythro-9-(2- hydroxy-3-nonyl)adenine (EHNA, an adenosine deaminase inhibitor), Nitrobenzylthioinosine (NBMPR, an ENT1 inhibitor) and Dipyridamole (an inhibitor of ENT1 and ENT2) were purchased from Tocris-Cookson (Bristol, UK).

Analysis and modelling

Data analysis and modelling were both carried out using Matlab R2011b (MathWorks, Natick, USA) using custom scripts.

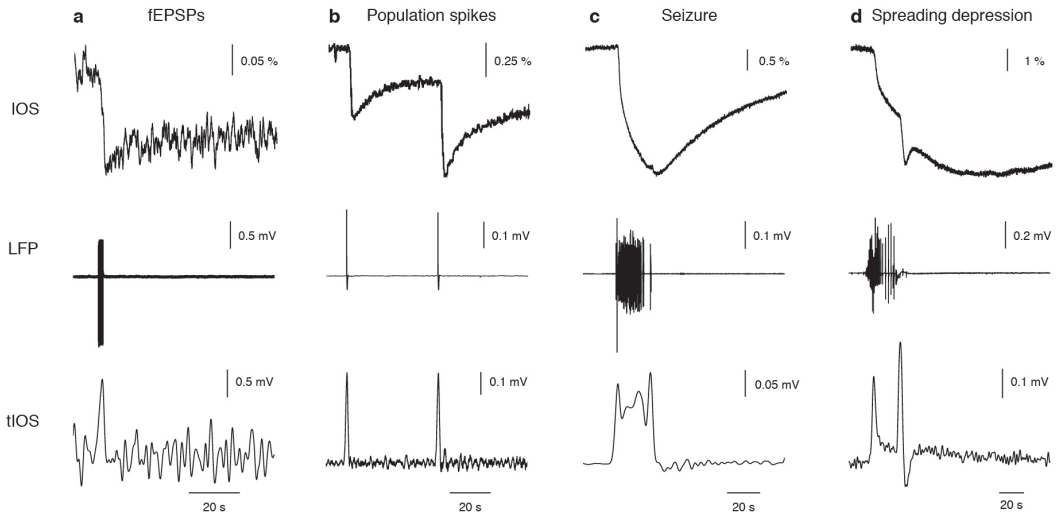

Figure 4.2: Recovery of an LFP like time-series from the IOS recorded. (a) train of fEPSPs (20 at 10 Hz) (b) population spikes (c) electrographic seizure activity and (d) spreading depression. For all types of activity, the top row shows the change in reflected intensity. The second row shows the associated LFP. The third row shows the result of the transformation to the tIOS. The tIOS accurately reflects the dynamics of the LFP, with the exception of spreading depression, which produces a characteristic tIOS waveform.

4.4 Results

The macroscopic structure of the neocortex allows the spatio-temporal dynamics of extracellular adenosine to be readily separated into two components. The structure of the neocortex is approximately translationally invariant perpendicular to the normal to the nearest point on the pial surface. Long range connections in these directions are, however, less frequent and so the level of neuronal activity can vary significantly as a function of these directions. Normal to the pial surface, although continuous tissue, the neocortex has a layered structure, each layer having a distinct cellular composition. The degree of connection between cells lying close to the same normal is, however, high and so variation in the level of neuronal activation is relatively small.

The spatial dynamics of purines were, therefore, separated into the direction of the local surface normal, along which the cellular composition of the tissue varied significantly, but the degree of activation could be considered uniform, and the directions perpendicular to the surface normal along which the composition of the tissue did not vary significantly but the degree of activation did (Fig. 4.3a). For the 400 μm tissue slices used in this study, the degree of neuronal activation was also

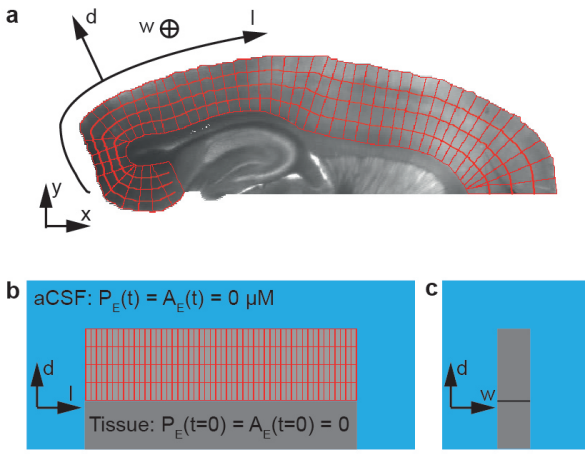

Figure 4.3: Separation of spatial components. (a) Example micrograph of a tissue slice with superimposed grid reflecting the organisation of the tissue. A cartesian coordinate system (x-y-z) and a natural coordinate system (l-d-w) are indicated. (b) A schematic of the tissue slice shown in (a) transformed on to a rectilinear grid. (c) Projection of tissue slice, normal to that shown in (b).

considered to be invariant along the short dimension perpendicular to the surface normal (w, Fig. 4.3c).

With an appropriate Jacobian, the structure of the neocortex can be transformed on to a rectilinear grid (Fig. 4.3b) with only structural variation along one direction, only activation variation along the other and no variation in either activation or structure along the third.

We assume extracellular purine (P_E) dynamics to be governed by diffusion, removal (B_P) and release (R_P), where the release is dependent on the current local level of activation ($E_P(l,t)$), the available stock of purine (P_S) and the nature of the local tissue ($D_P(d)$). Given the above assumptions this gives:

$$\frac{\partial P_E(l,d,w,t)}{\partial t} = D'\nabla^2(P_E(l,d,w,t)) - B_P(P_E(l,d,w,t)) + R_P(E(l,t), P_S(l,d,t), D_P(d)). \tag{4.1}$$

Where D' is a diffusion constant, assumed to be equal for adenosine, inosine and hypoxanthine, modified to account for the tortuosity of the tissue. We assume a similar equation applies for the dynamics of extracellullar adenosine (A_E, with B_A, R_A, A_S and D_A). Here we seek to test this model and constrain the parameters and functional forms.

Layer dependence of purine release

To investigate the layer dependence of purine release, three FPA biosensors were inserted in to somatosensory cortex, one in layer I, one in layer II/III and one in layer V; all along the same normal to the pial surface. Network activity was then induced in the tissue and was recorded optically. The optical recording was used to ensure that the active region completely encompassed the biosensors and that they were not close to the boundary of the active region.

Two types of response were detected, a monophasic rise in purine concentration associated with network activity induced by gradually reducing the Mg^{2+} concentration of the perfusing aCSF, thought to be electrographic seizure activity, and a biphasic rise in purine concentration associated with network activity induced by a rapid change from standard aCSF to Mg^{2+} free aCSF, thought to be mixed state activity.

The network activity induced by a gradual reduction in Mg^{2+} concentration caused a transient monophasic rise in purine concentration on all three biosensors (n=7, Fig. 4.4a). The temporal dynamics and peak amplitudes of the purine transients in layers II/III and V were not significantly different: layer II/III peak: 1.0 ± 0.1 μM; layer II/III time to maximum: 41 ± 1 s; layer V peak: 1.3 ± 0.2 μM; layer V time to maximum: 39 ± 4 s. The dynamics of the transients in layer I were, however, different to those in layers II/III and V. The transients in layer I were smaller in amplitude than those in layers II/III and V ($P<0.01$); layer I peak: 0.3 ± 0.1 μM and the time to maximum was greater in layer I than in layers II/III and V ($P<0.01$), time to maximum in layer I: 90 ± 10 s.

The network activity induced by a rapid reduction in Mg^{2+} concentration caused a transient biphasic rise in purine concentration on all three biosensors (n=7, Fig. 4.4b). The initial downward deflection on the biosensor recordings was followed by an initial rise and plateau phase followed by a second rising phase and subsequent decay. Neither the peak amplitudes nor the time to maximum were significantly different across all three biosensors: layer I peak: 3.6 ± 1.0 μM; layer I time to maximum: 126 ± 14 s; layer II/III peak: 7.6 ± 2.0 μM; layer II/III time to maximum: 110 ± 26 s; layer V peak: 6.7 ± 2.0 μM; layer V time to maximum: 110 ± 25 s.

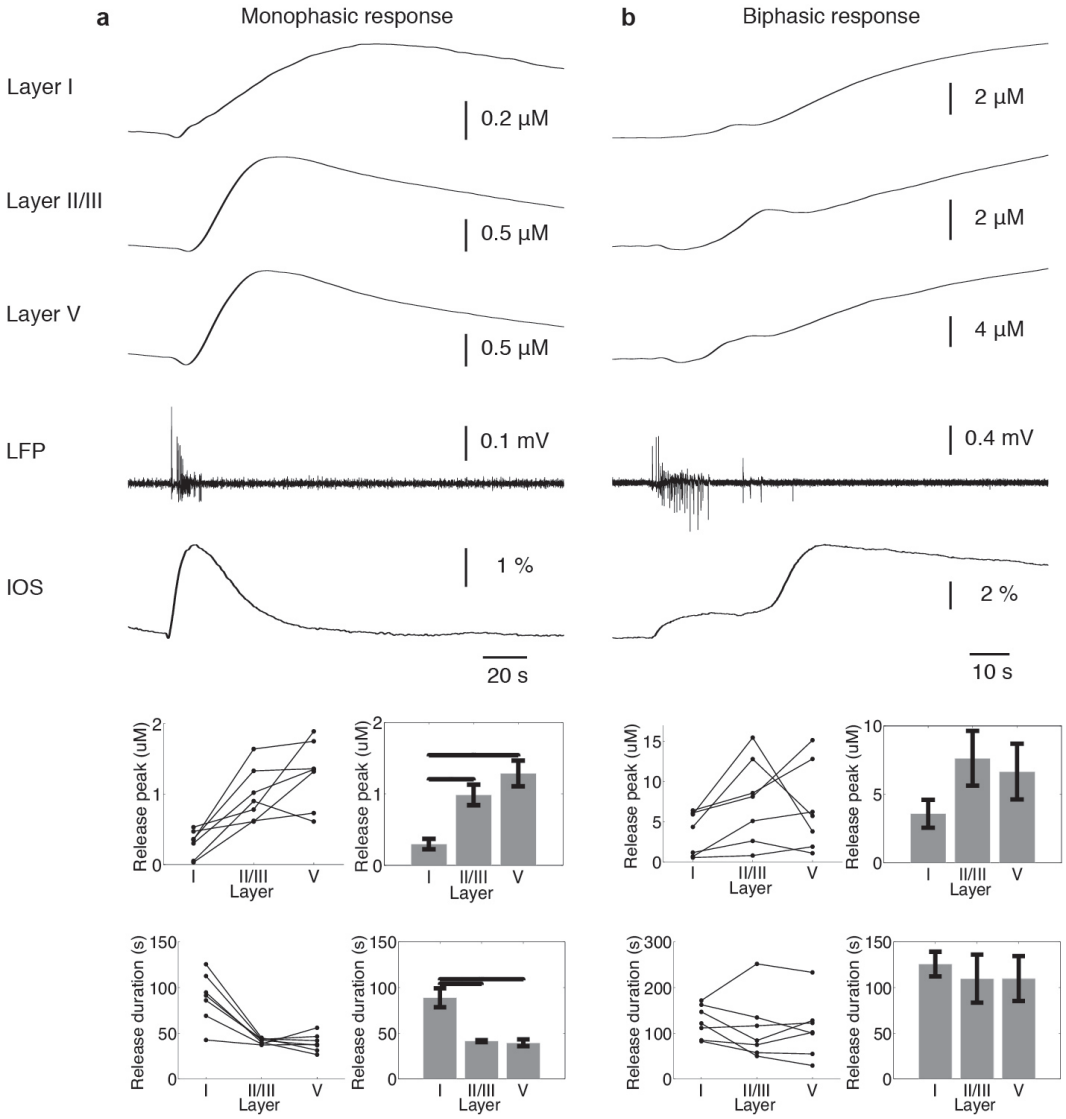

Figure 4.4: Layer dependence of monophasic (a) and bisphasic (b) purine release as measured with FPA biosensors. The top panels show example traces from the biosensors and the associated intrinsic optical signals. The bottom panels show summary data (n=7 for both types of response), bars indicate result of a paired sample t-test $< 1\%$.

For all other experiments a gradual change to Mg^{2+} free aCSF was employed to induce network activity, as this was thought to cause electrographic seizure activity.

Model of layer dependent release

Layer I has different boundary conditions to layers II/III and V. Tissue within the slice preparation in layers II/III and V has a zero purine concentration boundary condition along the two cut surfaces. Layer I of a tissue slice also has a zero purine concentration boundary condition across the pial surface. We modelled the system

to investigate whether this difference in boundary conditions explains the difference in purine dynamics in layer I.

Given the measurements were made from locations distant from the edges of the active region, as confirmed optically, purine flux along direction l (Fig. 4.3a,b) could be ignored. This therefore resulted in a two dimensional reaction-diffusion equation. Assuming breakdown of hypoxanthine to be much slower than its loss from the slice by diffusion (Klyuch et al., 2011), breakdown can be ignored, leaving:

$$\frac{\partial P_E(d,w,t)}{\partial t} = D'\nabla^2(P_E(d,w,t)) + R_P(d,w,t). \tag{4.2}$$

The case where purine release is a delta function at all position within the tissue at $t = 0$ was solved analytically, giving:

$$P_E(w,d,t) = \sum_{n=1}^{\infty}\sum_{m=1}^{\infty} \frac{4\Omega}{nm\pi^2}(1-\cos(n\pi))(1-\cos(\frac{m\pi}{2}))\cdot\sin(\frac{n\pi}{\alpha}w)\sin(\frac{m\pi}{\beta}d)e^{-D'(\frac{n^2\pi^2}{\alpha^2}+\frac{m^2\pi^2}{\beta^2})t} \tag{4.3}$$

where α is the thickness of the tissue, β is the depth of the neocortex (Layers I - V) and Ω is the adenosine concentration in the tissue immediately after release. This result was then used to validate a numerical scheme to solve the reaction diffusion system (Fig. 4.5). The numerical result accurately matched the analytic one (Fig. 4.5c) and so was used to solve the system with more complex release dynamics.

Considering a burst of electrographic seizure activity to be made up of spikes occurring at a constant, high, firing rate, with the duration of the burst much smaller than the re-stock time constant, it is reasonable to approximate the discrete release of a resource depletion model (Klyuch et al., 2011) with a decaying exponential. We therefore solved Eq. 4.2 with exponential release dynamics and compared the resulting purine concentration dynamics at a point adjacent to the pial surface, representative of the dynamics in layer I, to those at a point in the middle of the active region, representative of the dynamics in layer V (Fig. 4.6a).

With spatially uniform release of purine, the peak in purine concentration in layer I was smaller than that in layer V (Fig. 4.6 b,c), as was observed experimentally. The time of the peak was, however, earlier in layer I than in layer V (Fig. 4.6d),

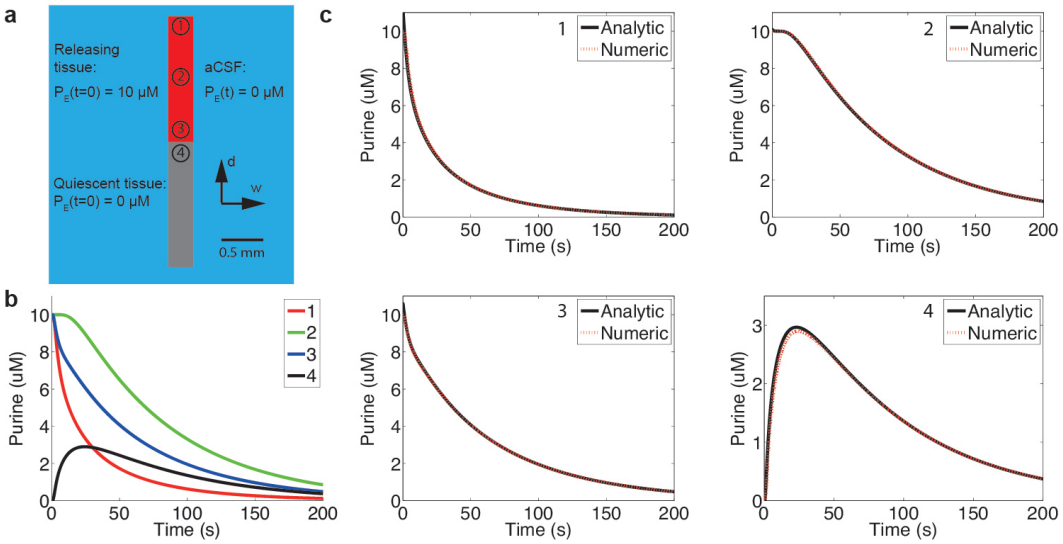

Figure 4.5: Validation of numerical PDE solution scheme. (a) Schematic of test geometry. (b) Analytic solution of diffusion equation at the four locations shown in (a). (c) Comparison of numeric and analytic solutions at the four regions shown in (a) showing good agreement between the two solutions.

which was inconsistent with the experimental results. We therefore modelled the system without purine release in the region adjacent to the pial surface, considering a range of sizes of this region (Fig. 4.6a,e). In this system the time to peak was greater in layer I than in layer V (Fig. 4.6 b,g), as observed experimentally, and again the peak in layer I was smaller than that in layer V (Fig. 4.6h). However, experimentally there was a positive correlation between the ratio of release of purine in layer I to layer V and the lag to the peak (Fig. 4.6e). The model without release in layer I did not exhibit this property, instead showing a negative correlation between relative release and lag to peak as the duration of release was varied (Fig. 4.6f).

Diffusion correction

Tissue slices allow access and control not possible *in vivo*. However, a consequence of slicing the tissue and maintaining it in aCSF is a significant modification to the boundary conditions of the tissue. The cut surfaces of slices are exposed to a rapidly replaced solution not containing any purines. This is effectively a zero concentration boundary condition across all of the tissue, this does not reflect the *in vivo* conditions and leads to a significant modification to decay dynamics.

The loss of purines from the tissue by diffusion can, however, be corrected for. Assuming the release of purine to be slowly varying with depth (d) on the

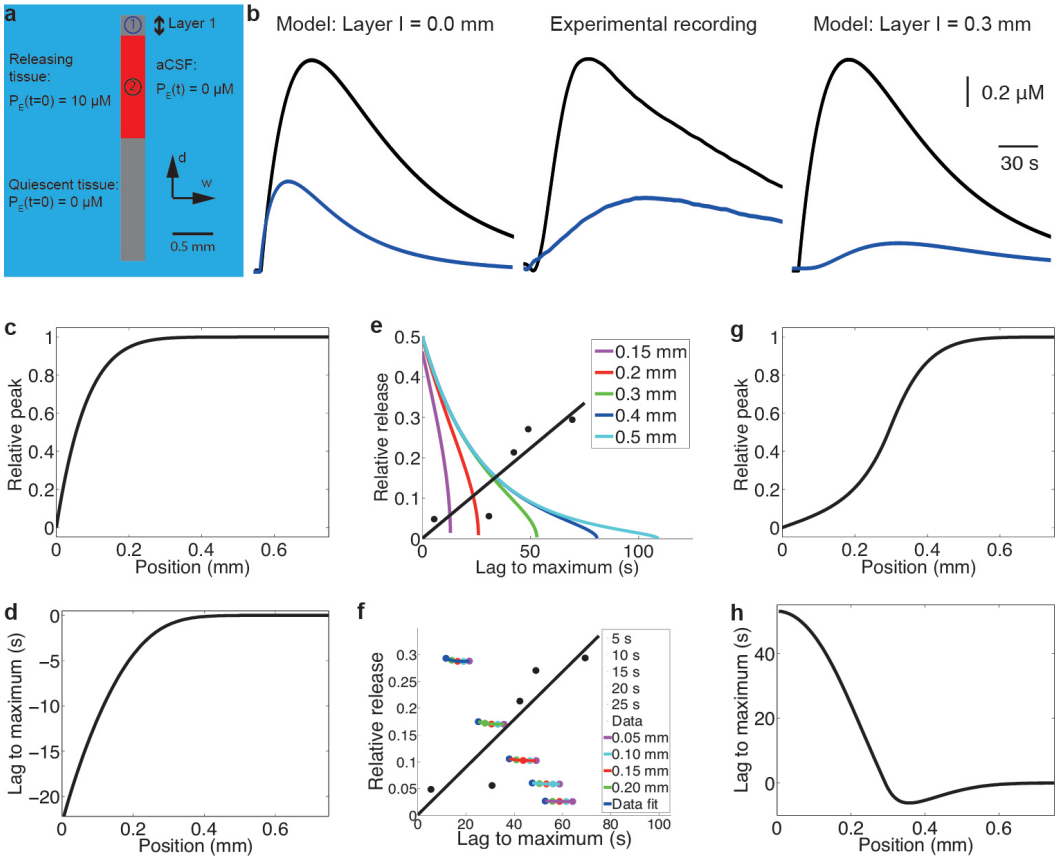

Figure 4.6: Model of release as a function of depth into neocortex. (a) Schematic of system, indicating a non-releasing layer I. (b) Time courses of purine concentration for location 1 (blue) and 2 (black) in (a). (c) Relative peak in purine concentration as a function of depth into the neocortex for a releasing layer I. (d) Lag to peak in purine concentration as a function of depth in the neocortex for a releasing layer I. (e) Relative peak in purine concentration plotted against the lag to the maximum for a range of depths of layer I, all points along the line equidistant from both cut surfaces are shown (colours), and experimental results and linear fit (black). Relative peak in purine concentration plotted against the lag to the maximum for a 300 μm layer I. A number of durations of release are shown at a number of distances from the pial surface. (g) Relative peak in purine concentration as a function of depth into the neocortex for a 300 μm layer I. (h) Lag to peak in purine concentration as a function of depth in the neocortex for a 300 μm layer I.

length scale of the thickness of the slice, considering a point within a large releasing region, away from both the dorsal and ventral edges (Fig. 4.7a) and ignoring removal of purine by the biosensor, the concentration of purine can be considered to be invariant in the plane of the slice (directions d and l). The temporal dynamics of purine concentration can, therefore, be considered as a one dimensional reaction diffusion problem.

The biosensor inserted through the tissue (Fig. 4.7b) then measures the integral of the extracellular purine concentration (P_E) as a function of w:

$$M_P(t) = \gamma \int_0^\alpha P_E(w,t)dw. \tag{4.4}$$

The one dimensional reaction diffusion equation for purine concentration is assumed to be:

$$\frac{\partial P_E(w,t)}{\partial t} = D' \frac{\partial^2 P_E}{\partial w^2} + R_P(w,t) - B_P(P_E(w,t)). \tag{4.5}$$

Where D' is a diffusion constant, assumed to be equal for adenosine, inosine and hypoxanthine, modified to account for the tortuosity of the tissue; $R_P(w,t)$ is the rate of release of purine and B_P is the rate of breakdown of purine.

The functions of interest in Eq. 4.5 are $R_P(w,t)$ and $B_P(P(w,t))$, while what is measured experimentally is $M_P(t)$(Eq. 4.4). We seek to identify an operation to determine $R_P(w,t)$ and $B_P(P_E(w,t))$ given $M(t)$.

Integrating Eq. 4.5 gives:

$$\frac{\partial}{\partial t}\int_0^\alpha P_E(w,t)dw = \int_0^\alpha D' \frac{\partial^2 P_E(w,t)}{\partial w^2}dw + \int_0^\alpha R_P(w,t)dw - \int_0^\alpha B_P(P_E(w,t))dw. \tag{4.6}$$

Slice thickness (α) is small, so the release of purine is considered to be invariant along this direction. Substituting for the expression for $M(t)$ in to Eq. 4.6 gives:

$$\frac{\partial}{\partial t}\left(\frac{1}{\gamma}M_P(t)\right) = D'\left[\frac{\partial P_E(w,t)}{\partial w}\right] + \alpha R_P(w,t) - \int_0^{\alpha} B_P(P_E(w,t))dw. \tag{4.7}$$

If we then assume that $B_P(P_E(w,t))$ is proportional to $P_E(w,t)$ with a constant of proportionality of $\frac{1}{\tau_P}$:

$$\frac{\partial P_E(w,t)}{\partial t} = D'\frac{\partial^2 P_E}{\partial w^2} + R_P(w,t) - \frac{P_E(w,t)}{\tau_P}. \tag{4.8}$$

Substituting for the resulting expression for $M_P(t)$ this gives:

$$\frac{1}{\gamma}M_P(t) = D'\left[\frac{\partial P_E(w,t)}{\partial w}\right] + \alpha R_P(w,t) - \frac{M_P(t)}{\gamma\tau_P}. \tag{4.9}$$

Combining Eqs. 4.5 and 4.9 to eliminate $R_P(w,t)$ yields:

$$\frac{\partial P_E(w,t)}{\partial t} = \frac{1}{\alpha\gamma}\frac{\partial M_P(t)}{\partial t} + \frac{1}{\alpha\gamma\tau}M_P(t) + D'\frac{\partial^2 P_E(w,t)}{\partial w^2} - \frac{P_E(w,t)}{\tau_P} - \frac{D'}{\alpha}\left[\frac{\partial P_E(w,t)}{\partial w}\right]_0^{\alpha}. \tag{4.10}$$

Assuming $P_E(w, t=0) = 0$, a numerical integration scheme can then be used with Eq. 4.10 to determine $P_E(w,t)$ from $M_P(t)$.

Substituting Eq. 4.10 in to Eq. 4.8 then gives an expression for $R_P(w,t)$. Assuming that the breakdown of hypoxanthine is much slower than loss of purines from the slice by diffusion (Klyuch et al., 2011), τ_P can be assumed to be infinite and $R_P(t)$ can be recovered from $M(t)$:

$$R(t) = \frac{1}{\alpha\gamma}\frac{\partial M_P(t)}{\partial t} + \frac{M_P(t)}{\alpha\gamma\tau_P} - \frac{D'}{\alpha}\left[\frac{\partial P_E(w,t)}{\partial w}\right]_0^{\alpha}. \tag{4.11}$$

The same argument can be used to recover adenosine dynamics from $M_A(t)$, however, τ_A in that case is finite and so needs to be determined.

Purine release

To characterise purine release in response to electrographic seizure activity, an FPA biosensor was inserted into layer II/III of somatosensory cortex and electrographic seizure activity was induced (n=15). The activity was recorded optically and the

active region was thereby confirmed to encompass the location of the biosensor and extend significantly beyond it (Fig. 4.7a). The approach to correction for diffusion derived above could, therefore, be applied to the measured purine concentration.

Figure 4.7c shows an example LFP trace extracted from a biosensor recording, exhibiting bursts of electrographic seizure activity. The associated biosensor measurement (Fig. 4.7d) shows typical transient increases in purine concentration with each burst of seizure activity. Applying the procedure derived in the previous section the form of the release was derived (Fig. 4.7e), showing isolated bursts of release.

A resource depletion model for purine release (Klyuch et al., 2011) was compared to the derived release dynamics. Spike times were extracted from the LFP and used as input to the model in which a proportion, f, of available purine stock was released with each spike, with a re-stock of form:

$$\frac{dP_S(t)}{dt} = \frac{P_0 - P_S(t)}{\tau_S} - fP_S(t-\epsilon)\sum \delta(t-t_k) \tag{4.12}$$

where P_S is the available purine stock, P_0 is the maximum level of the store, τ_S is the re-stock time constant, t_k are the spike times and ϵ is small and positive. This model reflected some of the temporal dynamics of the purine release, however, the measured release was significantly delayed compared to the model prediction (Fig. 4.7f,g). This comparison is, however, complicated by the transient downward deflection observed on biosensor recordings at seizure onset (Fig. 4.7f). The cause of this downward deflection is unknown, but is routinely observed (Lopatar et al., 2011; Wall and Richardson, 2015) and may be the result of the change in ionic environment around the sensor due to the sustained action potential firing.

Spatial spread

Having measured the layer dependence of purine dynamics, we then considered the dynamics along the layers (direction l, Fig. 4.3a). We inserted FPA biosensors in to layer V of the neocortex and induced electrographic seizure activity, recording the spatial dynamics of the activity optically.

We measured no transient rise in purine concentration associated with bursts

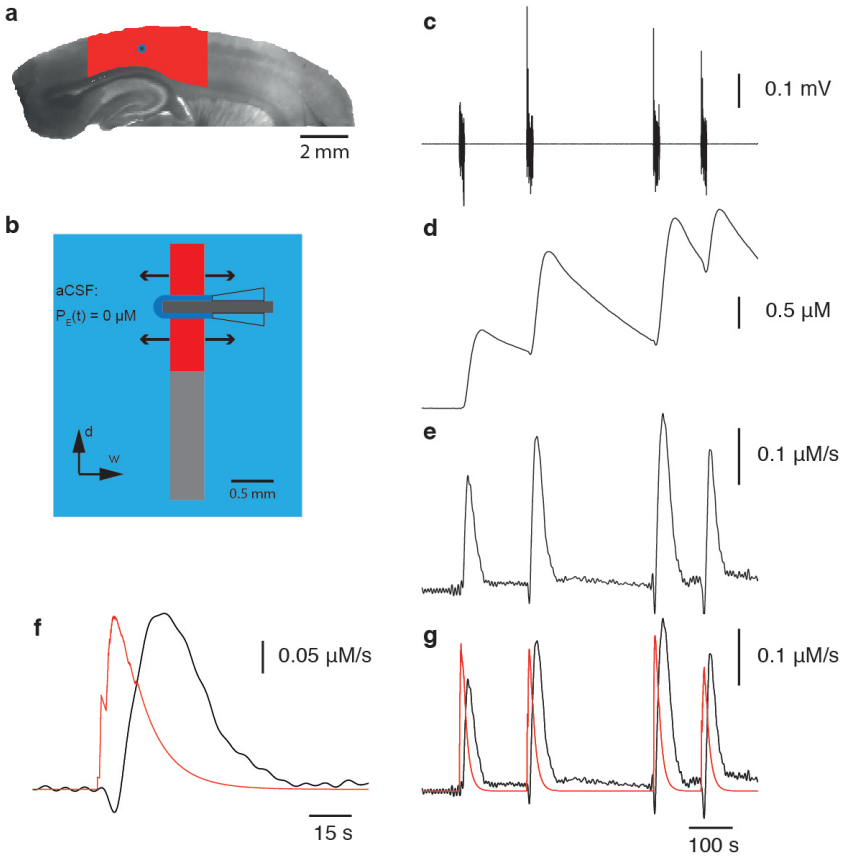

Figure 4.7: Measurement of purine release in response to electrographic seizure activity and correction for loss through diffusion. (a) Illustration of biosensor placement relative to active region (red) and the boundaries of the tissue slice. (b) Schematic, normal to (a), of biosensor placement. The releasing region is indicated in red, with loss of purine from the slice indicated by the arrows. (c) Example LFP recording showing electrographic seizure activity. (d) FPA recording associated with the LFP recording shown in (c). (e) Purine release associated with (c) recovered from (d). (f) and (g) Recovered purine release (black) and model of release driven by LFP (red). The measured purine release is significantly delayed relative to the model.

of activity unless the active region encompassed the biosensor (Fig. 4.8).

We investigated whether this is consistent with release local to the active region and spread beyond this the result of diffusion only. The layer dependence of release was not significant between layers II/III and V. Considering a point at the centre of this band, purine flux in direction d could be ignored. As with the model of layer dependent release, we assumed the breakdown of hypoxanthine to be slow compared to the loss of purine from the slice by diffusion. This yielded the reaction-diffusion equation:

$$\frac{\partial P_E(l,w,t)}{\partial t} = D'\nabla^2(P_E(l,w,t)) + R_P(l,w,t). \tag{4.13}$$

Solving this equation using the numerical scheme discussed above showed that, in a tissue slice, spread of purine from a releasing region in to adjacent tissue is limited (Fig. 4.9). Peak purine concentration was 10 % of its maximum 170 μm from the boundary of the active region in to the quiescent region, consistent with experimental results.

Simultaneous FPA and FSCV

Having characterised the spatio-temporal dynamics of total purine, we carried out simultaneous FPA and FSCV to resolve the dynamics of adenosine specifically (n=7). We inserted an FPA biosensor in to layer II/III of somatosensory cortex and a carbon fibre microelectrode (CFME) for FSCV was inserted in to layer V, along the same normal to the local pial surface as the FPA biosensor. Electrographic seizure activity was then induced in the tissue. Optical measurements were simultaneously carried out to ensure that the active region completely encompassed and extended significantly beyond the location of the biosensor and the CFME.

Both the FPA and FSCV showed transients in response to bursts of electrographic seizure activity (Fig. 4.10a). The onset of the transients recorded using FSCV was, however, more rapid than those recorded using FPA and the FSCV transients were also more rapid to rise and to decay. Application of EHNA, an adenosine deaminase (ADA) antagonist, caused both an increase in baseline and an increase in duration of transients measured using FSCV (Fig. 4.10b). EHNA suppressed the

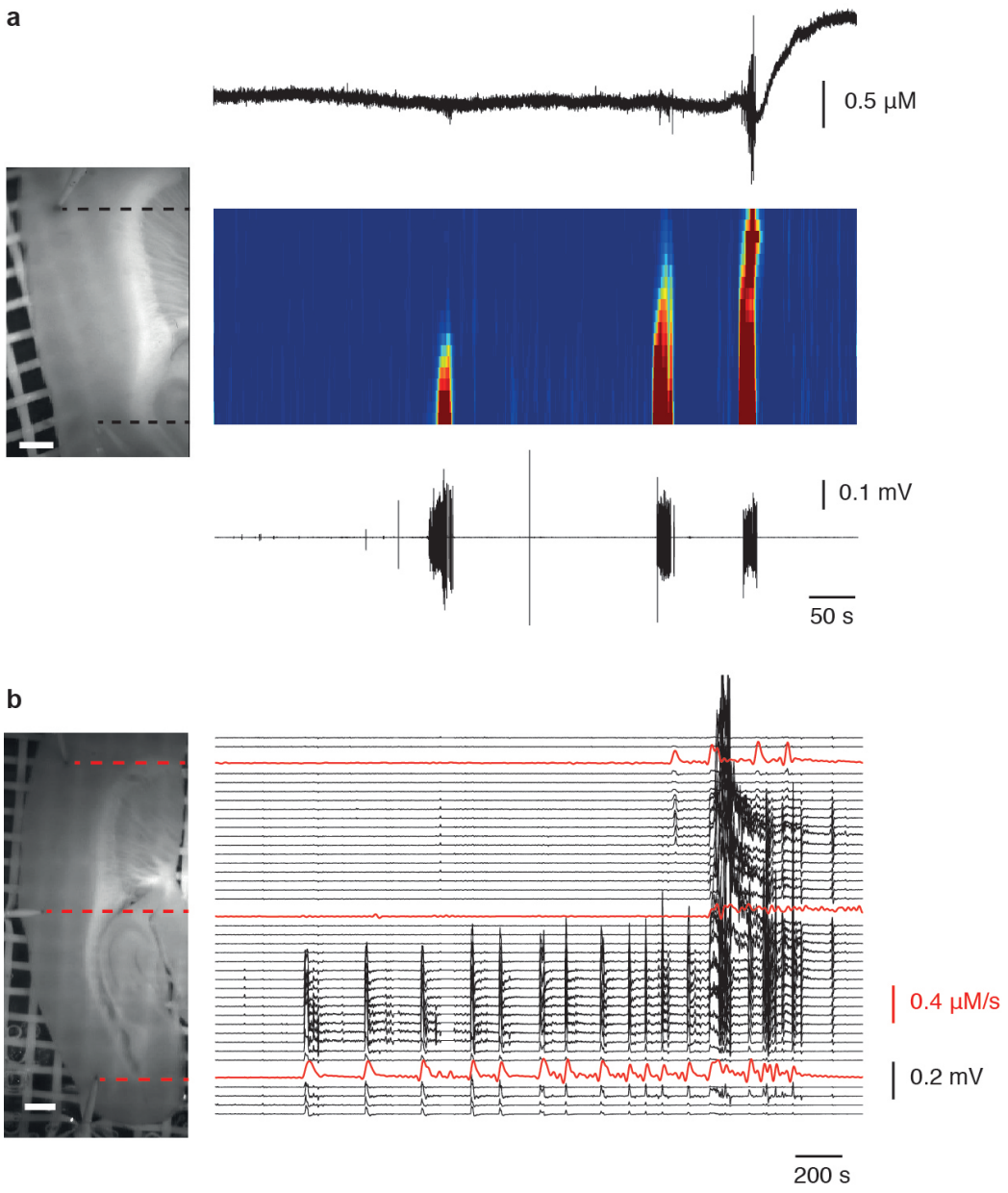

Figure 4.8: Purine release is local to region of electrographic seizure activity. (a) Left: Micrograph of tissue slice indicating location of LFP microelectrode and FPA biosensor, the scale bar corresponds to 700 μm. Right: False colour map showing spatial spread of activity across the slice as a function of time with the associated LFP recording (bottom) and biosensor measurement (top). (b) Left: micrograph of tissue slice indicating the location of three FPA biosensors. Right: tIOS for regions of interest across the tissue slice (black) and biosensor measurements (red).

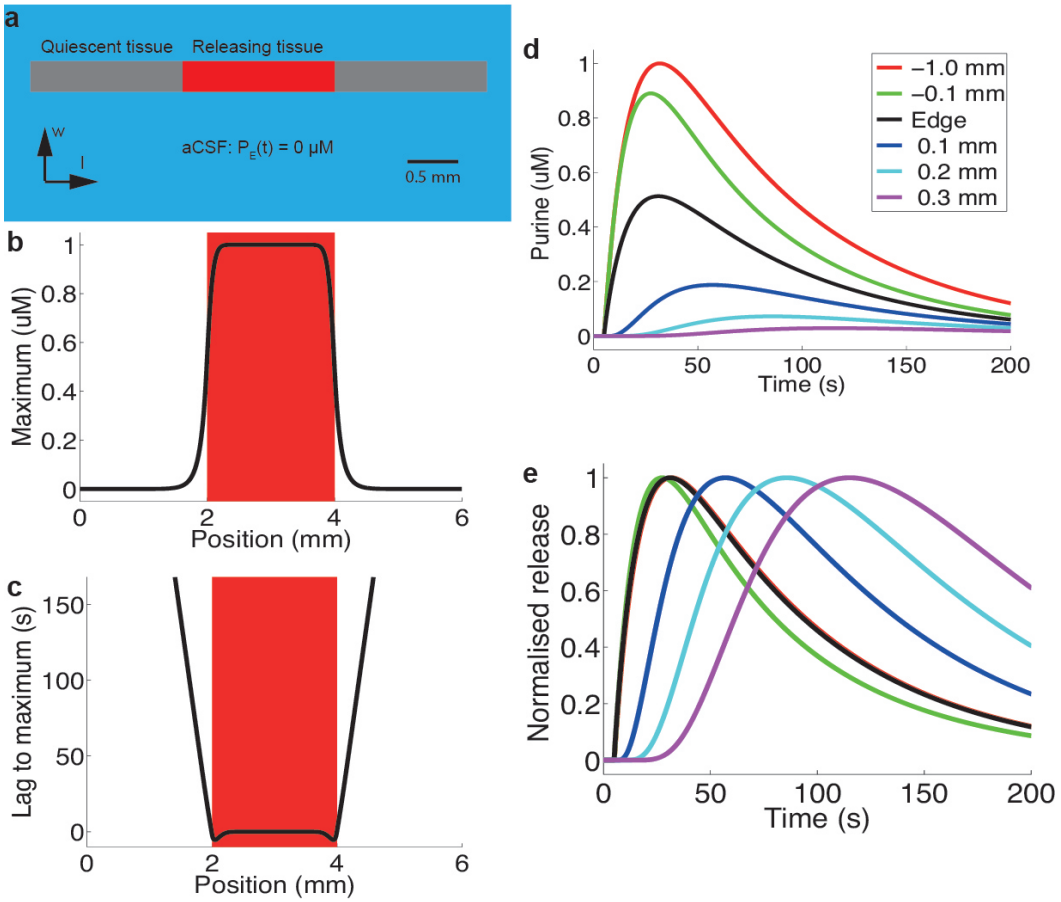

Figure 4.9: Modelling of the spatial spread of purine by diffusion in a tissue slice. (a) Schematic of system modelled. (b) Peak in purine concentration as a function of position (black) shows little penetration of purine beyond releasing region (red). (c) Lag to peak in purine concentration. (d) Time courses of purine concentration at locations adjacent to a boundary. (e) Normalised time courses of purine concentration at locations adjacent to a boundary.

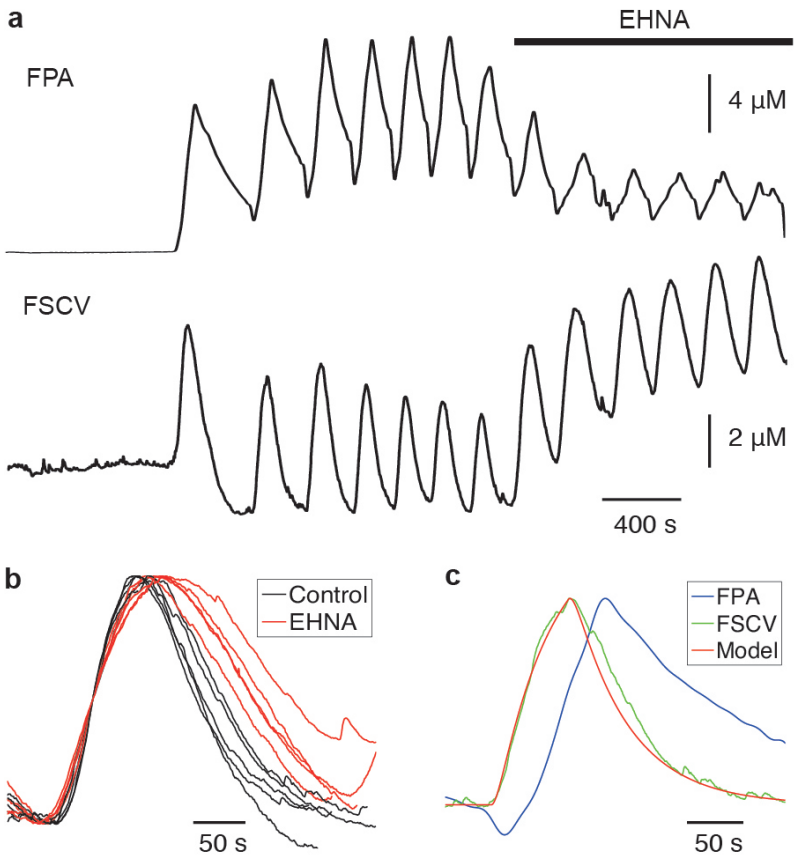

Figure 4.10: Comparison of simultaneous FPA and FSCV measurements. (a) Simultaneous FPA and FSCV measurements during a period of bursts of electrographic seizure activity. The black bar inidcates the application of EHNA. (b) Overlay of adenosine transients from FSCV from control period (black) and with EHNA (red) showing an increase in transient width with application of EHNA. (c) Plot of normalised transients measured with FPA (blue) and FSCV (green) with a stock release model (Eq. 4.12, red).

responses of the FPA biosensors as they are dependent on ADA to detect adenosine (Wall and Dale, 2007).

The transients recorded using FPA and FSCV were compared to a resource depletion model driven by the LFP associated with the transients. The model fit the FSCV recordings much more closely than those of the FPA (Fig. 4.10c).

FSCV across layers

The layer dependence of adenosine transients was investigated by simultaneously carrying out FSCV in layers I and V of somatosensory cortex, along the same local normal to the pial surface (n=5). Electrographic seizure activity was induced and monitored optically to ensure that the active region included and extended well beyond the region measured from.

Adenosine transients were detected in both layers I and V in response to

bursts of electrographic seizure activity (Fig. 4.11a). The transients were smaller in amplitude in layer I than in layer V ($P<0.05$): layer I peak amplitude: 3.4 ± 0.5 μM; layer peak: 15.6 ± 3.7 μM (Fig. 4.11b). The transients were not significantly different in duration (layer I FWHM: 46 ± 16 s; layer V: 69 ± 5 μM).

Application of EHNA or the equilibritive nucleoside transporter (ENT) inhibitors dipyridamole and NBMQR did not have a significant effect on the amplitude of adenosine transients in layer I. Inhibition of the ENTs did, however, cause an increase in the duration of the adenosine transients ($P<0.05$, Fig. 4.11c).

Inhibition of the ENTs caused a reduction in the peak amplitude in layer V ($P<0.05$) and both EHNA and ENT inhibition caused an increase in the duration of the transients ($P<0.05$). Thus ENTs appear to play a role in the release of adenosine during seizures and adenosine deaminase and ENTs play a role in adenosine removal.

4.5 Discussion

In this study we have begun to characterise the transient adenosine dynamics associated with electrographic seizure activity. By making chronic optical measurements we have been able to directly relate the spatial extent of network activity to adenosine release. As suggested by previous work (Wall and Richardson, 2015) we found that adenosine release is localised to the active area. However, contrary to previous studies (Van Gompel et al., 2014; Wall and Richardson, 2015) we found that adenosine release appears to commence with onset of seizure activity and persists extracellularly as adenosine for the duration of the seizure, only decaying after seizure termination. The release in layer I is significantly smaller than in other layers and may also be slower; this difference is not explained by the difference in boundary conditions. In the quasi two-dimensional system studied here, extracellular adenosine transients were not detected beyond the region of tissue exhibiting electrographic seizure activity.

Acute tissue slice is a preparation widely used for the study of network activity and its modulation. With such preparations there is, however, a significant modification to the boundary conditions occurring *in vivo*. A large proportion of

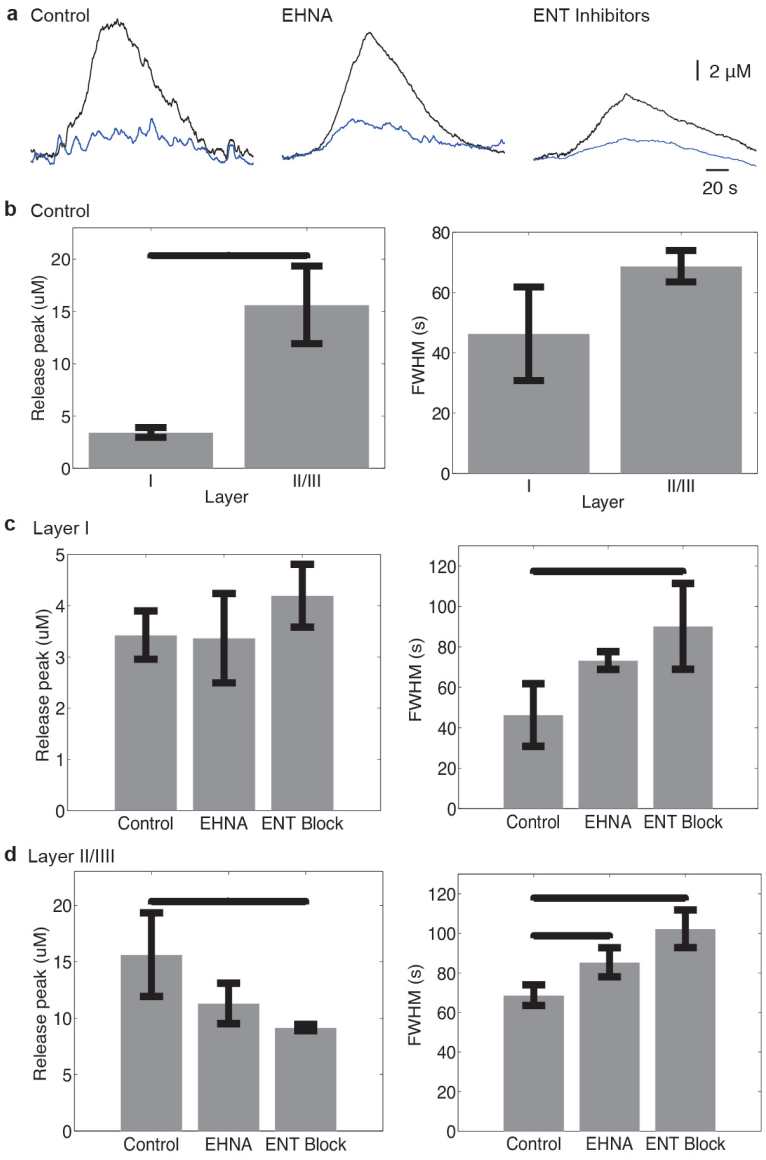

Figure 4.11: Layer dependence of adenosine release measured with FSCV. (a) Adenosine transients in response to electrographic seizure activity in layer I (blue) and layer II/III (black). (b) Comparison of release peaks (left) and the full width at half maximum of adenosine transients in layers I and II/III. (c) Effect of treatment with EHNA and ENT inhibitors on adenosine transients in layer I. (d) Effect of treatment with EHNA and ENT inhibitors on adenosine transients in layer II/III.

transiently released compounds are lost from the cut surfaces of the slice exposed to aCSF. Here we have derived an approach to correct for this loss to determine the actual release dynamics from just a measurement of the integral of the compound concentration across the thickness of the slice, as is measured using FPA or FSCV.

The dynamics of purine release in response to electrographic seizure activity has been characterised in previous work (Winn et al., 1980; During and Spencer, 1992; Dale and Frenguelli, 2009; Lopatar et al., 2011; Van Gompel et al., 2014; Wall and Richardson, 2015) . However, it is adenosine specifically that activates receptors causing negative feedback to control network activity. By simultaneously using two techniques for the measurement of extracellular adenosine, with different cross sensitivities, we have obtained data to achieve greater specificity to adenosine. We hope to develop a complete model consistent with both results for purine dynamics from FPA and for those largely specific to adenosine from FSCV. By constraining the model using the results from the two independent techniques we hope to achieve high specificity to adenosine, and thereby characterisation of a large component of the negative feedback system that suppresses seizure activity.

FPA and FSCV suggest different adenosine dynamics

In a previous study, Wall and Richardson (2015) used simultaneous measurements with adenosine and inosine FPA biosensors to resolve adenosine specifically. Adenosine biosensors respond to adenosine, inosine and hypoxanthine while inosine biosensors only respond to inosine and hypoxanthine. By subtracting the scaled recordings from the inosine biosensor from that of the adenosine biosensor the result was specifically extracellular adenosine. The application of this procedure to the transients associated with electrographic seizure activity showed no adenosine to be present. The transients measured on the adenosine and inosine biosensors exhibited the same dynamics, strongly suggesting that the compounds detected were metabolites of adenosine. This indicated that the breakdown of adenosine to inosine is extremely rapid. Further, they showed that the breakdown of inosine into hypoxanthine was a slower process.

These results would suggest that no adenosine transients would be detected with FSCV. However, we detected substantial transients at the oxidation voltage

of adenosine in response to electrographic seizure activity. The duration of these transients was increased by the application of EHNA, strongly suggesting they were adenosine. The onset of the transients was synchronous with the onset of seizure activity, the duration of the rising phase was the same as that of the seizure activity, with a decay over a similar time period.

The experimental preparation in our two studies were identical other than for the methods of adenosine detection. We hypothesise that the difference in the detection of adenosine is a result of a difference in the degree of tissue damage caused by insertion of the microelectrodes used for the two types of measurement. The microelectrodes used for the FPA were based on 50 μm diameter Pt wire, the enzyme matrix then further increased the diameter. The CFMEs used for the FSCV were 7 μm in diameter. The microelectrodes used for FPA therefore had a cross-sectional area over 50 times that of the CFMEs used for FSCV. We hypothesise that the damage to the tissue caused by the FPA microelectrodes ruptured significantly more cells, releasing formerly intracellular ADA in to the space around the electrode. This would then convert adenosine adjacent to the FPA biosensor to inosine before detection. We hypothesise that the CFMEs used for FSCV caused far less damage, that adenosine was released in to the extracellular space and was only broken down in to inosine once it entered cells through the ENTs, a slow process, allowing the detection of extracellular adenosine before it was broken down. The very rapid breakdown to inosine presented in Wall and Richardson would, therefore, be an artefact specific to the location of the biosensor. The FSCV measurement would be a more accurate reflection of adenosine dynamics, suggesting a significantly longer presence of extracellular adenosine.

This hypothesis can be tested by repeating the experiments presented in Wall and Richardson (2015) using FPA biosensors based on a 7 μm carbon fibres. This would use the same method of detection, whilst reducing the tissue damage to a level comparable to that caused by the CFMEs used for FSCV.

Adenosine release starts with seizure onset not termination

Gompel *et al.* (Van Gompel et al., 2014) made measurements of adenosine transients in response to seizure activity using FPA and FSCV in pigs *in vivo* and using FSCV

in humans *in vivo*. They found that adenosine release started just prior to seizure termination, peaking after the end of seizure events. Our measurements suggest that adenosine release starts synchronously with seizure onset, peaking at seizure termination and subsequently decaying. Our *in vitro* preparation had the advantage of allowing accurate monitoring of the region of tissue involved in seizure events. We could therefore be confident that transients were the result of activity in the tissue adjacent to the microelectrodes. Gompel *et al.* used electrocorticography to monitor seizure activity in their preparations. This approach does not allow as accurate spatial localisation of activity. The delay between seizure onset and the adenosine transients they detected may have been the result of the active region not including the location of the FPA and FSCV microelectrodes, the adenosine they detected having diffused from the active region, hence being delayed. The geometry and boundary conditions of their preparation mean that adenosine would diffuse over far greater distances than we observed in our quasi two-dimensional preparation. In further work, our model constrained using our preparation will be applied to three dimensions and the resulting length scales of diffusion investigated.

Adenosine transients in layer I are significantly smaller and slower than those in other layers

The transients measured using both FPA and FSCV in response to electrographic seizure activity were smaller in layer I than in other layers. We eliminated the possibility that this is the result of the difference in boundary conditions. The duration of the transients recorded using FPA was significantly greater in layer I than those in other layers. The same difference was not seen using FSCV, however, the signal to noise ratio of the small transients recorded in layer I was such that the FWHM could not be accurately determined from the FSCV recordings.

We propose two hypothesise for the observed differences in dynamics. Firstly, the ratio of glia to neurons in layer I is greater than that in the other layers (Shipp, 2007). The exchange dynamics of adenosine between the extracellular matrix and glia maybe slower than those with neurons. This may then explain the slower dynamics in layer I. This, however, seems unlikely to explain the observed positive correlation between the relative lag to peak and peak amplitude in layer I relative

to other layers. The second hypothesis is that an interposed transmitter is released in response to electrographic seizure activity and that adenosine is then released in response to the second transmitter (Wall and Dale, 2008). If this interposed transmitter was not released in layer I, only reaching it by diffusion, and caused adenosine release with a non-linear dependence, this may explain the observed dynamics.

ENTs appear to be involved in adenosine release

Application of ENT inhibitors significantly reduced the amplitude of the transients in response to electrographic seizure activity. We hypothesise that a significant component of the adenosine released in response to electrographic seizure activity is released through the ENTs. This component is then suppressed by inhibiting the ENTs. This component of release could be investigated further by measuring the effect of ENT inhibitors on adenosine release in response to seizures induced with calcium free aCSF (Jefferys and Haas, 1982), a regime in which there would be no contribution from exocytosis.

ADA plays an important role in regulating adenosine tone and is involved in the breakdown of transiently released adenosine

Inhibition of ADA resulted in a significant increase in extracellular adenosine concentration between bursts of seizure activity, suggesting, that ADA plays a significant role in regulating adenosine tone. In future work the effect of the inhibition of ADA in quiescent tissue will be investigated. Inhibition of ADA also increased the FWHM of adenosine transients in response to electrographic seizure activity.

4.6 Acknowledgements

This work was supported by the UK Biotechnology and Biological Sciences Research Council through grant BB/J015369/1 (to MJER and MJW and supporting MGT) and by the UK Engineering and Physical Sciences Research Council through a studentship through grant EP/F500378/1, the MOAC Doctoral Training Centre, (to MGT).

Bibliography

Barraco, R., Martens, K., Parizon, M., and Normile, H. Adenosine a_2a receptors in the nucleus accumbens mediate locomotor depression. *Brain Research Bulletin*, 31:397–404, 1993.

Boison, D. Adenosine kinase, epilepsy and stroke: mechanisms and therapies. *TRENDS in Pharmacological Sciences*, 27:652–658, 2006.

Boison, D. The adenosine kinase hypothesis of epileptogenesis. *Progress in Neurobiology*, 84:249–262, 2007.

Chang, S.-Y., Kim, I., Marsh, M., Jang, D., Hwang, S.-C., Van Gompel, J., Goerss, S., Kimble, C., Bennet, K., Garris, P., Blaha, C., and Lee, K. Wireless fast-scan cyclic voltammetry to monitor adenosine in patients with essential tremor during deep brain stimulation. *Mayo Clin. Proc.*, 87:760–765, 2012.

Dale, N. and Frenguelli. Release of adenosine and ATP during ischemia and epilepsy. *Current Neuropharmacology*, 7:160–179, 2009.

Dale, N., Hatz, S., Tian, F., and Llaudet, E. Listening to the brain: microelectrode biosensors for neurochemicals. *TRENDS in Biotechnology*, 23:420–428, 2005.

During, M. and Spencer, D. Adenosine: A potential mediator of seizure arrest and postictal refractoriness. *Annals of Neurology*, 32:618–624, 1992.

Etherington, L., Patterson, G., Meechan, L., Boison, D., Irving, A., Dale, N., and Frenguelli, B. Astrocytic adenosine kinase regulates basal synaptic adenosine levels and seizure activity but not activity-dependent adenosine release in the hippocampus. *Neuropharmacology*, 56:429–437, 2009.

Fedele, D., Gouder, N., Guttinger, M., Gabernet, L., Scheurer, L., Rulicke, T., Crestani, F., and Boison, D. Astrogliosis in epilepsy leads to over expression of adenosine kinase, resulting in seizure aggravation. *Brain*, 128:2383–2395, 2005.

Florio, C., Rosati, A., Traversa, U., and Vertua, R. Inhibitory and excitatory effects of adenosine antagonists on spontaneous locmotor activity in mice. *Life Sciences*, 60:1477–1486, 1997.

Fredholm, B., Dunwiddie, T., Bergman, B., and Lindstrom, K. Levels of adenosine and adenine nucleotides in slices of rat hippocampus. *Brain Research*, 295:127–136, 1984.

Fredholm, B., Ijzerman, A., Jacobson, K., Klotz, K.-N., and Linden, J. International union of pharmacology. xxv. nomenclature and classification of adenosine receptors. *Pharmacological Reviews*, 53:527–552, 2001.

Huber, A., Padrun, V., Deglon, N., Aebischer, P., Mohler, H., and Boison, D. Grafts of adenosine-releasing cells suppress seizures in kindling epilepsy. *Pharmacology*, 98:7611–7616, 2001.

Ilie, A., Raimondo, J., and Akerman, C. Adenosine release during seizures attenuates gaba_a receptor-mediated depolarization. *J. Neurosci.*, 32:5321–5332, 2012.

Jefferys, J. and Haas, H. Synchronised bursting of CA1 hippocampal pyramidal cells in the absence of synaptic transmission. *Nature*, 300:448–450, 1982.

Kerr, M., Wall, M., and Richardson, M. Adenosine a1 receptor activation mediates the developmental shift at layer 5 pyramidal cell synapses and is a determinant of mature synaptic strength. *The Journal of Physiology*, 591:3371–3380, 2013.

Klyuch, B., Richardson, M., Dale, N., and Wall, M. The dynamics of single spike-evoked adenosine release in the cerebellum. *J. Physiol.*, 589:283–295, 2011.

Latini, S. and Pedata, F. Adenosine in the central nervous system: release mechanisms and extracellular concentrations. *Journal of Neurochemistry*, 79:463–484, 2001.

Llaudet, E., Botting, N., Crayston, J., and Dale, N. A three-enzyme microelectrode sensor for detecting purine release from central nervous system. *Biosensors and Bioelectronics*, 18:43–52, 2003.

Lopatar, J., Dale, N., and Frenguelli, B. Minor contribution of atp p2 receptors to electrically-evoked electrographic seizure activity in hippocampal slices: Evidence from purine biosensors and p2 receptor agonists and antagonists. *Neuropharmacology*, 61:25–34, 2011.

Masino, S., Li, T., Theofilas, P., Sandau, U., Ruskin, D., Fredholm, B., Geiger, J., Aronica, E., and Boison, D. A ketogenic diet suppresses seizures in mice through adenosine a_1 receptors. *The Journal of Clinical Investigation*, 121:2679–2683, 2011.

Mody, I., Lambert, J., and Heinemann, U. Low extracellular magnesium induces epileptiform activity and spreading depression in rat hippocampal slices. *J. Neurophysiol.*, 57:869–888, 1987.

Nagel, J., Schladebach, H., Koch, M., Schwienbacher, I., Muller, C., and Hauber, W. Effects of an adenosine a_2a receptor blockade in the nucleus accumbens on locomotion, feeding and prepulse inhibition in rats. *Synapse*, 49:279–286, 2003.

Nguyen, M., Lee, S., Ross, A., Ryals, M., Choudhry, V., and Venton, J. Characterization of spontaneous, transient adenosine release in the caudate-putamen and prefrontal cortex. *PLOS ONE*, 9:e87165, 2014.

Ralevic, V. and Burnstock, G. Receptors for purines and pyrimidines. *Pharmacological Reviews*, 50:413–492, 1998.

Shipp, S. Structure and function of the cerebral cortex. *Current Biology*, 17:R443–R449, 2007.

Swamy, B. and Venton, B. Subsecond detection of physiological adenosine concentrations using fast-scan cyclic voltammetry. *Anal. Chem.*, 79:744–750, 2007.

Thomas, M., Covington, J., and Wall, M. A chamber for the perfusion of in vitro tissue with multiple solutions. *J. Neurophysiol.*, 110:269–277, 2013.

Thomas, M., Covington, J., Richardson, M., Turner, M., and Wall, M. High-resolution recording of neural activity by transforming intrinsic optical signals. *J. Neurosci*, In Review, 2015.

Van Gompel, J., Bower, M., Worrell, G., Stead, M., Chang, S.-Y., Goerss, S., Kim, I., Bennet, K., Meyer, F., Marsh, W., Blaha, C., and Lee, K. Increased cortical extracellular adenosine correlates with seizure termination. *Epilepsia*, 55:233–244, 2014.

Wall, M. and Dale, N. Auto-inhibition of rat parallel fibre-purkinje cell synapses by activity-dependent adenosine release. *J. Physiol.*, 581:553–565, 2007.

Wall, M. and Dale, N. Activity-dependent release of adenosine: A critical re-evaluation of mechanism. *Curr. Neuropharmacol.*, 6:329–337, 2008.

Wall, M. and Richardson, M. Localized adenosine signaling provides fine-tuned negative feedback over a wide dynamic range of neocortical network activities. *J. Neurophysiol.*, 113:871–882, 2015.

Winn, H., Welsh, J., Rubio, R., and Berne, R. Changes in brain adenosine during bicuculine-induced seizures in rats. *Circ. Res.*, 47:568–577, 1980.

Yoon, K.-W. and Rothman, S. Adenosine inhibits excitatory but not inhibitory synaptic transmission in the hippocampus. *J. Neurosci.*, 11:1375–1380, 1991.

Chapter 5

Conclusions

Understanding the brain in both health and disease is of fundamental scientific interest and of great practical importance. The acute neural tissue slice is a widely used experimental preparation, facilitating treatments and measurements not practical *in vivo* while preserving a largely connected network representative of the true *in vivo* structure. In this thesis two methods that further the ability to study the acute neural tissue slice have been presented, followed by an application of one of the methods to the study of seizure evoked adenosine release.

In Chapter 2 a novel chamber was presented and characterised that allows extended areas of acute tissue slice to be exposed, in isolation, to changes in ionic conditions or pharmacological manipulation whilst preserving the ability to record from the entire surface of the tissue. Such spatial targeting had previously only been achieved at the expense of access to the tissue for recording. The chamber facilitates an entirely *in vitro* model of focal seizure activity.

Changes in the intrinsic optical properties of brain tissue correlated with neuronal activity are known to occur both *in vivo* and *in vitro*. These changes are used as the basis of non-invasive approaches to the recording of neuronal activity. The use of IOSs as a proxy for neuronal activity has many advantages; they require no mechanical, chemical or genetic interference with the tissue and are not limited by recording rate or duration. The temporal dynamics of the IOS are, however, slow and so do not directly correspond to the underlying network dynamics. In Chapter 3 we characterised the intrinsic optical signal (IOS) that persists *in vitro* and derived

a transformation that converts the slow temporal dynamics of the IOS to a form that accurately reflects the underlying network dynamics, thereby mitigating the primary disadvantage of the use of IOSs as a method to record neuronal dynamics, allowing their advantages to be fully exploited.

Adenosine is a potent neuromodulator that plays an important role both in physiological processes and in neuroprotection during pathological events. Adenosine largely provides negative feedback in response to neuronal activity and it is, therefore, of fundamental interest in epilepsy. Adenosine is known to be released in response to seizure activity and is implicated in seizure termination. Dis-regulation of adenosine may be involved in epileptogenesis and there are promising applications of adenosine therapeutically. In Chapter 4 we characterised the spatio-temporal dynamics of adenosine in response to seizure activity *in vitro*. The temporal dynamics of adenosine release in response to seizure activity had previously been investigated, however, the spatial dynamics had not been readily accessible because of the lack of a suitable recording tool for the network activity, able to record over sufficiently large areas of tissue for sufficiently long periods. Recording of the IOS in combination with the transformation presented in Chapter 3 rendered this regime accessible and so facilitated the study. In this work we identified two qualitatively different forms for adenosine release, observed a significant difference in adenosine release between layers of the neocortex, resolved the spatial spread of adenosine relative to the associated network activity and determined that a component of seizure evoked adenosine release is dependent on equilibritive nucleoside transporters (ENTs).

Finally, in the appendices of this thesis, four studies are presented that investigate the potential for Field Asymmetric Ion Mobility Spectrometry (FAIMS) in medical diagnosis. FAIMS is a highly sensitive tool for chemical detection, originally applied to the detection of chemical warfare agents. FAIMS was thought to have significant potential in medical diagnosis, however, this had never been explored due to the challenge of the analysis of FAIMS spectra from complex biological mixtures. Appendix B presents a first proof of principle of the effectiveness of FAIMS at discriminating between complex biological mixtures. Following this we go on to present proof of principle of the potential of FAIMS in medical diagnosis (Ap-

pendix C), obtaining prognostic information (Appendix D) and as a screening tool (Appendix E). The approach presented here for the analysis of FAIMS spectra is almost certainly not optimal, however, the proof of principle will hopefully stimulate further development.

Appendix A

FAIMS analysis introduction

Abstract

Field Asymmetric Ion Mobility Spectrometry (FAIMS) is a highly sensitive tool for chemical detection, originally applied to the detection of chemical warfare agents. FAIMS is able to detect a broad range of chemicals at concentrations below one part per billion. As such, FAIMS was thought to have significant potential in medical diagnosis, however, this had never been explored due to the challenge of the analysis of FAIMS spectra from complex biological mixtures. In the following section an analysis approach is presented that allows the FAIMS spectra of complex biological mixtures to be distinguished. In the following appendices the approach is then applied to identify inflammatory bowel diseases, patients at risk of high gastrointestinal toxicity in response to radical pelvic radiotherapy and patients with colorectal cancer.

A.1 Ion mobility spectrometry

Ion mobility spectrometry (IMS) discriminates between ions on the basis of their transport properties when moving through a medium under the influence of an electric field. Conventional IMS refers to methods dependent on transport properties that can be measured using a constant electric field. Differential IMS refers to methods that rely on transport properties that are dependent on the applied electric field (Shvartsburg, 2009).

When exposed to an electric field in a medium, ions rapidly accelerate to a terminal (drift) velocity, $\mathbf{v}$. The drift velocity is proportional to the applied electric field, $\mathbf{E}$: $\mathbf{v} = K\mathbf{E}$, where K is the ion mobility. The mobility of an ion depends on its physical characteristics, mobility can therefore be used to distinguish ions.

In a conventional IMS system molecules are ionised and then driven through a medium filled drift tube by a constant electric field. The ions can be separated on the basis of the time taken for them to traverse the drift tube.

Differential IMS depends on the fact that ion mobility usually varies as a function of the applied electric field. Ions are then separated on the basis of differences in this voltage dependence by exposing them to a time dependent electric field.

A.2 Principles of FAIMS

Field asymmetric ion mobility spectrometry (FAIMS) is a type of differential ion mobility spectrometry. Molecules are ionised and then carried between two parallel plates towards a detector by a carrier gas. A time dependent electric field, $\mathbf{E}(t)$, with an asymmetric waveform is applied to the plates, such that the ions experience an electric field perpendicular to the direction of carrier gas flow. If an ion touches one of the plates it is likely to be neutralised. If an ion traverses the space between the two plates (the filter gap) without touching either plate it is detected (Fig. A.1).

The applied electric field consists of an asymmetric waveform, $f(t)$, with variable dispersion field amplitude, $0 \leq S \leq 1$, and a compensation voltage, C: $E(t) = Sf(t) + C$. The moments of $f(t)$ are defined as:

$$\langle f^n \rangle \equiv \frac{1}{T} \int_0^T f^n(t) dt \tag{A.1}$$

where T is the period of the waveform. The waveform is constructed such that $\langle f \rangle = 0$, but so at least some odd moments are non-zero.

If ion mobility were independent of electric field all ions would traverse the filter gap (other than as a result of diffusion) and be detected when the compensation voltage was set to zero. The field dependence of the ion mobility results, however,

Figure A.1: Schematic of a FAIMS system. From Owlstone Inc., Cambridge. The figure has been redacted from this version to avoid copyright infringement.

in a net drift of ions parallel to the applied electric field. Ions are only detected when the compensation voltage corrects for this drift, resulting in ions traversing the filter gap without coming in to contact with either plate.

The output from a FAIMS system consists of two matrices, one corresponding to positive ions and one corresponding to negative ions. The matrices consist of ion counts at different combinations of compensation voltage and dispersion field, for example see Fig. A.2.

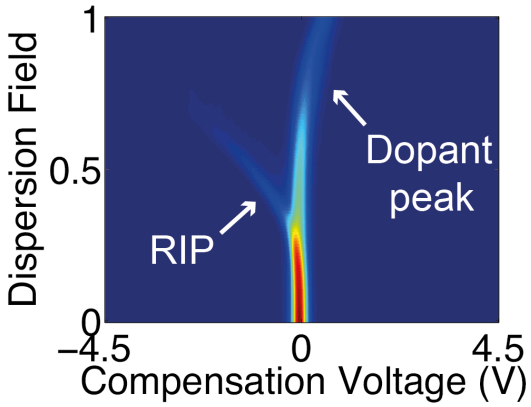

Figure A.2: An example positive ion FAIMS spectrum of air contaminated with a single dopant (acetone). The residual ion peak (RIP) corresponds to hydronium ions (O^- in the case of the negative ion matrix) produced from the beta decay of ^{63}Ni, to ionise the analytes.

A.3 Clinical potential for FAIMS

Recent advances have led to the development of microchip based FAIMS systems (Shvartsburg et al., 2009; Wilks et al., 2012). This has resulted in devices that have high sensitivity (< 0.1 parts per billion (ppb) for many low molecular weight compounds (Shvartsburg et al., 2009)) whilst also being compact (Fig. A.3) and robust, with low power consumption and no moving parts (Boyle, 2006).

These properties make microchip based FAIMS systems ideal for a number of detection and screening applications. These devices have been widely adopted by defence and security agencies for the detection of explosive and chemical detection (Boyle, 2006). FAIMS is also thought to have significant potential in clinical diagnosis and screening (Arasardnam et al., 2011). The challenges associated with the analysis of the FAIMS spectra of complex biological mixtures are, however, far greater than those associated with, for example, the detection of chemical warfare agents contaminating air. As a result, the exploitation of FAIMS for clinical applications has been slow.

Figure A.3: The Owlstone Lonestar, a self contained FAIMS system. From Owlstone Inc., Cambridge. The figure has been redacted from this version to avoid copyright infringement.

A.4 The challenge of identifying clinically relevant information in FAIMS spectra of complex biological mixtures

Algorithmic detection of the contamination of air with a single dopant, such as a chemical warfare agent, is readily implemented. Analysis of uncontaminated air shows a single peak. This is the residual ion peak (RIP) corresponding to hydronium ions in the case of the positive ion matrix and O^- ions in the case of the negative ion matrix. These ions are produced by the beta decay of ^{63}Ni to ionise analytes. When a contaminant is added to the air an additional peak is detected. Figure A.4 shows the FAIMS spectra and representative cross-sections for air (top) and for air with a single contaminant, such as the neurotoxin sarin (bottom). Automatic detection of such contamination is simply implemented by imposing thresholds at the locations that correspond to contaminants of interest.

Unlike the FAIMS spectra of air and a single dopant, the FAIMS spectra

of complex mixtures consist of multiple overlapping peaks, for example Figure A.5 shows the positive ion FAIMS spectra of the headspace of urine from a healthy individual and that from an individual with colorectal cancer (CRC). It was unknown whether such spectra contained diagnostic information. They would almost certainly show variability not related to disease state, and even if they did contain diagnostic information, it may not simply be as the presence or absence of a specific peak. It would, however, be valuable to explore the the possibility of using FAIMS to screen for CRC, because if it were possible the analysis of urine using FAIMS would be a significant improvement on the currently available screening tools (these potential advantages are discussed in Appendix E.

The methods used to detect contamination of air with chemical warfare agents were clearly unsuitable for the investigation of the possibility of discriminating between the FAIMS spectra of similar biological samples. The direct application of unsupervised machine learning techniques, such as principal component analysis, proved unsuccessful. Approaches for supervised machine learning could not be directly applied because the number of elements in the FAIMS spectra ($\sim$51 000) was far greater than the number of patients in the trials ($\sim$100). Any training set was likely to contain dimensions on which the groups could be discriminated correctly, however, this was likely to be a result of noise. The application of the resulting classification criterion to a test set was likely to yield re-classification no better than that expected from random re-classification.

A.5 Analysis approach

To allow the effective application of supervised machine learning techniques, an approach to reduce the number of elements associated with each patient was required. Both theoretical and empirical analyses have shown that the profiles of FAIMS spectra at constant dispersion fields are made up of a number of localised peaks (Fig. A.6A (Krylov et al., 2007; Buryakov, 2005). The nature of this structure suggested that a basis set of similar functions may be a more natural choice and may make diagnostic information easier to identify.

A wavelet, ψ, is a function consisting of an isolated oscillation, such as that

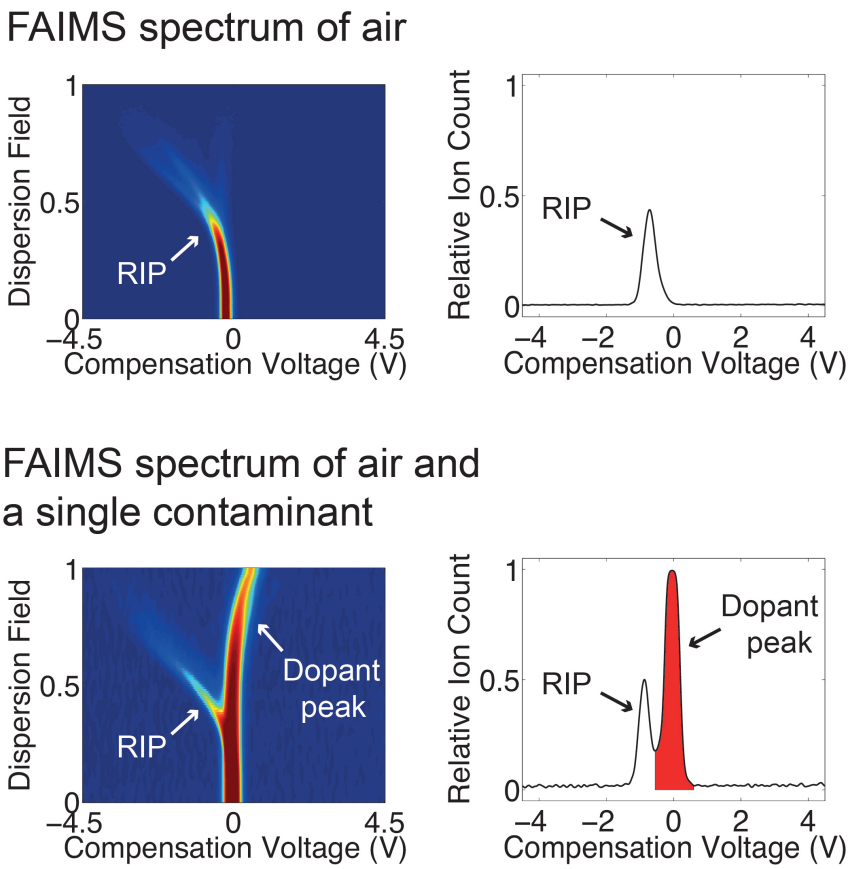

Figure A.4: An example positive ion FAIMS spectrum of air (top left) showing the residual ion peak (RIP) and an example cross-section at constant dispersion field (top right) and an example positive ion FAIMS spectrum of air contaminated with a single dopant (acetone, bottom left) and an example cross-section at constant dispersion field (bottom right).

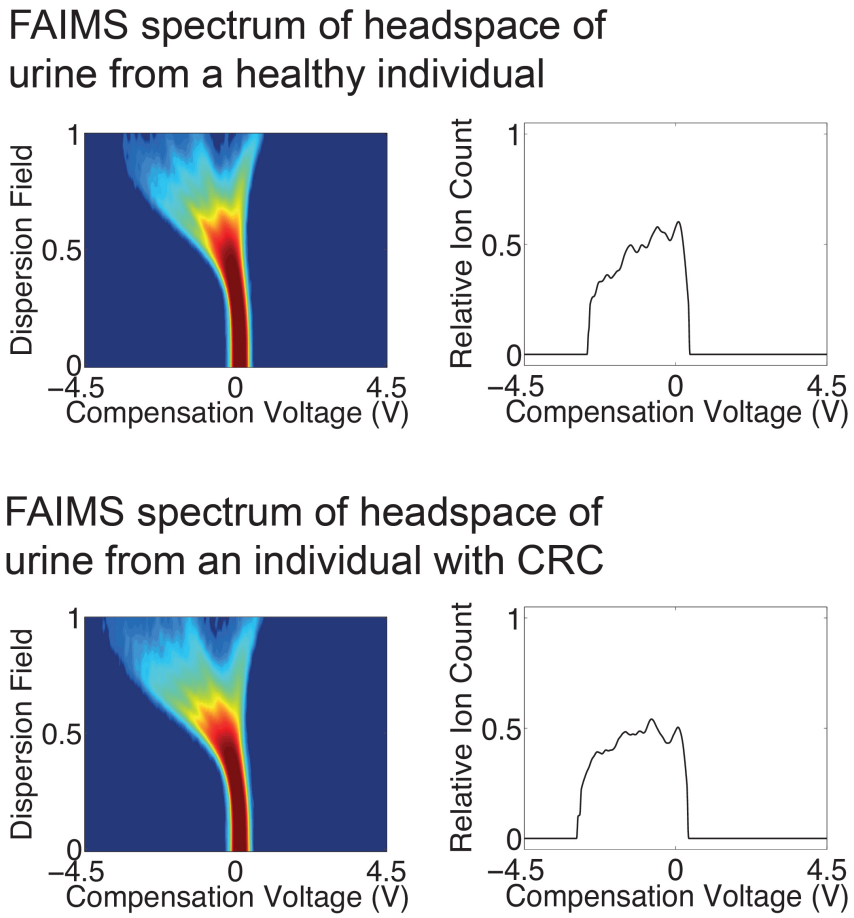

Figure A.5: An example positive ion FAIMS spectrum of the headspace of urine from a healthy individual (top left) and an example cross-section at constant dispersion field (top right) and an example positive ion FAIMS spectrum of the headspace of urine from an individual with colorectal cancer (bottom left) and an example cross-section at constant dispersion field (bottom right).

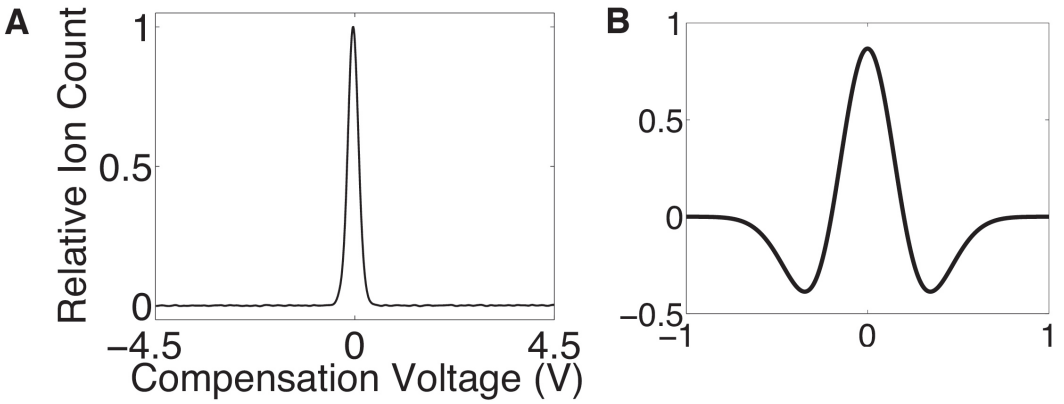

Figure A.6: (A) An example cross section through a FAIMS peak at constant dispersion field. (B) An example wavelet.

shown in Fig. A.6B that has zero mean and L^2 norm one. By translating and dilating ψ (Eqn. A.2), a basis set can be generated. A basis set of this form seemed natural for FAIMS data.

$$\psi^{a,b}(x) = \mid a \mid^{-1/2} \psi\left(\frac{x-b}{a}\right) \tag{A.2}$$

An intuition driven approach based on wavelet transforming the FAIMS spectra was implemented as follows. To test the validity of the approach, for each data set the process was applied to a randomly selected training set and the resulting classification matrix was tested on the remaining data and compared to the true classification:

1. Firstly, the rows of the positive and negative ion count matrices were concatenated to form a one dimensional vector corresponding to each matrix. These vectors were then concatenated. This gave a single vector containing every element from the two output matrices. This re-arrangement was obviously invertible and so preserved the information content in the spectra whilst producing a one dimensional vector to which a wavelet transform could be carried out.

2. The vector was then wavelet transformed using a multi-level discrete wavelet transform using a Daubechies D4 wavelet. This was also an invertible operation and so the information content of the original spectra was still preserved at this stage. However, intuition suggested that the information content relating

to the ion peaks would now be compressed on to fewer dimensions.

3. Dimensions in the transform space suitable for discrimination were then identified. Thresholds were set for the between class scatter: $(\sigma_\mu)^2/(\Sigma\sigma)^2$ and the within class scatter: $(\Sigma\sigma)^2$. In both cases the thresholds were used as a lower bounds. Large between class scatter was clearly desirable in a dimension used for discrimination - the form used for this compensating for the within class scatter. The second threshold, the minimum imposed on the within class scatter was required to prevent dimensions with small values and correspondingly narrow distributions giving anomalously large values for the between class scatter. Dimensions meeting the criteria for both thresholds were included in an output vector.

4. The number of dimensions identified for discrimination was compared to a final threshold of approximately 200. If the number of dimensions identified exceeded this threshold, the data was not reclassified and the result was counted as incorrect. This avoided the computational demand associated with applying Fisher Discriminant Analysis to a large number of dimensions. The threshold was larger than the number of patients in any of the trials and so a preclassified machine learning technique applied to this many variables was not likely to identify a classification matrix that would yield accurate reclassification. Assuming that the reclassification would have been incorrect was only likely to modify the result that would otherwise have been the $\sim 50\%$ expected for random reclassification.

5. Fisher Discriminant Analysis (FDA) (Fisher, 1936) was applied to the output vectors. FDA is a linear, preclassified, machine learning technique. The approach identifies a projection matrix that maximises the separation of the groups.

   The dimensions identified for discrimination from the training set were also selected for each sample in the test set. The projection matrix identified by the FDA was then applied to these vectors corresponding to each sample and the result was compared to the true classification. The fraction of success-

ful reclassifications of test sets was then compared with that expected from random reclassification.

A.6 Testing of analysis process

The effectiveness of the analysis process was investigated by applying it to the data set discussed in Appendix B. Briefly, urine samples were obtained from eight patients who underwent partial bowel cleansing prior to flexible sigmoidoscopy and from eight patients who underwent total bowel cleansing prior to colonoscopy. The urine samples were heated and the resulting headspaces were characterised using FAIMS.

For each group, seven randomly selected samples were used as the training set and the remaining sample from each group was reclassified. This process was repeated ten times for each combination of the input parameters, the within class scatter threshold and the between class scatter threshold. The percentage reclassification for each set of these parameters was then calculated. Fig. A.7A shows the result of this process. A robust region in parameter space was identified that yielded reclassification significantly better than that expected from random reclassification. A 100 element region, spanning 10% of the parameter range in each dimension yielded a mean correct reclassification of 84.2 $\pm$ 1.2 %.

To confirm the validity of this result, the same process was applied after the data had been randomised such that each of the two new groups consisted of four patients from each treatment group. Fig. A.7B shows the result of this process. No robust region in the parameter space was found where the reclassification was significantly better than that expected from random reclassification. Equally, the distribution of reclassification success did not extend beyond 70 %, unlike for the correctly grouped data for which it extended to 100 %.

These results indicate that the proposed analysis process can identify features specific to a group and accurately reclassify spectra on the basis of these features, and does not give spurious results, overestimating the success of the reclassification.

The wavelet transform step was included in the analysis process on the basis of intuition. Its effect on the process was investigated empirically using the same

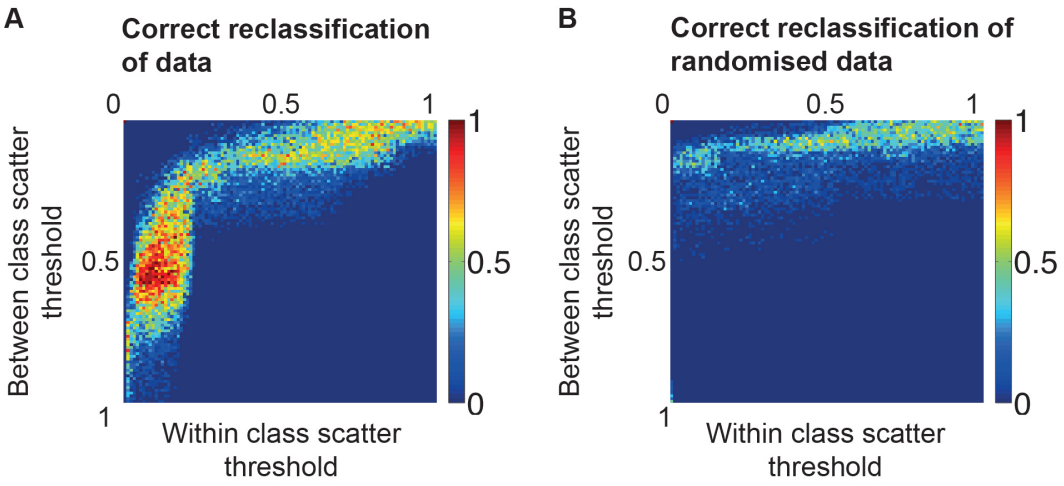

Figure A.7: Comparison of reclassification success for the original data sets and for the data relabelled to give two equivalent groups. (A) Result of the application of the analysis process to the original data as a function of the input parameters, showing a robust region where successful reclassification significantly exceeded that expected from random reclassification. (B) Result of the application of the analysis process, as a function of the input parameters, to the data relabelled such that each new group contained half of each of the original members of each group (no spectrum was duplicated in each new group), showing significantly fewer correct reclassifications than that from reclassification of the correctly labelled data.

data as discussed above and in Appendix B. The analysis process was applied to the data both with the wavelet transform step included and with it omitted. The process without the wavelet transform step did not identify a significant robust region that yielded successful reclassification and the distribution of reclassification success was truncated at lower success fractions than for the complete process (Fig A.8.

This suggests that the wavelet transform acts as expected to compress the information content of the FAIMS spectra and that this is a beneficial step in the process presented here.

A.7 Pilot studies

The application of this analysis process to the FAIMS spectra of these samples (discussed fully in Appendix B) demonstrated that the health of the gut affects the composition of urine, that at least some of these differences can be detected with FAIMS of the headspace of the urine and that the spectra can be separated better than would be expected by random reclassification using the analysis process presented here. This proof of principle was a significant step towards exploiting the advantages of FAIMS in clinical diagnosis. The separation of the specific groups,

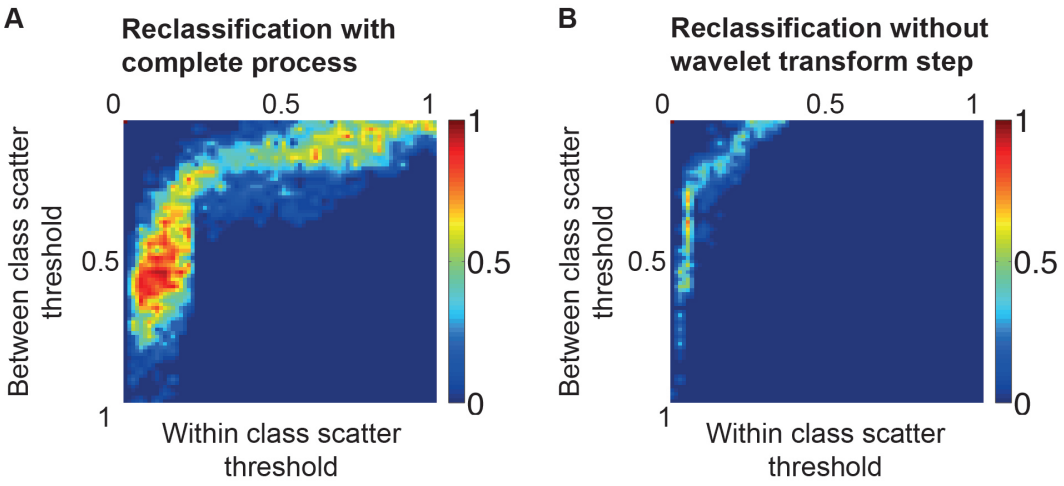

Figure A.8: The wavelet transform step increases accurate reclassification. (A) Correct reclassification of the test sets as a function of the input parameters for the analysis process including the wavelet transform step, showing a robust region where successful reclassification significantly exceeds that expected from random reclassification. (B) Correct reclassification of the test sets as a function of the input parameters without the wavelet transform step showing significantly less accurate reclassification when the wavelet transform step is not included in the analysis.

however, had no clinical value, the difference between the groups was the intervention. To investigate the application of FAIMS to clinically relevant problems a further three pilot studies were carried out. The first investigated the possibility of diagnosing inflammatory bowel disease from urine samples; the second investigated the possibility of extracting prognostic information from faecal samples from patients due to undergo radical pelvic radiotherapy and the third investigated the possibility of screening for colorectal cancer from urine samples. These studies are presented in the following appendices.

Bibliography

R.P. Arasardnam, C.U. Nwokolo, K.D. Bardhan, and J.A. Covington. Electronic nose versus canine nose: clash of the titans. *Gut*, 60:1768, 2011.

B. Boyle. Owlstone Nanotech. Technical report, Owlstone Nanotech Inc, 03 2006.

I.A. Buryakov. Solution of the equation of continuity for ions moving in a gas under the action of a periodic asymmetric alternating waveform. *Technical Physics Letters*, 32:67–69, 2005.

R.A. Fisher. The use of multiple measurements in taxonomic problems. *Annals of Eugenics*, 7:179–188, 1936.

E.V. Krylov, E.G. Nazaroy, and R.A. Miller. Differential mobility spectrometer: Model of operation. *International Journal of Mass Spectrometry*, 266:76–85, 2007.

A.A. Shvartsburg. *Differential Ion Mobility Spectrometry.* CRC Press, 2009.

A.A. Shvartsburg, R.D. Smith, A. Wilks, A. Koehl, D. Ruiz-Alonso, and B. Boyle. Ultrafast differntial ion mobility spectrometry at extreme electric fields in multi-channel microchips. *Anal. Chem.*, 81:6489–6495, 2009.

A. Wilks, M. Hart, A. Koehl, J. Somerville, B. Boyle, and D. Ruiz-Alonso. Characterization of a miniature, ultra-high-field, ion mobility spectrometer. *Int. J. Ion. Mobil. Spec*, 15:199–222, 2012.

Appendix B

Evaluation of gut bacterial populations using an electronic e-nose and field asymmetric ion mobility spectrometry: further insights into fermentonomics

This Appendix contains a paper presenting an initial proof of principle of the effectiveness of Field Asymmetric Ion Mobility Spectrometry (FAIMS) at discriminating between complex biological mixtures, specifically urine samples from patients after partial and total bowel cleansing prior to flexible sigmoidoscopy and colonoscopy respectively. I developed the analysis procedure for the FAIMS spectra, wrote the code to implement it and applied it to the data. The trial was designed and otherwise implemented by the other authors.

The full paper has been redacted from this version to avoid copyright infringement.

Appendix C

A novel tool for noninvasive diagnosis and tracking of patients with inflammatory bowel disease

This Appendix contains a paper presenting a proof of principle of the effectiveness of FAIMS at analysing urine samples to discriminate between disease states, specifically ulcerative colitis and Crohn's disease both in remission and flare. I developed the analysis procedure for the FAIMS spectra, wrote the code to implement it and applied it to the data. The trial was designed and otherwise implemented by the other authors.

The full paper has been redacted from this version to avoid copyright infringement.

Appendix D

The detection of patients at risk of gastrointestinal toxicity during pelvic radiotherapy by electronic nose and FAIMS: A pilot study

This Appendix contains a paper investigating the possibility of using FAIMS to analyse urine samples to provide prognostic information, specifically the reaction to radical pelvic radiotherapy. I developed the analysis procedure for the FAIMS spectra, wrote the code to implement it and applied it to the data. The trial was designed and otherwise implemented by the other authors.

Sensors **2012**, *12*, 13002-13018; doi:10.3390/s121013002

OPEN ACCESS

sensors

ISSN 1424-8220

www.mdpi.com/journal/sensors

Article

The Detection of Patients at Risk of Gastrointestinal Toxicity during Pelvic Radiotherapy by Electronic Nose and FAIMS: A Pilot Study

James A. Covington [1,*], Linda Wedlake [2], Jervoise Andreyev [2], Nathalie Ouaret [1], Matthew G. Thomas [1,3], Chuka U. Nwokolo [4], Karna D. Bardhan [5,6] and Ramesh P. Arasaradnam [4,6]

1 School of Engineering, University of Warwick, Coventry CV4 7AL, UK; E-Mails: N.Ouaret@warwick.ac.uk (N.O.); M.G.Thomas@warwick.ac.uk (M.G.T.)

2 Department of Nutrition and Dietetics and the GI Unit, The Royal Marsden NHS Foundation Trust, Fulham Road, London SW3 6JJ, UK; E-Mails: box46@statacom.net (L.W.); J@andreyev.demon.co.uk (J.A.); R.Arasaradnam@warwick.ac.uk (R.P.A.)

3 MOAC Doctoral Training Centre, University of Warwick, Coventry CV4 7AL, UK

4 University Hospital Coventry & Warwickshire, Coventry CV2 2DX, UK; E-Mail: chuka.nwokolo@uhcw.nhs.uk

5 Department of Gastroenterology, Rotherham General Hospital, Rotherham S60 2UD, UK; E-Mail: bardhan.sec@rothgen.nhs.uk

6 Clinical Sciences Research Institute, University of Warwick, Coventry CV2 2DX, UK

* Author to whom correspondence should be addressed; E-Mail: J.A.Covington@warwick.ac.uk; Tel.: +44-24-7657-4494; Fax: +44-24-7641-8922.

Received: 21 July 2012; in revised form: 10 September 2012 / Accepted: 10 September 2012 / Published: 26 September 2012

Abstract: It is well known that the electronic nose can be used to identify differences between human health and disease for a range of disorders. We present a pilot study to investigate if the electronic nose and a newer technology, FAIMS (Field Asymmetric Ion Mobility Spectrometry), can be used to identify and help inform the treatment pathway for patients receiving pelvic radiotherapy, which frequently causes gastrointestinal side-effects, severe in some. From a larger group, 23 radiotherapy patients were selected where half had the highest levels of toxicity and the others the lowest. Stool samples were obtained before and four weeks after radiotherapy and the volatiles and gases emitted analysed by both methods; these chemicals are products of fermentation caused by gut microflora. Principal

component analysis of the electronic nose data and wavelet transform followed by Fisher discriminant analysis of FAIMS data indicated that it was possible to separate patients after treatment by their toxicity levels. More interestingly, differences were also identified in their pre-treatment samples. We believe these patterns arise from differences in gut microflora where some combinations of bacteria result to give this olfactory signature. In the future our approach may result in a technique that will help identify patients at "high risk" even before radiation treatment is started.

Keywords: electronic nose; FAIMS; fermentome; gastrointestinal toxicity; gut permeability; pelvic radiotherapy

1. Introduction

The electronic nose (e-nose) was first conceived in the early 1980s [1] and has undergone continuous refinement ever since. Developed as a means of replicating the biological olfactory system, it does not identify specific chemicals within a complex mixture (as possible with, for example, gas chromatography and/or mass spectrometry—GCMS), but analyses the sample as a whole to create an "olfactory signature". Such instruments have been applied widely in commerce and research, including for food and beverage quality, perfumes and process control [2,3]. Of increasing importance has been the application of this technology to the medical domain. The possibility of using the electronic nose for the identification and monitoring of disease has shown considerable promise. The detection of gas phase bio-markers from human biological output, be it breath, sweat, blood, urine or faecal matter, has been shown to identify a disease state. E-nose technology is close to real-time, can be operated without special gases, at room temperature and pressure, is non-invasive and could be produced at a financially acceptable cost for the medical profession. The range of diseases that e-nose technology has been applied to is considerable, ranging from lung cancer, brain cancer and melanoma to inflammatory bowel disease and even schizophrenia [4–9].

A more recent technological development is that of field-asymmetric ion mobility spectrometry (FAIMS) for monitoring complex odours. As with the electronic nose, FAIMS can be used for the real-time analysis of complex chemical components, looking at the total chemical composition of a sample. Such instruments use differences in the mobility of ionised molecules in high electric fields to provide a "mobility signature" of a complex sample. This mobility signature is in many ways comparable to the olfactory signature created by the array of chemical sensors in the e-nose. FAIMS instruments have found widespread use within the security sector [10], as they can detect large volatile molecules at extremely low concentration (e.g., explosives), but it has not as yet been used extensively within the medical field.

One medical area yet to receive attention by either e-nose or FAIMS technology is that of pelvic cancer patients, undergoing radiotherapy. The pelvis is a confined area bounded by bone and thick muscle, leaving only a fairly small central cavity. This is packed (from front to back) with the bladder, ovaries, uterus/cervix, the rectum, sigmoid colon (the lower part of the large bowel) and a variable number of small bowel loops. As a result, pelvic irradiation for a tumour affecting an organ inevitably

injures the others. Almost all patients experience changes in bowel habits during their five to seven week course of radiotherapy. Up to 90% of patients report abnormal gastrointestinal symptoms of varying severity, termed "pelvic radiation disease" [11,12]. A wealth of data now supports the view that acute radiotherapy-induced damage is characterised by inflammatory processes. Maximum damage to the gastrointestinal mucosa occurs about two weeks into treatment [13]. However, whilst acute mucosal damage may then improve, the prevalence of moderate or severe chronic side effects can be as high as 50% [13,14]. Despite increasingly sophisticated radiotherapy planning and delivery, those patients who are at most risk of severe late problems cannot be predicted using normal medical measures. There is evidence that this high level of susceptibility may be due to differences in the composition and treatment-induced change of their gut bacterial populations [15,16]. Directly measuring the composition of these populations is incredibly difficult due to their location and huge variation in bacterial types, but we believe information in regard to its overall composition could be attained by looking at the gaseous emissions of bacteria within faecal samples. Thus, in an attempt to evaluate if it is possible to identify these "high-risk" patients, we have undertaken a pilot study to evaluate if either a traditional e-nose or a FAIMS instrument can identify differences in faecal gas emissions. Here we have taken samples before and after treatment from patients who have had a high toxicity and low toxicity response after treatment to investigate if there is a difference in these gas emissions. If feasible, it may be possible in the future to warn the clinician of patients that are likely to become seriously ill, thereby indicating who requires closer monitoring and/or possibly to be considered for an alternative treatment pathway. Such a patient-tailored approach offers a potential route towards minimising morbidity associated with this treatment.

2. Material and Methods

To undertake this study an in-house traditional electronic nose and a commercial FAIMS instrument has been used to analyse faecal samples from pelvic radiation patients.

2.1. Electronic Nose

Electronic noses are instruments that attempt to replicate the biological olfactory system, by investigating gas phase samples as a whole, instead of identifying specific chemicals within a complex gas mixture. In an electronic nose, the air above the sample (or headspace) is drawn into the electronic nose and is passed across an array of chemical sensors. The size of the array varies, but most are between six and 32 sensors. Each sensor of the array is broadly tuned to a chemical group, with overlapping sensitivity, but importantly, is different in some way from the rest of the array. As each sensor is dissimilar, the interaction between the sensor and the complex sample is unique within the array. Thus, an olfactory signature of this complex odour can be created. In most applications, some form of pattern recognition algorithm is applied to learn this olfactory signature and, when presented with the same profile, is able to recognize the odour.

The electronic nose used in this study is an in-house instrument developed at Warwick University. It contains an array of six metal oxide based sensors (high temperature resistive sensors), as well as six electrochemical sensors, a pellister (catalytic sensor), and an NDIR sensor (optical, to monitor CO_2). A list of sensors and manufacturers is given in Table 1. These different sensor technologies

were chosen for two reasons. First, it provides considerable diversity to the information that can be gathered from the array. Second, the sensors were selected to be broadly tuned to gases and vapours that we believe may be important products in the normal metabolic activity of the gut.

Table 1. Sensors deployed within the electronic nose, with descriptions. Number is brackets is sensor number within the instrument.

Metal Oxide Sensors (Figaro Jpn)	Electrochemical Sensors (Alphasense/Sensors Direct, UK)	Others (Alphasense, UK)
TGS813—Low pressure gas (1)	NO_2-A1—Nitrogen dioxide (8)	IRC-A1—Carbon dioxide (7)
TGS821—Hydrogen (2)	NO-A1—Nitrous oxide (9)	CH-A3—Flammable gases (13)
TGS822—Organic solvents (3)	H_2S-A1—Hydrogen sulphide (10)	
TGS824—Ammonia (4)	CO-A1—Carbon monoxide (11)	
TGS825—Hydrogen sulphide (5)	SO_2-A1—Sulphur dioxide (12)	
TGS880—Volatile vapours (6)	S+H_2—Hydrogen (14)	

Due to the different types of sensors deployed within the instrument, it is useful to transduce each of the sensor outputs into a common form—in this case voltage. The six metal-oxide sensors were driven with a constant current source (100 μA) and the voltage across the sensor then amplified and monitored. The electrochemical sensors were attained with transmitter boards, containing a potentiostat and drive circuit to give a 4–20 mA output. This current was converted to a 0–10 V signal (note that the boards and sensors were calibrated for the gas concentration operating ranges defined by the manufacturer). The NDIR was also supplied with a transmitter board, giving a 4–20 mA output, which again was converted to 0–10 V. Finally, for the pellister a bridge circuit was manufactured with a differential output stage. Here the offset was trimmed to be zero in laboratory air and the differential output stage gain set to 20. The output voltage of all these sensors was measured using two National Instruments (USA) USB-6009 boards. The electronic nose was also fitted with a temperature and humidity sensor (Sensirion SHT-15, Staefa, Switzerland) to monitor the input sample. In addition to the sensors, the electronic nose was fitted with a pump with flow sensors, chamber temperature control, valves and dedicated software interface (written in LabVIEW 8.6, National Instruments, Woburn, MA, USA).

2.2. FAIMS Instrumentation

For this study a commercial FAIMS instrument was used, specifically a Lonestar (Owlstone, UK). FAIMS is a fairly recent technological development whereby separation occurs due to ionised molecules having different mobilities in high and low electric fields. Such instruments have a number of advantages, for example, they can use scrubbed air as the carrier gas, operate at room pressure (or above), and so no vacuum pump is required.

In a FAIMS instrument the gas phase chemical input is first ionised (in our case using a Ni-63 source). These ionised molecules then enter an oscillating high electric field, whereby molecules zig-zag between two plates to which this electric field is applied. This waveform is “asymmetric”, thus a high positive voltage is applied for a short period of time and a low negative voltage is applied for a longer period. However, the integral of the voltage over a time period is zero. The waveform is stepped through a

series of magnitudes and is called the "dispersion field" (DF). Below 200 V/cm the ions, on average, simply move back and forth between the plates but do not drift preferentially towards either one. At higher voltages in contrast, for example 5,000 V/cm or more, some ions within the complex mixture, on average move more in the direction of one plate. If an ion contacts the plate it loses its charge and is not detected as it exits the plates. Thus a balancing voltage (known as the "Compensation Voltage" or "CV") is applied, which counteracts this drift. This compensation voltage can be set whereby only the drift from a specific ion is compensated for and will be detected. Thus by sweeping through a range of dispersion fields and compensation voltages a complex mixture of gases can be separated by their differences in mobility in high and low electric fields [17]. Figure 1 gives an example of the applied waveform for FAIMS and the separation of ions by the field plates.

Figure 1. (**a**) Asymmetric waveform applied in FAIMS and (**b**) ions being separated by an asymmetric waveform.

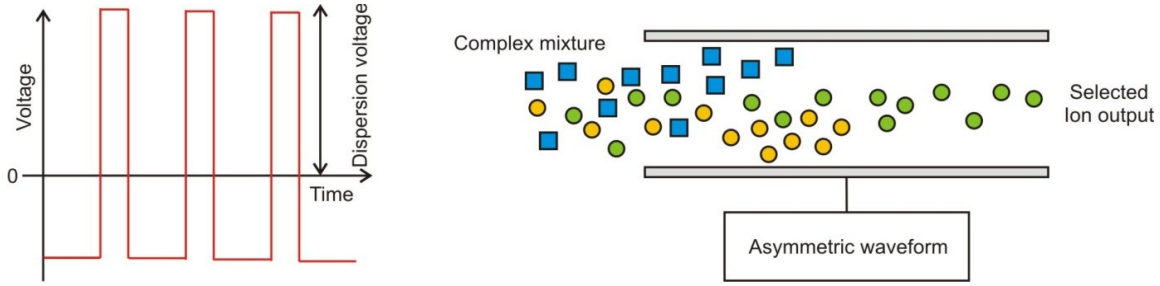

(**a**) (**b**)

2.3. Patients

Patients were recruited from a larger cohort undergoing long course (radical) radiotherapy with different end points and will be reported independently. Two groups were selected and stool samples from these patients were used for this study. The only criterion for inclusion was the degree of gastrointestinal disturbance between baseline and after four weeks of radiotherapy. This was measured by the IBDQ-B score (described below). The first group selected (group 1) were patients who had minimal toxicity as indicated by the least fall in the score; patients in the second group (group 2) were those who experienced the greatest fall in the score. Scientific and ethical approval was obtained from local Research Ethics and Scientific Committees of the Royal Marsden NHS Foundation Trust, London. Written informed consent was obtained from all patients who participated in the study. Previous studies examining the potential for identifying patients at risk of developing severe gastrointestinal toxicity during long course pelvic radiotherapy treatment have employed similar methodologies and patient numbers [15].

2.4. Samples

All data and samples were collected prospectively. Faecal samples (between 10 and 50 mL) were collected within 12 h of evacuation and immediately stored at −20 °C. Gastrointestinal toxicity was recorded using the validated IBDQ-B, which has been developed for use in monitoring disease activity in Ulcerative Colitis and Crohn's Disease [18,19]. The IBDQ-B is the bowel specific part of the

questionnaire, which is a 10 question subset of the IBDQ. A maximum of seven points per question can be attained indicating no bowel toxicity (totaling a maximum score of 70) and a minimum score of 1 point per question (minimum score of 10 points showing most severe symptoms). A decline in score therefore represents increasing severity or frequency of symptoms. A decrease of more than six points has been shown to be clinically significant in a variety of settings [20,21]. Stool samples and IBDQ questionnaires were collected from all patients immediately before the start of radiotherapy (indicated as the baseline measurement) and after four weeks of treatment.

2.4. Analysis Methodology

Stool samples were thawed overnight to room temperature and then heated to 40 ± 0.1 °C in a dri-block^{TM} heater for 1 h before the experiment. Ten mL of sample was aliquoted to a 25 mL sterilin bottle and 5 mL of deionized water added and manually shaken to homogenize the sample. Here, each sample was divided into two aliquots, one for e-nose, the other for FAIMS. Due to limited volume of sample, in some cases there was only enough sample for one aliquot. In these cases FAIMS analysis was prioritized over e-nose. The sterilin bottle lids were also modified to take pipe fittings for 3 mm PTFE tubing.

For e-nose experiments, laboratory air was used as the carrier gas with a measured humidity of 20 ± 2% r.h. (relative humidity). Before each experiment, laboratory air was pumped through the e-nose at a flow rate of 500 mL/min for 450 s to create a stable baseline. The stool sample line was then switched in and the headspace from the stool sample was passed into the instrument (also at 500 mL/min for 450 s), with a further 450 s of laboratory air to allow the sensors to recover back to their original baseline. Each sample was analysed in a random sequence and run twice. The sample humidity was measured for all experiments at 49 ± 5% r.h. with a random distribution between groups.

Figure 2. Typical output of the (**a**) Electronic Nose and (**b**) Owlstone FAIMS instrument.

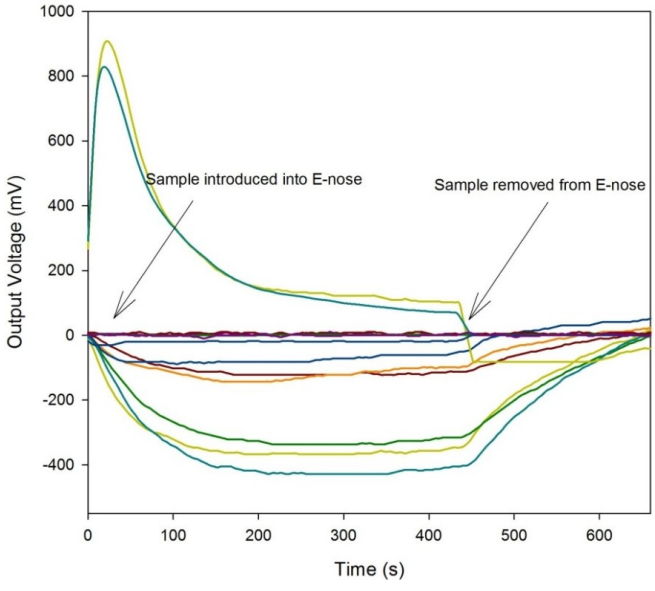

(**a**)

Figure 2. *Cont.*

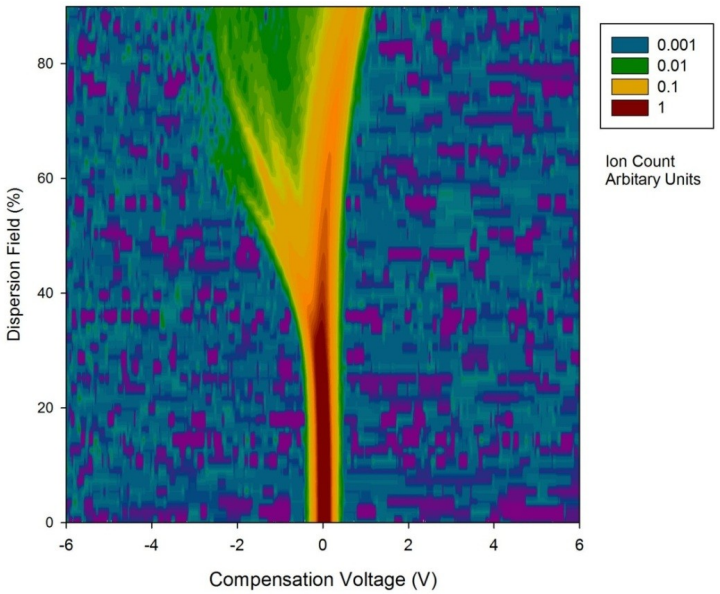

(**b**)

For the FAIMS instrument, a similar approach was taken, though here, clean scrubbed compressed air was used as the carrier. The flow rate over the sample was 2 L/min, with the dispersion field scanned between 0 and 90% in 51 steps and the compensation voltage from −6 V to 6 V in 512 steps. Each analysis took typically 180 s and each sample was analysed twice. Figure 2 shows both a typical e-nose response (without legend for simplicity) and a FAIMS response to a stool sample.

E-nose feature extraction was performed using Multisens Analyzer (JLM Innovations, Tübingen, Germany). E-nose analysis used the change in voltage (delta V) as the input feature for analysis. Before exploratory analysis was performed, the data was pre-processed with a standardization routine, built into the Multisens software. Here the mean value of all the features was subtracted from all the features. Additionally, the features were then divided by the standard deviation of the features. This was done for two reasons, the first process allows only the differences between features to be evaluated, thus the absolute feature value (normally associated with intensity) was not considered. The second process ensures that each feature will receive equal weighting in the exploratory analysis. This method has been applied due to the very different sensor technologies used within the electronic nose. This data was then analysed by two different methods, Principal Component Analysis (PCA) and by Linear Discriminant Analysis (LDA). For PCA, the samples were analysed as a single group and then post-categorized, whereas for LDA the samples were pre-categorised according to clinical outcome (low and high toxicity). Principal component analysis is a method to convert multiple sensor responses from a group of observations (here patients) into a smaller number of artificial variables called principal components, where the total number of principal components is less that the number of sensors. This transformation produces results whereby the first principal component accounts for the largest variability in the data as possible. The succeeding principal components, in order, have the next highest variability and so on. These additional components are constrained in that they must be orthogonal to (*i.e.*, uncorrelated to) the proceeding components. Thus, the results produced by this transformation are unclassified, but also show if the different observations produce the most

differences in the sensor responses. LDA is in some ways similar to PCA, but in this case, LDA attempts to find the optimum combination of sensors that best separates the differences between sample groups. So unlike PCA, which analyses samples based on the maximum difference, LDA looks for similarities within groups of samples.

FAIMS data was processed in Matlab (Mathworks Inc., Natick, MA, USA). As stated earlier, for each FAIMS measurement, the dispersion field was scanned between 0 to 90% and the compensation voltage between −6 V and 6 V. This produces 26,112 data points (as shown in Figure 1). In addition, both positive and negative ion counts were measured separately. Thus, the total number of data points was 52,254. To pre-process this data, a wavelet transform was applied (Daubechies D4). Wavelet transforms are a method used most commonly as a way of conditioning a signal into a more reduced form, before data compression. In simple terms, it projects the data on to a basis set of short waveforms (or wave-lets). Where the projections are large, this gives frequency and location information of this part of the original signal. Such techniques are incredibly good at separating signal information from noise. This is a natural method of pre-processing as the FAIMS output is a series of overlapping peaks, where one peak arises from molecules with a specific mobility. The wavelet transform gives information about this molecule, but also aids in discovering any additional molecules with similar, but not identical mobilities, by looking for differences in the frequency components on the signal. Figure 3, gives a section of the data after a wavelet transform had been applied. This was for a low toxicity patient, before treatment.

Figure 3. Wavelet transform of a low toxicity patient for elements 1 to 5,000.

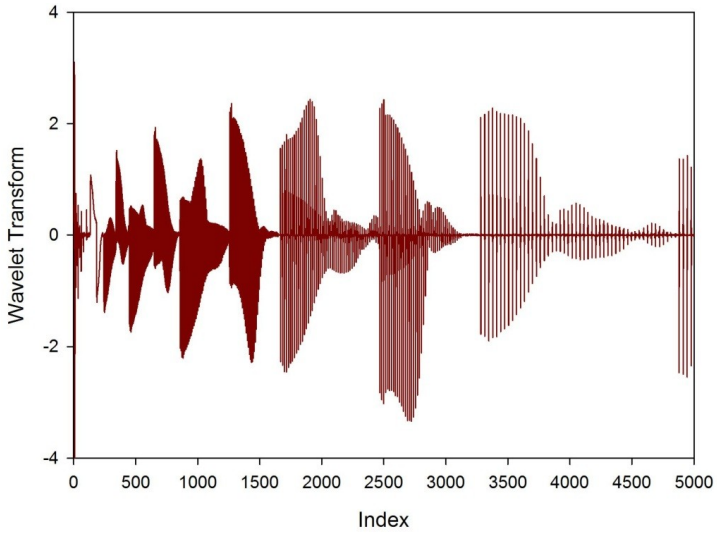

For analysis both the positive and negative ion count matrices from each sample were concatenated into a single 1D array 52,224 elements in length and then the wavelet transform applied. This produced a new 1D array, again 52,224 elements in size. Due to the large size of the dataset, it was required to identify elements that are suitable/useful in discriminating the different samples. To achieve this, thresholds were set for the within group (*i.e.*, low toxicity/high toxicity, pre and post treatment, thus four groups) scatter: $(\Sigma\sigma_i)^2$ and the between group scatter: $(\sigma_\mu)^2/(\Sigma\sigma_i)^2$, to identify dimensions for selection (σ_i: the standard deviation of the dimension in question within the group i, and σ_μ was the

standard deviation of the means of the dimension under test between classes). The exponents change the form to reflect that employed in Fisher Discriminant Analysis (FDA). FDA is almost identical to LDA, except that it does not make some of the assumptions used in LDA (such as normal distributed classes). It was discovered that this gave better discrimination for the methods and data captured by FAIMS.

This approach gave a two dimensional input parameter space to control the separation algorithm. This space was explored as follows. For each point in the input space 20 test sets (each containing one high toxicity response and one low) was re-classified. These test sets were not used in the identification of dimensions or the implementation of the FDA. This exploration identified regions in the parameter space where re-classification exceeded the 65.8% that would be expected for random re-classification (two standard deviations from the mean), and for which the success of re-classification was robust to perturbation in the parameters while changing the number of dimensions identified.

3. Results and Discussion

In total, 23 patients were investigated, 11 in the low toxicity group and 12 in the high toxicity group. The sample number, age, male/female ratio, radiotherapy dose and symptom burden (IBDQ-B score) analyzed by e-nose and FAIMS is shown in Table 2. The patients were of a similar age in both groups and had a similar dose of radiotherapy, including fractionation and duration of treatment (data not shown). By selection, the fall in the IBDQ-B score was only slight in the low toxicity group, but was marked and significant in the high toxicity. Numbers of samples per instrument differs slightly due to available volume of biological matter. Figure 4 shows the average e-nose sensor responses to the four groups from Table 2 (Figure 4(a)—raw values and Figure 4(b)—normalized before averaged). Here, only one set of data was used for these figures, even though the samples were run twice. This was done as we have previously noticed sample depletion with running samples using a dynamic sampling approach, thus the sensors are exposed to different gas profiles between tests.

Table 2. Baseline demographic characteristics and treatment features: Groups 1 (low toxicity) and 2 (High toxicity).

Feature	**Electronic Nose Analysis**		**FAIMS Analysis**	
Least Toxicity:	Pre-treatment	Post-treatment	Pre-treatment	Post-treatment
Number of patients	N = 11	N = 8	N = 11	N = 10
(Male:Female)	(9:2)	(7:1)	(9:2)	(8:2)
Mean Age (s.d.):	71.9 (4.8)	70.9 (5.1)	71.9 (4.8)	71.3 (4.5)
Mean Radiotherapy dose	61.8	63.3	61.8	61.0
Mean IBDQ Scores (s.d.)	67.4 (2.6)	67.5 (2.7)	67.4 (2.6)	67.3 (2.7)
High Toxicity:	Pre-treatment	Post-treatment	Pre-treatment	Post-treatment
Number of patients	N = 12	N = 11	N = 12	N = 10
(Male:Female)	(9:3)	(8:3)	(9:3)	(8:2)
Mean Age (s.d.):	69.8 (11.3)	69.1 (11.1)	69.8 (11.3)	71.8 (7.3)
Mean Radiotherapy dose	60.4	59.5	60.4	61
Mean IBDQ Scores (s.d.)	68.8 (1.7)	48.5 (7.4)	68.8 (1.7)	49.8 (6.2)

Figure 4. (**a**) Averaged e-nose sensor responses for different sample groups (axis is change in output voltage) and (**b**) Normalized responses.

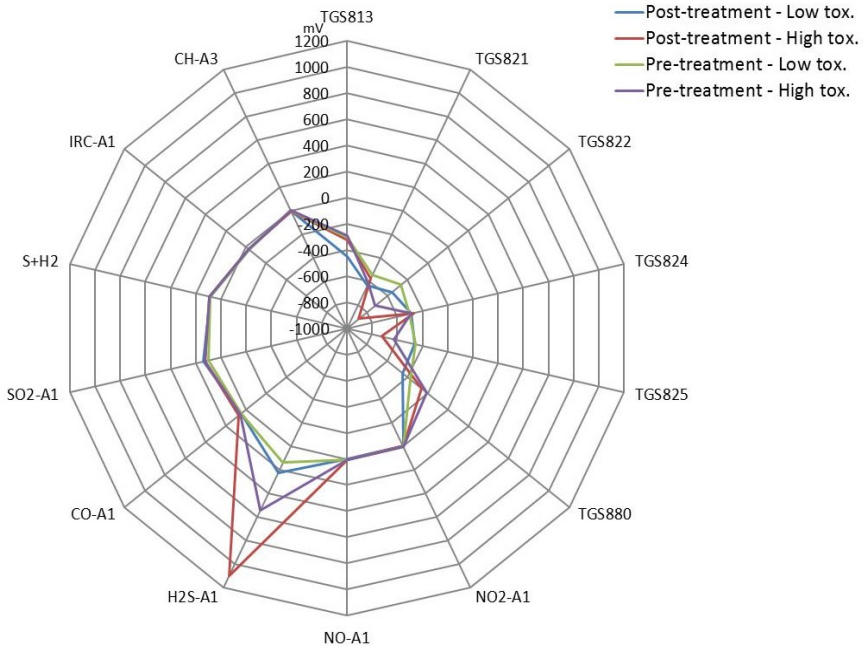

(**a**)

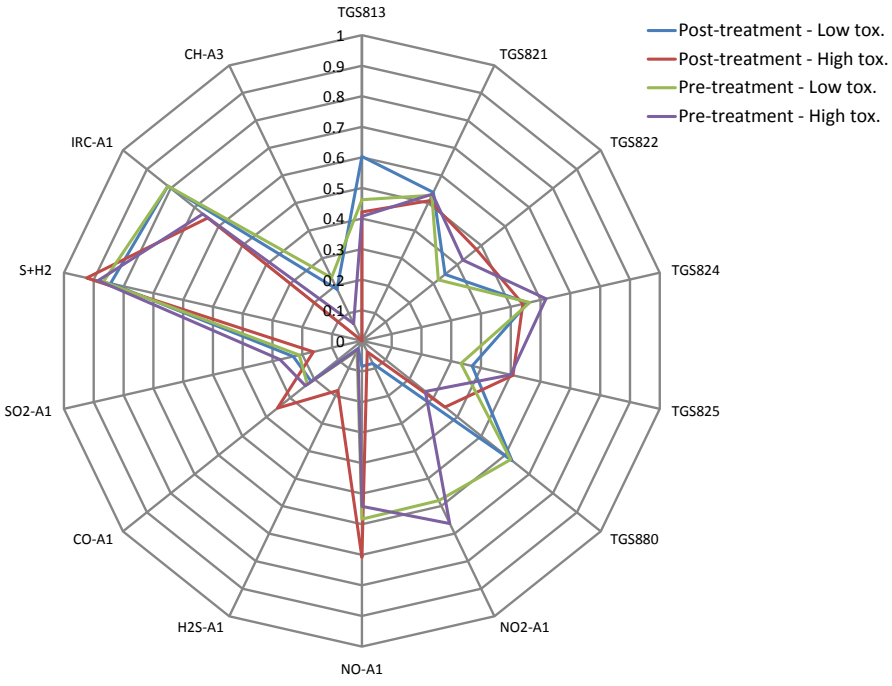

(**b**)

Samples after radiotherapy were analysed first, as the differences between these groups were likely to be greatest. Figure 5(a) shows the PCA of the two groups after treatment; there was a clear separation between the low and high toxicity groups. Figure 5(b) shows the loadings of this analysis, indicating that a large number of sensors contributed to the variability. LDA was also performed that again showed clear separation between the two groups (hence the results not shown here).

Figure 5. (**a**) PCA results from e-nose data and (**b**) loadings for samples taken four weeks after treatment referenced to Table 1.

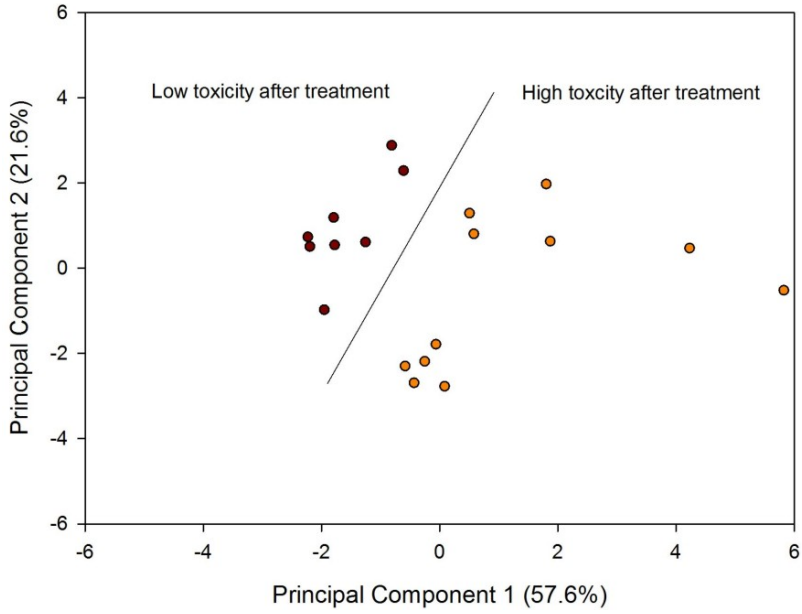

(**a**)

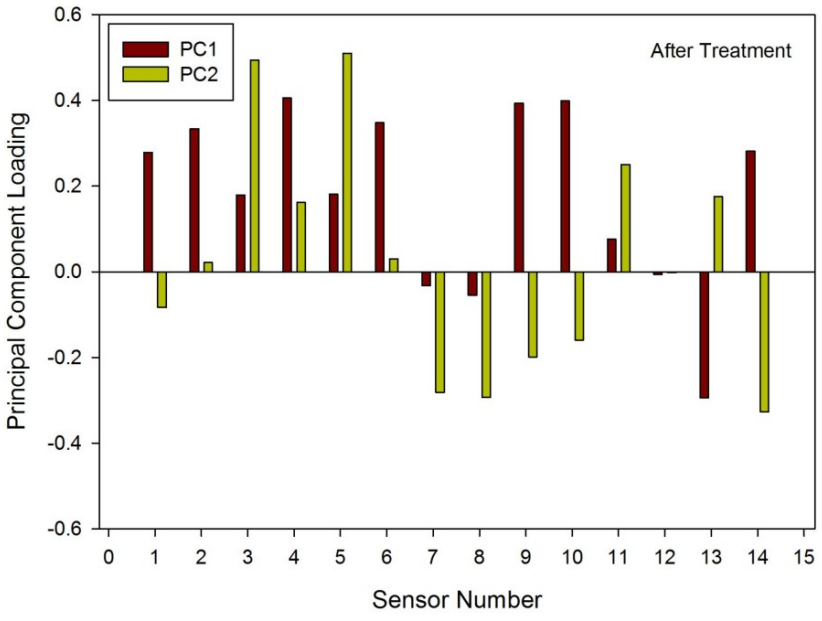

(**b**)

Analysis of the pre-treatment samples by PCA Figure 6(a) and by loadings Figure 6(b) indicated a difference between those who ultimately went on to have high or low toxicity. The differences, though statistically significant, were less striking.

Figure 6. (**a**) PCA results from e-nose data and (**b**) loadings for samples taken before treatment; categorized on their post-treatment toxicity referenced to Table 1.

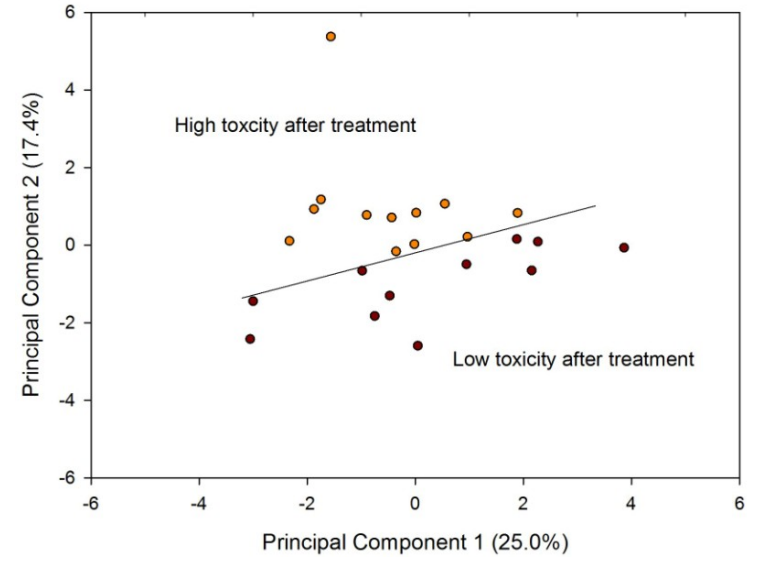

(**a**)

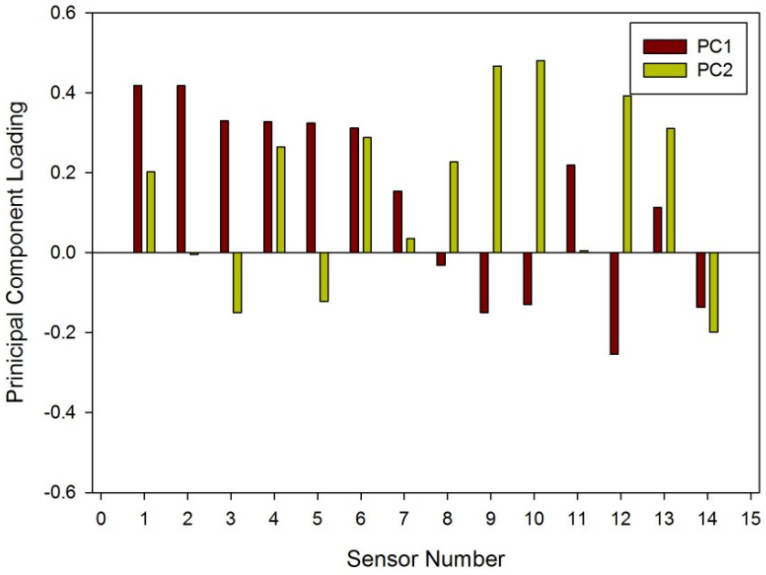

(**b**)

Finally, LDA was undertaken for all four groups. Though LDA could clearly separate high and low toxicity, pre and post treatment, it could not separate all four groups when analyzed together, as shown in Figure 7. What it does suggest is that there is a significant difference between those susceptible to radiation damage to those who are less so.

Although the sample numbers were small, a KNN (K-nearest neighbour) algorithm was applied to the electronic nose data to evaluate if it was possible to classify each sample correctly. Using n − 1 as the training set (where n is the number of samples), it was possible to correctly classify 22 out of 23 samples correctly (pre-treatment). When 10 samples were moved at random from the reference set to the test set, it was still able to correctly classify 80% of the samples consistently.

Figure 7. (**a**) LDA of all four groups using the e-nose and (**b**) loading plot associated with LDA referenced to Table 1.

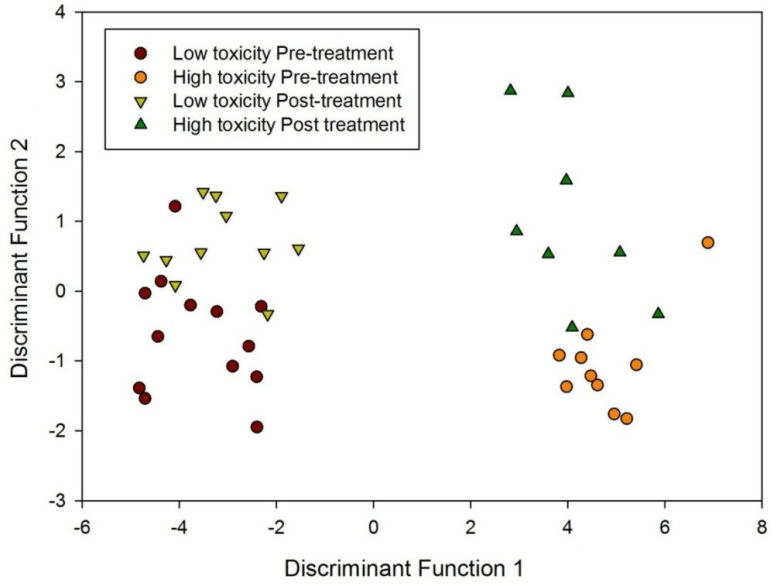

(**a**)

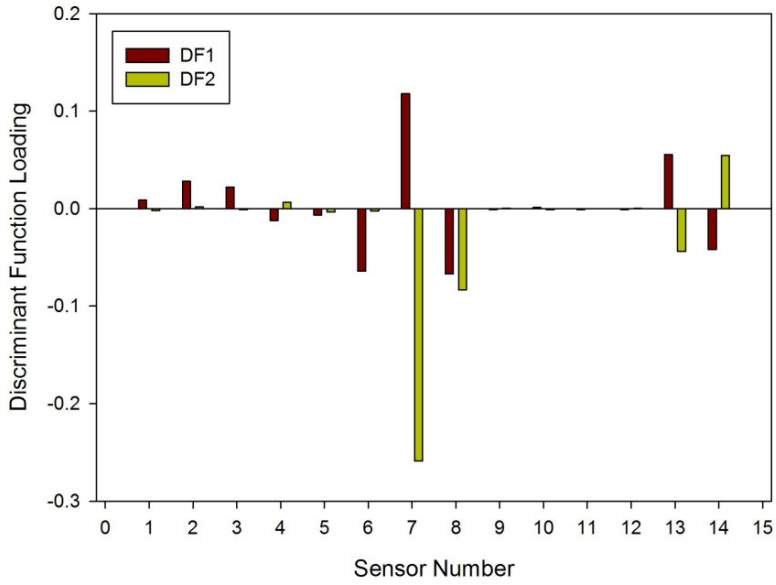

(**b**)

FAIMS analysis was done first from post radiotherapy samples as greater differences were expected, then on the pre-treatment samples and finally as all samples together. It was discovered that FDA could separate the different groups in all three cases. Figure 8(a) shows the FDA result from the FAIMS data from all the samples. Thresholds of 0.16 on the between class scatter and 0.12 on the within class scatter were imposed for the selection of dimensions. This identified 23 dimensions which were used for the FDA. Taking one sample out (n − 1) and re-performing the FDA, the accuracy of reclassification was in excess of 90% for both groups. Figure 8(b) shows the components of the projection vector identified and indicate that a large number contribute significantly to the classification.

Figure 8. (**a**) FDA of FAIMS data to all four groups and (**b**) loading plot associated with FDA using dimensions created in the analysis described earlier.

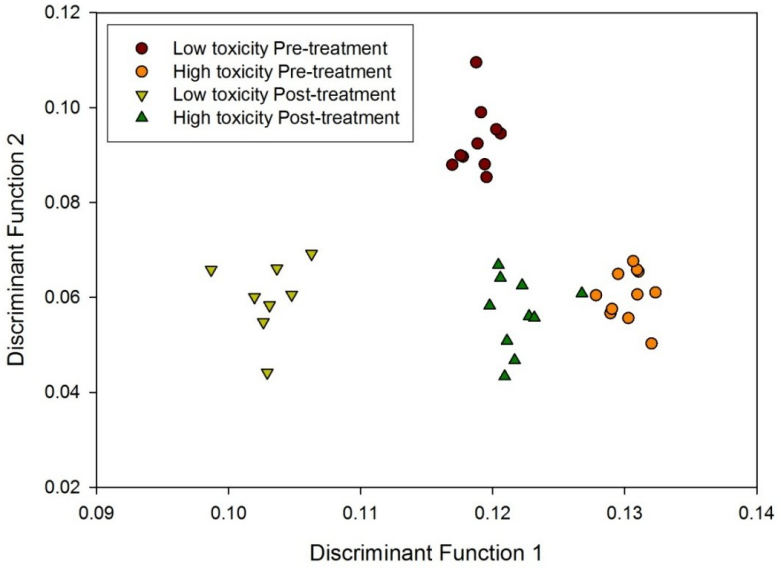

(**a**)

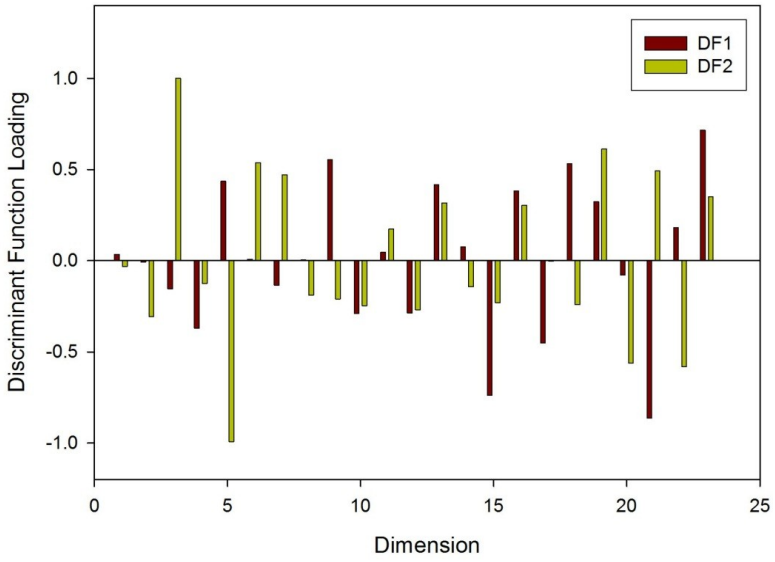

(**b**)

3.1. Discussion

Pelvic radiotherapy is a highly invasive procedure that frequently causes gastrointestinal side-effects as a result of tissue damage. Currently there is no reliable means of identifying those patients who will have a severe reaction. Our results indicate that the difference in odour profiles distinguishes patients severely affected from those with milder symptoms, using the patients themselves as the control group for this pilot study. Furthermore, this difference may be measured before treatment. As shown in the loading plot Figures 5(b) and 6(b) volatiles and gases obtained from stools collected before and after radiotherapy activate different sets of sensors, a clear indication of a change in the gas chemical profile. The gaseous outputs reflect the pattern of chemicals released by the fermentation of undigested

fibre by resident gut microbes, principally within the colon. The change observed, we hypothesise, results from radiation which perturbs the balance between the many species that together make up the gut microflora. Of note is that the LDA plot of the toxicity groups Figure 7(a) is unable to separate the before and after treatment for either toxicity group, but clearly distinguishes those patients who will be severely affected from those less so. More interesting, the loading plot Figure 7(b) shows that these groups are separated by gases/vapours that could be associated with the fermentation process, specifically hydrogen, methane/combustible, carbon dioxide, nitrogen dioxide and volatile organic compounds.

Our pilot data do not allow us to comment upon how radiation affects microbial behaviour, either by direct action or indirectly through resultant mucosal inflammation. We are also unable to comment if the altered microbial balance is a passive reflection of mucosal inflammation or whether it actively worsens it. Nevertheless our results suggest we now have the potential to identify patients "at risk" of severe radiation-induced gastrointestinal damage before starting such treatment.

Our speculation on the role of microbes is plausible and has a precedent in Crohn's disease, a gut disease characterized by inflammation—some patients affected mildly but others severely. Using electronic noses we have identified that the patterns of volatiles and gases emitted from the urine of such patients has a different pattern to that in health, signifying a difference in the respective resident microbial flora; furthermore, the pattern changes again when Crohn's activity flares up [22]. An interesting and very relevant recent finding is that the spectrum of microbial profile is reduced in Crohn's disease. Hence there is growing interest in the possibility that altered gut microbes may be more intimately linked with the disease than was at first thought.

Studying the microbial flora is difficult as many species cannot (as yet) be cultured; hence complex molecular methods are required, which currently remains at the research level. Studying instead the volatiles from gut fermentation provides a more accessible insight into microbial behaviour. Gas chromatography (GC)-mass spectrometry (MS) can identify individual volatiles but is complex and expensive; examining the overall pattern of the "fermentation signature" instead, using electronic noses or FAIMS, is more accessible.

Using the electronic nose to recognize odour patterns we were able to separate the "high risk" group from those at lower risk. We achieved the same separation with FAIMS, proof of principle that the investigation of movement patterns of the volatiles can be used in such medical investigations.

FAIMS is an interesting technology for future development. It has the advantages of high sensitivity (compared with traditional electronic nose instruments), can operate at room temperature and does not require special gases (as with GC or GC-MS). Its high sensitivity is however also a limitation as contamination reduces performance. Its other limitation is the very large datasets it generates, which in our study was 50,000 data points per sample. However, our technique of wavelet transformation combined with FDA allows us to handle such large data. FAIMS is still in its infancy but the technique is powerful; it therefore seems likely that as research continues the instruments will improve and evaluation of large datasets will allow full comparison with traditional electronic nose instrumentation.

4. Conclusions

Radiotherapy as a treatment for cancer has attained a high level of success, but can have major side-effects. For those patients receiving pelvic radiotherapy there is a marked variability in the level

of gastro-intestinal toxicity they may suffer. To inform treatment pathway, it would be beneficial to identify those patients who will have the most significant reaction and then alter their treatment accordingly—a patient tailored approach. In this pilot study, we have taken stool samples from patients before and four weeks after receiving radiotherapy. Of these patients a subset of 23 patients, who had the most significant reaction and those with the minimum reaction, were analysed by an in-house electronic nose and a FAIMS instrument. In this instance patients acted as their own control, as the aim of our study was to determine and track any changes (gases/volatiles) which could be detected. Using PCA for e-nose data and a wavelet transform followed by FDA for FAIMS data, the results indicated that it was possible to detect differences in odour profile of stool samples after treatment. More interestingly, these patients can be separated using these analysis techniques before radiotherapy. This suggests that there are substantial differences in stool composition between these two groups, prior to radiotherapy, indicating a difference in indigenous bacterial micro-flora between patients. Future work will look at increasing the size of the sample groups, analysing patients between the two extremes, undertaking GCMS (which is particularly challenging for fecal samples due to the large number of different chemicals involved) and instigating a study into the bacterial differences.

Acknowledgments

We would like to thank the Bardhan Research and Education Trust (BRET) for supporting this work.

References

1. Persaud, K.; Dodd, G. Analysis of discrimination mechanisms in the mammalian olfactory system using a model nose. *Nature* **1982**, *299*, 352–355.
2. Perisa, M.; Escuder-Gilabertb, L. A 21st century technique for food control: Electronic noses. *Anal. Chim. Acta* **2009**, *638*, 1–15.
3. Röck, F.; Barsan, N.; Weimar, U. Electronic nose: Current status and future trends. *Chem. Rev.* **2008**, *108*, 705–725.
4. Pearce, T.C.; Schiffman, S.S.; Nagle, H.T.; Gardner, J.W. *The Handbook for Machine Olfaction*; Wiley-VCH: Berlin, Germany, 2006; pp. 445–453.
5. D'Amico, A.; Pennazza, G.; Santonico, M.; Martinelli, E.; Roscioni, C.; Galluccio, G.; Paolesse, R.; di Natalea, C. An investigation on electronic nose diagnosis of lung cancer. *Lung Cancer* **2010**, *68*, 170–176.
6. Kateb, B.; Ryan, M.A.; Homer, M.L.; Lara, L.M.; Yin, Y.; Higa, K.; Chen, M.Y. Sniffing out cancer using the JPL electronic nose: A pilot study of a novel approach to detection and differentiation of brain cancer. *NeuroImage* **2009**, *47*, T5–T9.
7. Pennazza, G.; Santonico, M.; Bartolazzi, A.; Martinelli, A.; Paolesse, R.; di Natale, C.; Bono, R.; Tamburrelli, V.; Cristina, S.; D'Amico, A. Melanoma volatile fingerprint with a gas sensor array: *In vivo* and *in vitro* study. *Proc. Chem.* **2009**, *1*, 995–998.
8. Arasaradnam, R.P.; Quraishi, N.; Kyrou, I.; Nwokolo, C.U.; Joseph, M.; Kumar, S.; Bardhan, K.D.; Covington, J.A. Insights into "fermentonomics": Evaluation of volatile organic compounds (VOCs) in human disease using an electronic "e-nose". *J. Med. Eng. Technol.* **2010**, *35*, 87–91.

9. Oh, E.H.; Song, H.S.; Park, T.H. Recent advances in electronic and bioelectronic noses and their biomedical applications. *Enzym. Microb. Technol.* **2011**, *48*, 427–437.
10. Mäkinen, M.A.; Anttalainen, O.A.; Sillanpa, M.E.T. Ion mobility spectrometry and its applications in detection of chemical warfare agents. *Anal. Chem*. **2010**, *82*, 9594–9600.
11. Khalid, U.; McGough, C.; Hackett, C.; Blake, P.; Harrington, K.J.; Khoo, V.S. A modified inflammatory bowel disease questionnaire and the vaizey incontinence questionnaire are more sensitive measures of acute gastrointestinal toxicity during pelvic radiotherapy than RTOG grading. *Int. J. Radiat. Oncol. Biol. Phys*. **2006**, *64*, 1432–1441.
12. Andreyev, H.J.N.; Wotherspoon, A.; Denham, J.D.; Hauer-Jensen, M. Defining pelvic-radiation disease for the survivorship era. *Lancet Oncol.* **2010**, *11*, 310–312.
13. Andreyev, H.J.N. Gastrointestinal problems following pelvic radiotherapy: The past, the present and the future. *Clin. Oncol.* **2007**, *19*, 790–799.
14. Wedlake, L.J.; Andreyev, H.J.N. Manipulating the consequential effect: An alternative approach to reducing pelvic radiation disease other than dose reduction. *Curr. Opin. Support Palliat. Care* **2011**, *5*, 25–28.
15. Manichanch, C.; Varela, E.; Martinez, C.; Antolin, M.; Llopis, M.; Dore, J.; Giralt, J.; Guarner, F.; Malagelada, J.R. The gut microbiota predispose to the pathophysiology of acute postradiotherapy diarrhea. *Am. J. Gastroenterol*. **2008**, *103*, 1754–1761.
16. Denham, J.W.; Hauer-Jensen, M. The radiotherapeutic injury-a complex "wound". *Radiother. Oncol*. **2002**, *63*, 29–45.
17. Shvartsburg, A.A.; Smith, R.D.; Wilks, A.; Koehl, A.; Ruiz-Alonso, D.; Boyle, B. Ultrafast differential ion mobility spectrometry at extreme electric fields in multichannel microchips. *Anal. Chem*. **2009**, *81*, 6489–6495.
18. Guyatt, G.; Mitchell, A.; Irvine, E.; Singer, J.; Williams, N.; Goodacre, R. A new measure of health status for clinical trials in inflammatory bowel disease. *Gastroenterology* **1989**, *96*, 804–810.
19. Rubin, G.; Hungin, A.; Chinn, D.; Dwarakanath, D. Quality of life in patients with established inflammatory bowel disease: A UK general practice survey. *Aliment. Pharmacol. Ther.* **2004**, *19*, 529–535.
20. Olopade, F.O.; Norman, A.R.; Blake, P. The inflammatory bowel disease questionnaire and the Vaizey incontinence questionnaire are useful to identify gastrointestinal toxicity after pelvic radiotherapy. *Br. J. Cancer* **2005**, *92*, 1663–1670.
21. Hlavaty, T.; Persons, P.; Vermeire, S.; Ferrante, M.; Pierlik, M.; van Assche, G.; Rutgeerts, P. Evaluation of short-term responsiveness and cut-off values of Inflammatory Bowel Disease Questionnaire in Crohn's disease. *Inflamm. Bowel Dis.* **2006**, *12*, 199–204.
22. Arasaradnam, R.P.; Ouaret, N.; Thomas, M.; Quraishi, N.; Nwokolo, C.; Bardhan, K.D.; Covington, J.A. A novel tool for non invasive diagnosis and tracking of patients with Inflammatory Bowel Disease (IBD). **2012**, in press.

Appendix E

Detection of colorectal cancer (CRC) by urinary volatile organic compound analysis

This Appendix contains a paper presenting a proof of principle of the effectiveness of FAIMS at analysing urine samples to detect CRC. I developed the analysis procedure for the FAIMS spectra, wrote the code to implement it and applied it to the data. The trial was designed and otherwise implemented by the other authors.

OPEN ACCESS Freely available online

PLOS ONE

Detection of Colorectal Cancer (CRC) by Urinary Volatile Organic Compound Analysis

Ramesh P. Arasaradnam[1,3]*, Michael J. McFarlane[3], Courtenay Ryan-Fisher[3], Erik Westenbrink[2], Paula Hodges[3], Matthew G. Thomas[2,6], Samantha Chambers[3], Nicola O'Connell[3], Catherine Bailey[3], Christopher Harmston[5], Chuka U. Nwokolo[3], Karna D. Bardhan[1,4], James A. Covington[2]

1 Clinical Sciences Research Institute, University of Warwick, Coventry, Warwickshire, United Kingdom, **2** School of Engineering, University of Warwick, Coventry, Warwickshire, United Kingdom, **3** Department of Gastroenterology, University Hospital Coventry & Warwickshire, Coventry, Warwickshire, United Kingdom, **4** Department of Gastroenterology, Rotherham General Hospital, Rotherham, Yorkshire, United Kingdom, **5** Department of Surgery, University Hospital Coventry and Warwickshire, Coventry, Warwickshire, United Kingdom, **6** MOAC Doctoral Training Centre, University of Warwick, Coventry, Warwickshire, United Kingdom

Abstract

Colorectal cancer (CRC) is a leading cause of cancer related death in Europe and the USA. There is no universally accepted effective non-invasive screening test for CRC. Guaiac based faecal occult blood (gFOB) testing has largely been superseded by Faecal Immunochemical testing (FIT), but sensitivity still remains poor. The uptake of population based FOBt testing in the UK is also low at around 50%. The detection of volatile organic compounds (VOCs) signature(s) for many cancer subtypes is receiving increasing interest using a variety of gas phase analytical instruments. One such example is FAIMS (Field Asymmetric Ion Mobility Spectrometer). FAIMS is able to identify Inflammatory Bowel disease (IBD) patients by analysing shifts in VOCs patterns in both urine and faeces. This study extends this concept to determine whether CRC patients can be identified through non-invasive analysis of urine, using FAIMS. 133 patients were recruited; 83 CRC patients and 50 healthy controls. Urine was collected at the time of CRC diagnosis and headspace analysis undertaken using a FAIMS instrument (Owlstone, Lonestar, UK). Data was processed using Fisher Discriminant Analysis (FDA) after feature extraction from the raw data. FAIMS analyses demonstrated that the VOC profiles of CRC patients were tightly clustered and could be distinguished from healthy controls. Sensitivity and specificity for CRC detection with FAIMS were 88% and 60% respectively. This study suggests that VOC signatures emanating from urine can be detected in patients with CRC using ion mobility spectroscopy technology (FAIMS) with potential as a novel screening tool.

Citation: Arasaradnam RP, McFarlane MJ, Ryan-Fisher C, Westenbrink E, Hodges P, et al. (2014) Detection of Colorectal Cancer (CRC) by Urinary Volatile Organic Compound Analysis. PLoS ONE 9(9): e108750. doi:10.1371/journal.pone.0108750

Editor: Keping Xie, The University of Texas MD Anderson Cancer Center, United States of America

Received June 13, 2014; **Accepted** August 25, 2014; **Published** September 30, 2014

Data Availability: The authors confirm that all data underlying the findings are fully available without restriction. All relevant data are included within the paper.

Funding: The work was supported by Bardhan Research and Education Charity (BRET) charity, Warwickshire Private Hospital charity, Eveson trust - provided funding for materials. BRET was established by Professor Bardhan but he had no input into the funding decision made by the grant awarding committee. The funders had no role in study design, data collection and analysis, decision to publish, or preparation of the manuscript.

Competing Interests: The authors have declared that no competing interests exist.

* Email: r.arasaradnam@warwick.ac.uk

Introduction

Colorectal cancer (CRC) is one of the leading causes of cancer related death in Europe and the USA [1,2]. At present there is a lack of effective, non-invasive screening tests for CRC. Current methods utilise guaiac based faecal occult blood (gFOB) testing, however, this has now largely been replaced by Faecal Immunochemical Testing (FIT). Whilst this is an improvement, FIT still shows relatively low sensitivity for CRC, 66–88%, depending on the cut off values for haemoglobin (50–200 ng/ml), with a specificity of 87–96% [3–5]. The sensitivity for advanced adenoma is even lower at 27–41%, with a specificity of 91–97% [5]. The uptake of screening utilising faecal samples is also an issue, with approximately 50% of invited participants not accepting population based FOBt screening in our locality.

Non-invasive testing of cancers, using Volatile Organic Compounds (VOCs) and gases that emanate from urine, breath, stool and blood, has received growing interest and has been an expanding area of research in recent years. This work initially started from the use of canines to detect cancers, which showed a marked ability to discriminate cancer patients from healthy individuals [6,7,8]. However, more recently a number of groups have indicated that it is possible to use gas phase analytical instruments, specifically gas chromatography and mass spectrometry (GC-MS), selective-ion flow mass spectrometer (SIFT) and the electronic nose (e-nose), to detect lung, breast, bladder and prostate cancers [9,10,11,12]. For a detailed review on gas phase biomarkers in Gastroenterology, please see Arasaradnam et al [13].

In direct relation to colorectal cancer (CRC), recent work has shown that it is possible to discriminate cancer from non-cancer patients, but can also be used for the discrimination of lung, breast, prostate and colorectal cancer from each other by analysing breath samples [14]. This is further supported by recent work that has also shown that CRC can be distinguished from controls with over 75% accuracy using GC-MS, again employing breath analysis [15]. VOCs present in urine have also been shown to distinguish CRC patients from control groups and other cancers (leukaemia

Table 1. Demographic data for CRC and control patients.

N = 133	*CRC*	*Controls*
Number	83	50
Mean Age (years)	60 (17)	47 (16)
Sex: M/F	53:30	21:29
Mean BMI	27 (7)	26 (5)
Current Smokers (% of whole population)	6.0%	1.5%
Alcohol: Greater than recommended units/week (% of whole population)	5.3%	3.8%

Figures in parenthesis are standard deviations (SD).
doi:10.1371/journal.pone.0108750.t001

and lymphoma), with GC-MS [16]. The electronic nose (Cyrano 320, Sensigent, USA) has also been shown to discriminate between CRC and healthy controls when the VOCs profile in faeces are analysed (85% sensitivity and 87% specificity). Additionally the e-nose was able to discriminate between advanced adenomas and healthy controls with 62% sensitivity and 86% specificity [5]. These studies support the existence of putative gas phase biomarkers within biological output media for detecting CRC and thus could be the basis of a rapid screening tool.

VOCs can exist in the gaseous phase and are present in exhaled air, sweat, urine and faeces [17,18]. The mechanism for the generation of VOCs is the subject of current research but they are perturbed in many physiological and pathological states - affected by diet and disease states. It is believed that the generation of VOCs within the bowel are the result of colonic bacteria undergoing fermentation of non-starch polysaccharides – fibre consumed by the host. As such, they represent the complex interaction of colonic cells, human gut microflora and invading pathogens [19,20]. The study of the resultant products of fermentation which we have termed 'the fermentome' [17,18,21,22] can be measured in urine. The latter is presumed possible due to the altered gut permeability afforded in certain gut diseases [23]. We believe that VOCs represent a bio-signature that represents the sum of the multifactorial influences (genetics, environmental factors including diet and disease states) affecting an individual. The aim of this study was to test the potential of FAIMS – a novel highly sensitive technology to differentiate between CRC and healthy controls using only urine samples.

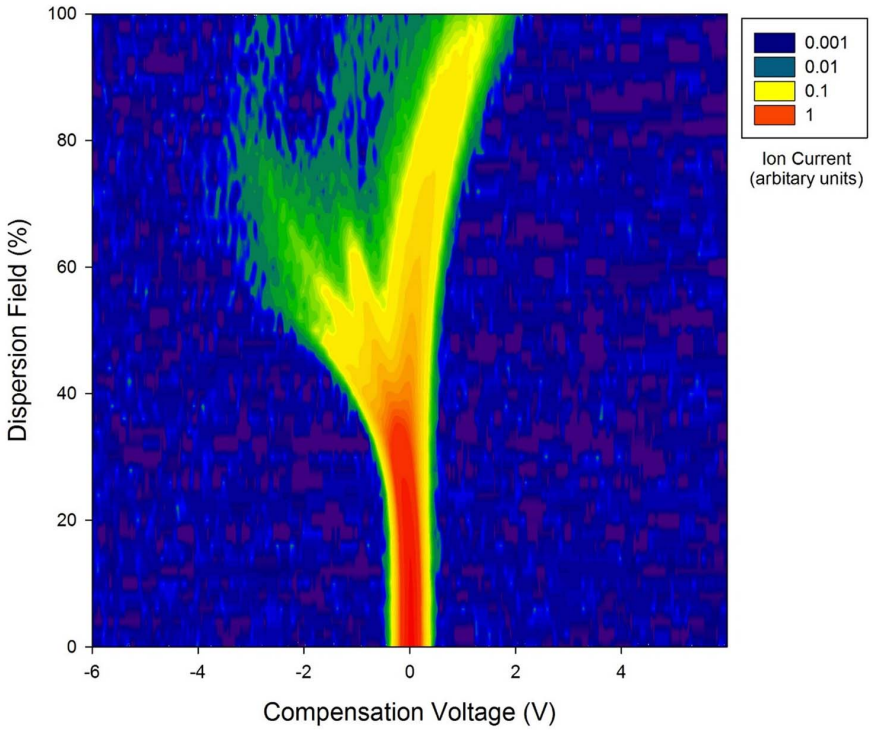

Figure 1. Log of raw data from the FAIMS instrument for a colorectal cancer patient. Intensity is in arbitrary units of ion count.
doi:10.1371/journal.pone.0108750.g001

Table 2. Staging for CRC patients using the tumour, nodal and metastases classification (TNM).

N = 83	T_1		T_2		T_3		T_4	
	N_0	$N_{1/2}$	N_0	$N_{1/2}$	N_0	$N_{1/2}$	N_0	$N_{1/2}$
Non-metastatic (M_0)	3	1	6	5	19	19	5	7
Metastatic (M_1)	0	0	0	0	4	1	0	4

N.B. 9 CRC patients could not be fully staged (inoperable).
doi:10.1371/journal.pone.0108750.t002

Materials and Methods

2.1 Subjects

One hundred and thirty three individuals were recruited prospectively for this study. Eighty-three of these patients had histologically confirmed colorectal cancer and fifty were healthy individuals who had a recent normal colonoscopy. The mean age of the CRC patients was 60 years (SD 17 years), 53 (64%) were male. The demographics of the subjects are shown in Table 1.

2.2 Study Design

This was a case control study where patients were recruited from outpatient clinics at University Hospital Coventry & Warwickshire, UK. Urine was then collected in standard universal Sterilin specimen containers (Newport, UK) and frozen immediately to −80°C, for subsequent batch analysis.

2.3 Analysis

Samples were thawed at room temperature overnight, aliquoted into appropriate sample bottles and analysed using the FAIMS experimental methods described below.

2.3.1 FAIMS. For FAIMS analysis, a commercial instrument was utilised (Lonestar, Owlstone, UK, employing an ATLAS sampling system and split flow box). This system achieves separation of chemical components on the basis of differences in the electric field dependence of ionised chemical mobilities. FAIMS allows gas molecules to be separated and analysed at atmospheric pressure and room temperature, unlike similar traditional analytical techniques. After a sample is ionised, it is composed of ions of various sizes and types. These are introduced between two metal plates and an asymmetric high voltage waveform is applied to these plates, subjecting the ionized molecules to high electric fields. The difference in movement of these molecules within this high electric field can be measured, thus resulting in a separation of the complex mixture.

A sample of 5 ml of urine is aliquoted into a 20 ml glass vial and placed inside the ATLAS sampler. The sampler heats the sample to (in our case) 40±0.1°C, when the sample reaches the correct temperature (typically 10 min), clean synthetic air is passed over the sample and into the Lonestar FAIMS instrument. The flow rate over the sample is 500 ml/min and increased to 2 L/min by additional clean air before being passed into the instrument. The Lonestar is set up to scan between 0 and 90% dispersion field (the dispersion field represents the magnitude of the electric field) in 51 steps and a compensation voltage of between −6 V and +6 V in 512 steps. The compensation voltage is used to remove the effect of the drift produced by the high electric field, thus only molecules that have a specific mobility exit the plates at that point. Figure 1 shows a typical FAIMS 'plume' produced from a CRC patient's urine sample plotted on a log scale.

2,3.2 GC-MS. For GC-MS analysis, separate aliquots of 5 ml are taken from each sample to run through a Bruker Scion SQ GC-MS instrument. Each aliquot was agitated and heated to 60°C for 5 minutes, before the contents of its headspace are extracted using a Combi-PAL ITEX automated pre-concentrator system. The volatiles contained in the ITEX were then released by heating to 250°C, and injected into the instrument at a split ratio of 1:20 with helium carrier gas. The Restek Rxi-624Sil column (20 m length, 0.18 mm ID, 1.0 um df) fitted to the GC was kept at a constant 50°C for 1 minute before being increased up to 280°C at a rate of 20°C/min, separating out the constituent VOCs in terms of molecular weight and polarity. After an initial detection to produce a chromatogram, the VOC molecules are fragmented by the mass spectrometer and detected to produce corresponding

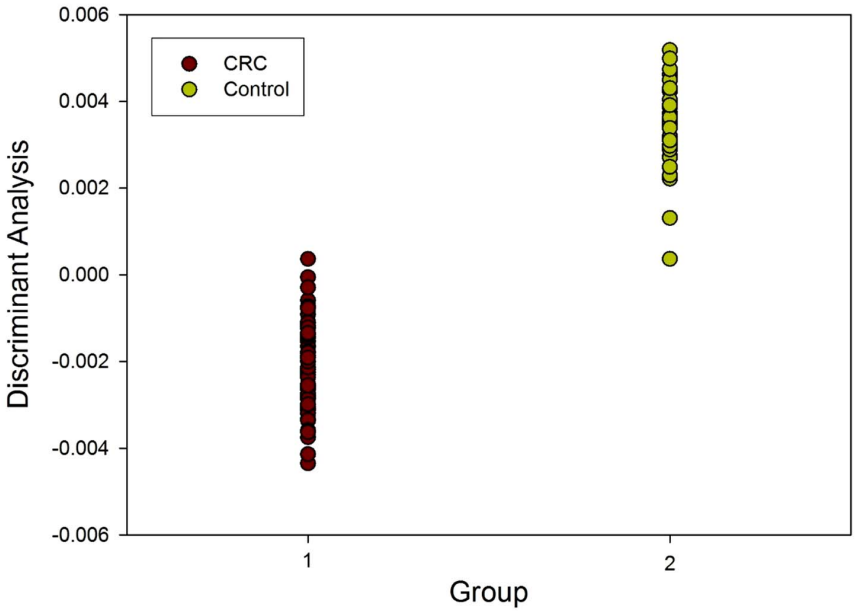

Figure 2. Fisher Disciminant Analysis (FDA) of FAIMS data in patients with CRC and controls.
doi:10.1371/journal.pone.0108750.g002

mass spectra. These are correlated with the GC chromatogram peaks, and checked against a National Institute of Standards and Technology library (NIST 2013) of chemical compounds. This was perfrimed in order to gain additional insight into the specific chemical groups that make up the volatile headspace of the urine samples in those with CRC.

2.4 Statistical Methods

Data analysis for FAIMS results is performed using Fisher Discriminant Analysis. This allows for the simple interpretation of complex data to determine if differences in groups can be detected. The data was processed in Matlab (Mathworks Inc., USA, R2013b). For analysis, both the positive and negative ion count matrices of each sample were concatenated into a single 52,224 element vector (or 1D array). These were then wavelet transformed using a Daubechies D4 wavelet, a technique commonly used in data compression and has the ability to separate out subtle signals within a dataset. Data points within the 52,224 elements suitable for discrimination are then identified. This is achieved by calculating the within class scatter ($\Sigma\sigma_i$) and the between class scatter $[(\sigma_\mu)^2/(\Sigma\sigma_i)^2]$ for each point within the vector (thus the same datapoints (or variable) from all the sample datasets are examined and the within class as well as between class scatter calculated across all the samples), to generate two further 1D arrays, again formed of 52,224 data points. Different thresholds are then set for within class and between class scatter and the variables that are within these thresholds are then used for data processing by fisher discriminant analysis (FDA; a pre-classified linear technique). To test the validity of the FDA, five samples from each group (CRC and controls) were removed before the FDA was performed. Then, based on the FDA results of the remnant, a prediction is made on the group of the unknown

Table 3. GC-MS peaks for the CRC patients and corresponding National Institute of Standards and Technology (NIST) targets for these peaks.

Average GC Retention Time (min)	*Major MS Peaks*	*Common NIST targets*
1.4	42, 43, 45, 56, 58	Acetaldehyde, Ethylene Oxide, Oxalic Acid
1.53	42, 44, 55, 67	Dimethyl Diazene, Cyclobutyl Amine, Oxepane
1.75	42, 43, 58	Acetone
2.95	39, 43, 44, 58, 71, 86	2-Pentanone, 3-methyl-2-Butanone, 2,3-Butanedione
4.56	43, 58, 71	4-Heptanone, 3-Heptanone, 2,4-dimethyl-3-Pentanone
4.7	44, 51, 63, 78, 104	Acetyloxime-Pyridine Carboxaldehyde, Hydrocinnamoyl-Bezene-ethanamine, Styrene, Dimethyl-Thiourea
4.77	39, 40, 60, 72, 99	Allyl Isothiocyanate, Isothiocyanato-cyclopropane, 2-cyano-acetamide
5.31	42, 44, 56, 75, 94, 118, 133, 151	Methoxy-phenyl-oxime, Ethylbenzoic acid (pentyl ester), Carbamic acid (methyl ester)
5.38	41, 43, 44, 57, 72	Hexen-1-ol, 4-methyl-1-hexene, Hexanal

doi:10.1371/journal.pone.0108750.t003

samples. This prediction is based on a KNN (k-nearest neighbor) method. This process is repeated ten times for each pair threshold values until optimum thresholds, and thus set of variables, are identified. This variable group is then used for the remainder of the analysis process to calculate sensitivity and specificity. For further details on analyses described in detail, please see Covington et al [23].

2.5 Ethics

Scientific and ethical approval was obtained from local Research & Development Department and Warwickshire Ethics Committee 09/H1211/38. Written informed consent was obtained from all patients who participated in the study.

Results

The demographic data of the cancer and non-cancer group are described in Table 1. No statistically significant difference between the groups was noted however, as expected there was male gender predominance. Details of the tumour staging for the 83 CRC patients are shown in Table 2.

The analysis of the FAIMS data for CRC patients and controls was carried out using Fisher Discriminant Analysis, as described above, and the results from the identified variables are shown in Figure 2. Reclassification for CRC was correct in 74% of cases ($p<0.001$). The sensitivity and specificity of the FAIMS analysis to detect CRC were 88% and 60% respectively.

The CRC patients' urine was also analysed by GC-MS, the results can be found in table 3, along with a list of corresponding chemicals from the National Institute for Standards and Technology (NIST) database. No unique chemical was identified in those with CRC compared with controls.

Discussion

This study is the first to our knowledge to report the utility FAIMS analyses for CRC detection in urine and supports previous work by others using electronic nose [5] and GCMS [16]. This has been achieved by investigating how gases and vapours (VOCs) emanating from urine samples are disparate in those with CRC compared with controls. Our findings also support previous work where, VOC signature differences were noted in CRC patients within different biological materials (faeces, breath and urine) [5,15,16]. Our CRC cohort had a male sex predominance, as would be expected for a population of CRC patients, whilst our control group had a slight female predominance. This could raise the prospect of sex bias within the cohort, however, whilst the pattern of VOCs and by association, the fermentome, could theoretically be affected by sex and age, data from our previous published studies of IBD, bile acid malabsorption, pelvic cancer and coeliac disease have not shown any propensity for age and sex affecting the VOC signals [23,24,25,26,27].

De Meij et al showed that the e-nose could discriminate CRC from healthy controls with 85% sensitivity and 87% specificity, and could also distinguish advanced adenomas from healthy controls with 62% sensitivity and 86% specificity [5]. Our study has shown using urine specimens rather than faeces – with FAIMS demonstrating a sensitivity of 88% and a specificity of 60%. This has importance especially in our local population where uptake of screening is poor due to the requirement to produce faecal samples.

Ion mobility has a number of advantages over both GCMS and e-nose: for example it is undertaking a physical measurement of molecules instead of a chemical interaction (as would a traditional e-nose) and secondly, the sensitivity is much higher i.e. parts per billion to parts per trillion. This makes it an ideal platform for a future screening tool especially as the sensitivity is high. Our findings expand on previous research describing how both e-nose and FAIMS technologies can be used to distinguish effects of radiation in pelvic cancers [25] and inflammatory conditions e.g. between Crohn's disease and ulcerative colitis [26], in addition to Bile acid malabsorption and Coeliac disease [23,27].

Genetic stool markers have received interest as a potential non-invasive screening target for CRC. Lidgard et al [28] performed a study of automated stool DNA analysis for β-actin, mutant *kRAS*, aberrantly methylated *BMP3* and *NDRG4*, and faecal haemoglobin. This showed a sensitivity of 98% and 90% specificity for CRC and 57–83% sensitivity for advanced adenomas depending on size. Our study shows comparable sensitivity results, but at a much lower process cost, and with urine rather than faecal sampling.

The unique chemical fingerprint or 'bio-odorant fingerprint' produced by the different disease states, and healthy individuals, shows the potential of this technology to screen for, and aid, in the diagnosis of CRC. It also has the potential to aid in further investigation of individuals with other gastrointestinal diseases. Gases and vapours are thought to be produced by the process of colonic fermentation involving a complex interaction between the colonocyte cells, human faecal flora, mucosal integrity and invading pathogens [17,18]. VOCs emitted from bodily fluids thus have huge potential as putative biomarkers for use in the assessment of gastrointestinal diseases. Alterations in the pattern of VOCs are thought to reflect changes in the gastrointestinal environment. This suggests a possible role for gut microflora dysbiosis in the pathophysiology of CRC [29].

Conclusions

This study has shown that the VOC signature present in the urine of patients with CRC, can be distinguished from healthy controls using FAIMS. The sensitivity and specificity of FAIMS is 88% and 60% respectively for CRC. Whilst this is lower than the gold standard of colonoscopy it is comparable with current faecal stool testing including the guaiac and immunohistochemical methods. The UK uptake for screening is low; 62%, 57% and 59% uptake in the first, second and third rounds of the national screening programme [30], and around 50% currently in the local population. One of the reasons for this is the nature of the biological sample required. Offering an alternative and less intrusive option, such as urine rather than faeces, is likely to be far more acceptable to patients, and can be incorporated into screening pathways for the future.

Acknowledgments

We would like to thank WPH, BRET and the Eveson Trust who provided funding for this research.

Author Contributions

Conceived and designed the experiments: RA CN KB JC. Performed the experiments: EW MT JC. Analyzed the data: RA MM EW MT JC. Contributed reagents/materials/analysis tools: RA EW MT JA. Wrote the paper: RA MM SC MT CH CN KB JC. Recruitment of patients: CRF PH NOC CB.

References

1. Siegel R, Naishadham D, Jemal A (2012) Cancer statistics. CA Cancer J Clin 62(1): 10–29.
2. Ferlay J, Parkin DM, Steliarova-Foucher E (2010) Estimates of cancer incidence and mortality in Europe in 2008. Eur J Cancer 46: 765–81
3. Brenner H, Tao S (2013) Superior diagnostic performance of faecal immunochemical tests for haemoglobin in a head-to-head comparison with guaiac based faecal occult blood test among 2235 participants of screening colonoscopy. Eur J Cancer 49 (14): 3049–54
4. Imperiale TF (2012) Non-invasive screening tests for colorectal cancer. Dig Dis 30 Suppl 2: 16–26.
5. De Meij TG, Ben Larbi I, van der Schee MP, Lentferink YE, Paff T, et al. (2014) Electronic nose can discriminate colorectal carcinoma and advanced adenomas by fecal volatile biomarker analysis: proof of principle study. Int J Cancer 134(5): 1132–1138.
6. Lippi G, Cervellin G (2012) Canine olfactory detection of cancer versus laboratory testing: myth or opportunity? Clin Chem Lab Med 50(3): 435–9
7. Sonoda H, Kohnoe S, Yamazato T, Satoh Y, Morizono G, et al. (2011) Colorectal cancer screening with odour material by canine scent detection. Gut 60(6): 814–9
8. Arasaradnam RP, Nwokolo CU, Bardhan KD, Covington JA (2011) Electronic nose versus canine nose: clash of the titans. Gut 60(12):1768
9. Westhoff M, Litterst P, Maddula S, Bödeker B, Rahmann S, et al. (2010) Differentiation of chronic obstructive pulmonary disease (COPD) including lung cancer from healthy control group by breath analysis using ion mobility spectrometry. International Journal for Ion Mobility Spectrometry 13(3–4): 131–139.
10. Phillips M, Cataneo RN, Ditkoff BA, Fisher P, Greenberg J, et al. (2003) Volatiles markers of breast cancer in the breath. The Breast J 9: 184–191.
11. Khalid T, White P, De Lacy Costello B, Persad R, Ewen R, et al. (2013) A Pilot Study Combining a GC-Sensor Device with a Statistical Model for the Identification of Bladder Cancer from Urine Headspace. PLoS ONE 8(7): e69602.
12. Bernabei M, Pennazza G, Santonico M, Corsi C, Roscion C, et al. (2008) A preliminary study on the possibility to diagnose urinary tract cancers by an electronic nose. Sens Actuat B Chem 131, 1–4.
13. Arasaradnam RP, Covington JA, Harmston C, Nwokolo CU (2014) Next generation diagnostic modalities in gastroenterology – gas phase volatile compound biomarker detection. Alimentary Pharmacology and Therapeutics 39 (8): 780–789.
14. Peng G, Hakim M, Broza YY, Billan S, Abdah-Bortnyak R, et al. (2010) Detection of lung, breast, colorectal, and prostate cancers from exhaled breath using a single array of nanosensors. Br J Cancer 103(4):542–51
15. Altomare DF, Di Lena M, Porcelli F, Trizio L, Travaglio E, et al. (2013) Exhaled volatile organic compounds identify patients with colorectal cancer. Br J Surg 100(1): 144–50.
16. Silva CL, Passos M, Câmara JS (2011) Investigation of urinary volatile organic metabolites as potential cancer biomarkers by solid-phase microextraction in combination with gas chromatography-mass spectrometry. Br J Cancer 105(12): 1894–904.
17. Probert CS, Ahmed I, Khalid T, Johnson E, Smith S, et al. (2009) Volatile organic compunds as diagnostic biomarkers in gastronintestinal and liver disease. J Gastroninestin Liver Dis 18: 337–43
18. Arasaradnam RP, Pharaoh MW, Williams GJ, Nwokolo CU, Bardhan KD, et al. (2009) Colonic fermentation–more than meets the nose. Med Hypotheses 73(5): 753–6
19. Buszewski B, Kesy M, Ligor T, Amann A (2007) Human exhaled air analytics: biomarkers of disease. Biomed Chromatogr 21: 533–66
20. Garner CE, Smith S, de Lacy Costello B, White P, et a.l (2007) Volatile organic compounds from feces and their potential for diagnosis of gastrointestinal disease. FASEB J 21: 1675–88
21. Arasaradnam RP, Quraishi N, Kyrou I, Nwokolo CU, Joseph M, et al. (2011) Insights into 'Fermentonomics': Evaluation of volatile organic compounds (VOCs) in human disease using an Electronic 'e' Nose. J Med Eng Technol 35(2):87–91.
22. Arasaradnam RP, Ouaret N, Thomas MG, Gold P, Quraishi MN, et al. (2012) Evaluation of gut bacterial populations using an electronic e-nose and field asymmetric ion mobility spectrometry: further insights into 'fermentonomics'. J Med Eng Technol 36(7):333–7.
23. Covington JA, Westenbrink EW, Ouaret N, Harbord R, Bailey C, et al. (2013) Application of a novel tool for diagnosing bile acid diarrhoea. Sensors (Basel) 13(9): 11899–912
24. Arasaradnam RP, Bardhan KD (2010) Bioactive foods and Extracts – Cancer treatment and prevention. Taylor Francis, New York.
25. Covington JA, Wedlake L, Andreyev J, Ouaret N, Thomas MG, et al. (2012) The detection of patients at risk of gastrointestinal toxicity during pelvic radiotherapy by electronic nose and FAIMS: a pilot study. Sensors (Basel) 12(10): 13002–18
26. Arasaradnam RP, Ouaret N, Thomas MG, Quraishi N, Heatherington E, et al. (2013) A novel tool for noninvasive diagnosis and tracking of patients with inflammatory bowel disease. Inflamm Bowel Dis 19(5): 999–1003.
27. Arasaradnam R, Westinbrink E, McFarlane M, Harbord R, Chambers S, et al (2014) Differentiating Coeliac disease from irritable bowel syndrome by urinary volatile organic compound analysis – a pilot study. PLOS One (in press)
28. Lidgard GP, Domanico MJ, Bruinsma JJ, Light J, Gagrat ZD, et al. (2013) Clinical performance of an automated stool DNA assay for detection of colorectal neoplasia. Clin Gastroenterol Hepatol 11(10): 1313–8
29. Pagnini C, Corleto VD, Mangoni ML, Pilozzi E, Torre MS, et al. (2011) Alteration of local microflora and α-defensins hyper-production in colonic adenoma mucosa. J Clin Gastroenterol 45(7): 602–10.
30. Moss SM, Campbell C, Melia J, Coleman D, Smith S, et al. (2012) Performance measures in three rounds of the English bowel cancer screening pilot. Gut 61(1): 101–7.